Atomic-Scale Interface Magnetism for Spintronics

Jean-Baptiste Laloë

Atomic-Scale Interface Magnetism for Spintronics

Jean-Baptiste Laloë
Darwin College

A dissertation submitted for the degree of
Doctor of Philosophy
at the University of Cambridge

March, 2007

Abstract

Atomic-Scale Interface Magnetism for Spintronics

by Jean-Baptiste Laloë

RECOGNISING that the characterisation of actual interfaces in magnetic multilayer systems will provide valuable insight for the integration of spintronics in practical devices, a study of interface effects in various structures is presented. Magnetometry measurements are performed for a range of Fe thicknesses (0.4 - 23 nm) grown by molecular beam epitaxy on GaAs and InAs substrates in order to determine the factors governing the evolution of the magnetic moment of epitaxial Fe grown on a zinc-blende semiconductor. A greater reduction of the Fe magnetic moment is observed for films grown on InAs as compared to GaAs, as the Fe films reach a bulk-like moment (within 10% deviation) at a thickness of ∼5.2 nm and ∼2.2 nm, respectively. From this direct comparative study it is concluded that interface and interdiffusion effects are the dominant mechanisms influencing the value of the magnetic moment for ultra-thin Fe films on GaAs and InAs. Spin injection at this interface is performed, by detecting optical polarisation in the oblique Hanle geometry from a Fe/AlGaAs/GaAs spin-light emitting diode structure. The electrical and magnetic properties of the system are presented, and a ∼1% injection polarisation at room temperature, rising to ∼4% at 77 K is reported. A study of the deposition and growth of MgO thin (3 - 39 nm) films in conjunction with magnetic layers is also performed. Crystallinity of MgO grown on GaAs is obtained, and epitaxial growth of Fe and Co on MgO is demonstrated. Polarised neutron reflectivity results again indicate a slight decrease in Fe and Co magnetic moments due to interfacial oxide layers. MgO is also incorporated in a pseudo-spin-valve structure which demonstrates epitaxy-induced magneto-crystalline anisotropy. It is concluded that the interface quality is a critical parameter for spintronic devices. Atomic-scale defects and intermixing in real samples mean that current theoretical estimates of ∼100% injection efficiency in perfect systems remain unattainable. However by increasing atomic-level structural control of interfaces, a substantial increase in efficiency might be achieved, similarly to the recent breakthrough in tunnelling magneto-resistance ratios which have reached 1000%.

à Alex

Declaration

This dissertation is the result of my own work and, unless otherwise stated, contains nothing which is the outcome of work done in collaboration. I have written this thesis in the first person plural form as a personal preference for ease of reading. No part of this thesis has already, or is currently being submitted for any other qualification than the degree of Doctor of Philosophy at the University of Cambridge. This thesis contains approximately 37,000 words.

Jean-Baptiste Laloë
March, 2007

Acknowledgements

I am very grateful to my supervisor Prof. J. A. C. Bland for continuous scientific and financial support. I also thank the Cambridge Philosophical Society, Darwin College and the Cavendish Laboratory for financial backing.

I am also very grateful to Dr. S. N. Holmes for thorough additional help and guidance throughout my work. I also thank all past and present TFMM members who have surrounded and helped me throughout this work, in particular Dr. A. Ionescu who taught me the joys and discipline of UHV physics. Thanks also to R. Mansell for our collaboration on the electro-luminescence experiment. The Cavendish staff has been very helpful during my research, and thanks are due to the workshop team, in particular Rik Balsod, Dave Johnson, Dave Powell and Terry Stubbings for always impeccable jobs. Outside of the department, I am grateful to Dr. M. E. Vickers of the Department of Materials Science and Metallurgy for her assistance and patience with me for the X-ray measurements, and Dr. R. M. Dalgliesh and Dr. S. Langridge of the Rutherford Appleton Laboratory for assistance during the PNR data collection.

I also thank Stuart Holmes, Adrian Ionescu and David Gillingham for careful proofreading and comments on this thesis.

On a more personal note, there are many people who have supported me during this work and my time in Cambridge. I thank my parents and siblings for being parents and siblings. I am grateful to my office mates, Tom in particular, for laughs each day. Thanks to Kate for being my college friend, and Jenny for livening up Cavendish tea times. Sports has been a major part of my life here, and I thank everybody who has motivated, coached, and trained with me for tournaments and races. This includes Anna, Beth and Ted, Christian, Hannah,

Stuart, my parents and siblings, and so many more, also from Strange Blue. Thanks for the support and motivation.

Of course there have been struggles during these past few years, but I was always well surrounded, and certain people have become very special to me. In particular I am so grateful to Hannah for being here; I could not have done this without you. I thank Kelly for so many supportive coffee times, and being there for me to lean on. Milou - you have brightened so many mornings and evenings. And Anna, thanks for teaching me so much.

Finally, I shall close with a couple of words *en français*.

Contents

List of Figures

List of Tables

Chapter 1

Introduction

1.1 Magneto-Static Phenomena

1.1.1 Magnetic Moments

Magnetism is one of the oldest phenomena in the history of natural science. The fundamental object in magnetism is the magnetic moment which in a classical picture can be equated to a current loop. If there is a current I around a vanishingly small oriented loop of area $\mathbf{dS}$, then the magnetic moment $\mathbf{d}\mu$ is given by [1]:

$$\mathbf{d}\mu = I\mathbf{dS}, \tag{1.1}$$

and the magnetic moment has units of A.m^2. For a loop of finite size, we calculate the magnetic moment by summing up the moments from the contained infinitesimal loops, by integrating equation 1.1:

$$\mu = \int d\mu = I \int \mathbf{dS}. \tag{1.2}$$

In atoms, the magnetic moment μ associated with an orbiting electron lies along the same direction as the angular momentum $\mathbf{L}$ of that electron and is proportional to it as $\boldsymbol{\mu} = \gamma\mathbf{L}$, where γ is a constant known as the gyromagnetic ratio. A magnetic moment in an external field will have energy $E = -\boldsymbol{\mu}\cdot\mathbf{B}$, so in order to minimise this energy there will be a torque on the magnetic moment. As the magnetic moment is associated with the angular momentum, and because torque is equal to the rate of change of angular momentum, we can write

$$\frac{d\boldsymbol{\mu}}{dt} = \gamma\boldsymbol{\mu} \times \mathbf{B}, \tag{1.3}$$

indicating that the change in μ is perpendicular to both $\boldsymbol{\mu}$ and $\mathbf{B}$, thus the magnetic field causes the direction of $\boldsymbol{\mu}$ to precess around $\mathbf{B}$.

Magnetic materials are materials which are magnetised to some extent by a magnetic field. When a magnetic material is magnetised uniformly the intensity of the magnetisation is given by the sum of all the magnetic moments in the material. Thus the concept of magnetisation is an ensemble of elementary magnetic moments.

1.1.2 Magnetic Disorder and Order

Various materials exhibit different magnetic behaviours and states of order. Physical formalism for each of these can be found in references [1] and [2], and will not be repeated here, but we will present an overview and description of these magnetic states.

Diamagnetism and Paramagnetism

Diamagnetism means a feeble magnetism which occurs in a material containing no atomic magnetic moments, and has a small negative magnetic susceptibility[1]. The mechanism by which the magnetisation is induced opposite to the magnetic field is the acceleration of the orbital electrons by electromagnetic induction caused by the penetration of the external field into the orbit. According to Lenz's law, the magnetic flux produced by this acceleration of an orbital electron is always opposite to the change in the external magnetic field [2].

Paramagnetism is a feeble magnetism which exhibits a positive susceptibility. Paramagnetic behaviour is found in materials that contain magnetic atoms or ions that are widely separated so that they exhibit no appreciable interaction with each other. Without an applied magnetic field, these magnetic moments point in random directions because the magnetic moments in neighbouring atoms interact only very weakly, to the point where they can be assumed to be independent. However, applying an external field aligns the moments to a degree

[1]The magnetic susceptibility, χ, is the degree of magnetisation of a material in response to an applied magnetic field: $\mathbf{M} = \chi\mathbf{H}$ where $\mathbf{M}$ is the magnetisation and $\mathbf{H}$ the applied field.

Material	T_C (K)
Fe	1043
Co	1394
Ni	631
Gd	289
MnSb	587
EuO	70
EuS	16.5

Table 1.1: (from [1]) Curie temperature, T_C, of some common ferromagnets.

determined by the strength of the applied field. Although an increase in the magnetic field will tend to line up the spins (moments), an increase in temperature will randomise them. The paramagnetic effect is generally much stronger than the diamagnetic effect, although the diamagnetism is always present as a weak negative contribution.

Ferromagnetism

A ferromagnet has a spontaneous magnetisation, even in the absence of an applied field. All the magnetic moments lie along a single unique direction[2]. The mechanism for the appearance of ferromagnetism was first clarified in 1907 by Pierre Weiss. He assumed that in a ferromagnetic material there exists an effective molecular field, $\mathbf{B}_{mf}$, considered to align the neighbouring spins parallel to one another because the dominant exchange interactions are positive. In the Weiss model, the ferromagnet is treated as a paramagnet placed in a magnetic field $\mathbf{B} + \mathbf{B}_{mf}$. At low temperatures, the moments can be aligned by the internal molecular field, even without any applied external field, and the magnetic order is self-sustaining. As the temperature is raised, thermal fluctuations begin to destroy the magnetisation and at a critical temperature the order will be destroyed. The temperature at which this transition occurs is the Curie Temperature, T_C.

The idea of the molecular field is only a convenient image to explain the ordering in a ferromagnet. Such a magneto-static effect would require fields of $\sim 10^3$ T within the material. In fact, thirty year after Weiss, Heisenberg showed

[2]More precisely in no external field there is a uniform magnetisation direction in separate domains in the material.

that it was the exchange interaction, which is a purely electro-static effect and involves large Coulomb energies, which is responsible for the 'large' molecular field.

Antiferromagnetism

In antiferromagnetism, neighbouring spins are aligned antiparallel to each other so that their magnetic moments cancel. In this case the exchange interaction is negative, so it is favourable for nearest-neighbour magnetic moments to lie antiparallel to one another. Therefore an antiferromagnet produces no spontaneous magnetisation and shows only a feeble magnetism.

In this case, when an external field is applied in the direction along the spin axis, the spins experience no torque as they are already saturated in that direction, and the susceptibility is ~ 0 (at 0 K). In the case of non-zero temperature but remaining in the antiferromagnetic regime[3], the thermal fluctuations decrease the molecular field at both anti-parallel sublattices, and the applied field will enhance the magnetisation in one direction, and reduce it in the other. If instead an external field is applied perpendicular to the spontaneous magnetisation direction, the moments in both directions will tilt slightly so that a component of magnetisation is produced along the applied field direction, and this effect is nearly independent of temperature.

1.2 Magneto-Electronics: Spintronics

In addition to their mass and electric charge, electrons have an intrinsic quantity of angular momentum called spin. Devices which rely on an electron's spin to perform their functions form the foundation of spin-electronics, or spintronics. Information processing technology classically relies on charge-based devices, which have produced today's million-transistor microchips, but as the industry requires further miniaturisation conventional devices are reaching their limits both from a fundamental and technical point of view. Adding the spin degree of freedom to conventional electronic devices or using the spin alone has the potential advantages of non-volatility, increased data processing speed, decreased

[3]The transition temperature at which antiferromagnetism disappears is know as the Néel temperature, T_N.

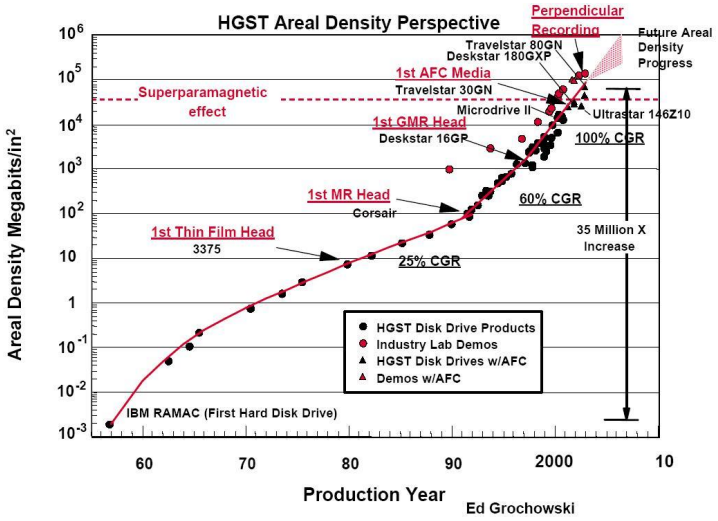

Figure 1.1: Increase of hard drive areal storage density, showing the 35 million × increase in storage density since 1957, and the increase in the compound annual growth rate (CGR) with the development of MR heads. Source: Hitachi GST.

electrical power consumption, and increased integration densities [3, 4].

Magnetism has always been important for information storage, with the earliest hard drives using inductive heads, and the second generation using magneto-resistance (MR) effects[4] to read and write data stored in magnetic domains. With the requirement for ever-increasing storage capacity, and read/write access speeds, the storage industry rapidly integrated MR read heads in hard drives, with anisotropic magneto-resistance (AMR) heads in the early 1990's, and giant magneto-resistance (GMR) heads by 2000. Nowadays, tunnelling magneto-resistance (TMR) heads are being used in commercially available high-capacity hard drives. Figure 1.1 shows the increase in areal storage density with the integration of MR heads in hard drives.

Alongside hard drive technology, recent years have seen the integration of magnetic storage elements in random access memory (RAM) with the development of magnetic random access memory (MRAM). An MRAM cell is made of two ferromagnetic contacts separated by a thin insulating layer. One of the ferromagnets is pinned to a given direction, and the other is free to rotate in an external field. The MR effect measured when switching between parallel and anti-parallel alignments of the two layers allows for the coding of bits in each cell.

[4]MR: A change in resistance caused by a magnetic field.

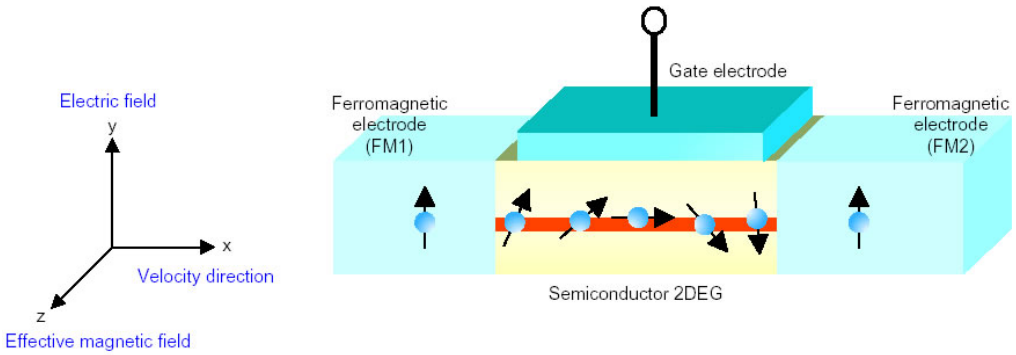

Figure 1.2: (from [6]) Schematic of a spin-FET. Injected electrons rotate because of the magnetic field created by the spin-orbit interaction induced by the applied gate voltage electric field.

An MRAM chip is a grid of such cells which can each be selectively read and written. One great advantage of MRAM over conventional RAM is its non-volatility, meaning that information can be retained in the absence power input.

Major challenges in the field of spintronics that are currently being addressed by experiment and theory include the optimisation of electron spin lifetimes, the detection of spin coherence, the transport of spin-polarised carriers, and the manipulation of both electron and nuclear spins in solid state materials. An understanding of the fundamental aspects of the control of the spin degree of freedom in semiconductors and heterostructures will lead to novel high-performance spin-based electronics with great potential. A common example of such a device is the spin-field effect transistor (FET), as proposed by Datta and Das in 1990 [5]. This has ferromagnetic source and drain contacts, separated by a narrow semiconducting channel. The source injects spin-polarised electrons into the channel and this spin current flows easily is it reaches the drain unaltered. A voltage applied to the gate electrode however, produces an electric field which causes the spins of the fast-moving electrons to precess, or rotate. The polarised drain therefore impedes the spin current depending on how far the spins have been rotated. Flipping the spins (thus controlling the current flow) requires much less energy and is much faster than the operation of conventional FETs. A schematic of a spin-FET is shown in figure 1.2.

A number of challenges lie ahead before the implementation of a spin-FET in a real device. However the progress toward understanding and implementing

the spin degree of freedom in metallic multilayers and semiconductors is gaining momentum as more research seeks to address individual obstacles associated with these novel ideas. A considerable impact on the storage industry and further potential applications in biology and chemistry promises that the emerging field of spintronics will provide fundamental new advances in both pure and applied science and technology for years to come.

1.3 Motivation: Interface Magnetism

The quality of the interface in spintronic devices is a critical parameter in thin film magnetic multilayers. Throughout this work, we study the effects of disorder, defects and intermixing at interfaces. These are found to have drastic consequences on magnetic and structural properties in multilayers.

Spintronics requires spin transport at room temperature (RT) across an interface or barrier. It is clear that the structural and magnetic order on the atomic scale at the interface are central to the efficiency of spintronic devices. Better control and understanding of such interfaces will allow for the improvement of MR ratios and spin injection and detection efficiency. With the adoption of TMR and more specifically the use of highly ordered MgO barriers, it has become clear that atomic order at interfaces is central to increased MR ratios. Indeed the progress from amorphous AlO_x to ordered or epitaxial MgO barriers has seen increase of the TMR ratio by over an order of magnitude. Simulations in perfect systems with abrupt interfaces have predicted the TMR ratios to increase further, as compared to current experimental results. Theoretical studies of spin injection from a ferromagnet into a semiconductor across ideal interfaces also predict extremely high injection polarisations surpassing all current experimental results. This is due to imperfection at the interfaces. In a real sample, roughness, intermixing, and lattice mismatch effects will be hugely detrimental to coherent spin injection.

The aim of this work is therefore to characterise real interfaces in magnetic multilayer systems, which will provide us with valuable insight for the integration of spintronics in practical devices.

1.4 Overview of the Thesis

This thesis presents a study of the challenges associated with thin film and interfacial magnetism. Each chapter can be taken as a stand-alone addressing a specific aspect of these obstacles, though they all complete each other and contribute to the general understanding of the issue.

Chapter 1: Introduction We present a brief background of the fields of magnetism and spintronics, and an overview of the thesis.

Chapter 2: GaAs Surfaces and Spin-Valve Structures In this review chapter, we present the fundamental properties of GaAs crystals and surfaces, and the initial aspects of Fe growth on GaAs. We also review growth and studies of epitaxial spin-valve structures.

Chapter 3: Experimental Techniques Here we briefly describe some main experimental methods we have used throughout the course of this project.

Chapter 4: Fe Magnetic Moment on GaAs, InAs In this chapter we present a study of the evolution of the Fe magnetic moment on GaAs and InAs, and describe the factors affecting it at ultra-low coverages.

Chapter 5: Electro-Luminescence The electro-luminescence experiment is a means of studying and detecting spin injection into a semiconductor. Here an overview of the theory and method is presented, as well as experimental characterisation results.

Chapter 6: MgO Growth and Applications Here we present details of the growth of MgO, and its integration in heterostructures for various device applications.

Chapter 7: Summary and Outlook In this concluding chapter we summarise the results from each aspect of our work and look ahead to ideas for future experiments which these results lead us to.

Sample Notations and Temperature Units

Throughout this thesis the order of growth of multilayers is written from the top surface to the substrate. Namely Au/Fe/GaAs(100) is a GaAs(100) substrate on

which we would have grown an Fe layer, and then a Au layer (cap). Throughout the thesis we have cited temperatures in °C and K. We have used K for low temperatures ($\leq$ room temperature) and °C for higher temperatures. The proportions of chemical solutions such as etchants are given by volume. For example HCl:H_2O (1:4) indicates 4 volumes of water per volume of HCl.

Chapter 2

GaAs Surface Reconstructions for Fe Growth and Epitaxial Spin-Valve Structures

Introduction and Outline

Epitaxy in magnetic heterostructures and multilayers has long been of interest, both for fundamental research purposes and for device applications. Indeed, epitaxial films and structures can be used as powerful tools to explore fundamental aspects of thin and ultrathin magnetic layers such as growth modes, interfaces and magnetic anisotropies. In this review chapter, we will firstly present the preparation methods of GaAs surfaces for epitaxial growth, including an overview of the various surface reconstructions. Then we will briefly discuss the growth of epitaxial Fe on GaAs. As we will see, this system has recently generated huge interest for spintronic device applications, with the interface being key to successful operation. We will then shift our interest to multilayers, and specifically epitaxial spin-valve structures, their growth and magnetic properties.

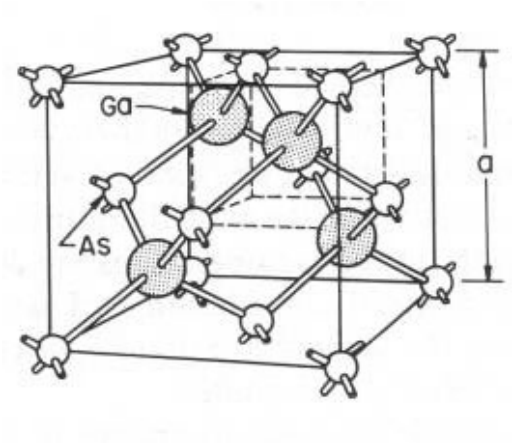

Figure 2.1: (from [9]) The GaAs unit cell, zincblende structure displaying the two (Ga and As) fcc sublattices, displaced by a quarter of the body diagonal.

2.1 Surface Reconstructions of GaAs(100)

2.1.1 Overview of GaAs

The rapidly growing use of GaAs in discrete devices, integrated circuits, opto-electronics, digital applications and alongside magnetic materials creates huge demand for single-crystal substrates of this material. Researchers have known the advantages of GaAs (as compared to Si) for decades, and the ability to produce semi-insulating substrates allows true monolithic circuit and device integration [7, 8].

Crystal Structure

A crystal is an object of high symmetry, ideally an infinite repetition of a three-dimensional building block. In the case of GaAs, this building block is a cubic Bravais lattice, more specifically two face centred cubic (fcc) lattices of Ga and As which are mutually penetrating, and shifted relative to each other by a quarter of the body diagonal, thus forming the zincblende structure. This lattice belongs to the tetrahedral phases. That is, each atom is surrounded by four equidistant nearest neighbours, which lie at the corners of a tetrahedron. The structure and tetrahedron are shown in figure 2.1. The lattice constant of undoped GaAs at RT is $a = 5.653$ Å, and its density is $\rho = 5.317$ g.cm^{-3}.

Crystal Planes

From the unit GaAs cell we can establish the basic crystal planes of GaAs. In the GaAs(100) surface, each As atom has two bonds with the Ga lattice below, the other two being free. The (110) plane contains the same number of Ga and As atoms, each atom having one bond with the layer below. Atoms on the (111) surface have three bonds with the Ga or As[1] atoms in the layers below, and the fourth is free [8]. However, we will see that this basic approach of the surface atoms and bonds is over-simplified, when we address surface reconstructions below.

Electronic Properties and Energy-Band Structure

Very briefly, GaAs is a direct band-gap semiconductor, with a band gap at room temperature of $E_G = 1.42$ eV. GaAs can be doped n- or p-type, with *e.g.* Si or Be atoms, respectively, and we note that impurities or crystal defects can introduce intra-band levels. A surface is naturally a location where the lattice is discontinuous, and where various oxides of Ga and As are present, as well as the possibility of elemental As [10]. In addition to this, numerous surface defects will cause 'surface states'. Unlike SiO_2 for the case of Si surfaces, there seems to be no dielectric material that passivates GaAs surfaces in a manner satisfactory to device fabrication [11].

2.1.2 *Ex situ* Surface Preparation and Cleaning

Production of semiconductor devices places a high premium on uniformity and yield. Therefore both cleaning and cleanliness are important matters to the semiconductor industry. This means removing contaminants from the wafer before processing or growth, and cleanliness refers to maintaining the level of cleanliness already present. Here we will briefly overview *ex situ* cleaning techniques.

Organic solvents are effective in removing oils, greases and organic materials such as photo-resist. These include acetone, ethanol and isopropanol. The debris removed by the solvent accumulates in the solvent, so the liquid must be rinsed or blown off.

[1] Of the eight planes in the {111} family for GaAs, four contain only Ga atoms, and the other four are comprised entirely of As atoms.

Wet etching is the use of liquid etchants to remove material. This has three main purposes, which are to polish, form patterns, and enable visualisation of defects or damages [12]. Wet etches will have characteristics such as anisotropic etching with respect to certain crystallographic orientations, and are usually based on oxidation of the Ga present. This means that the etchant solution will have an oxidising agent to oxidise the Ga, and a complexing agent and dilutant to form a compound with the oxide, and remove it. The most popular etchant system for GaAs consists of sulfuric acid, hydrogen peroxide, and water. We have used $H_2SO_4 : H_20_2 : H_2O$ (1:8:80) to etch GaAs, at a rate of ~ 80 Å/s [13]. Wet etching will depend on parameters such as agitation, temperature, time (if the layers of solution close to the etched surface become depleted of the molecules, in the absence of agitation) and, as we have mentioned before, on crystallographic orientation [8].

Dry etching has an advantage over wet-etching that it offers substantial directionality. The lateral etch rates in dry etching are close to zero, so undercutting of masking patterns can be greatly reduced. Dry etching techniques use a gas, generally in the form of a plasma, for etching. The techniques commonly used in GaAs processing include plasma etching, reactive ion etching, reactive ion beam etching, and ion milling. The first three processes are similar, using an accelerated plasma of a selected gas to efficiently volatilise the layer to be etched. Ion milling is a purely physical process in which energetic inert ions are delivered to the surface in a uniform directional beam.

2.1.3 *In situ* Substrate Cleaning and Surface Reconstructions

The ideal GaAs(100) surface is terminated (the topmost layer) by either Ga or As atoms. Experimentally, growth and cleaning conditions yield up to seven different reconstructions of the surface. Practically, these reconstructions are obtainable by varying the substrate temperature, or the Ga to As ratio during growth. *In situ* cleaning of a substrate in an ultra-high vacuum (UHV) chamber will include annealing steps, as well as ion sputtering, which will both have effects on the GaAs surface.

Ar^+ ion Sputtering of GaAs

Sputtering is an *in situ* cleaning step involving bombardment of a surface with high-energy ions. Inert Ar^+ ions are usually used in the case of GaAs. Pechman *et al.* studied the effect of Ar^+ sputtering of GaAs at a range of temperatures [14]. This study was performed on GaAs(110) rather than GaAs(100), but explores surface layer defects and disorder created by the sputtering, which would be similar on both surfaces[2]. Pechman *et al.* [14] find that the bombardment of GaAs with Ar^+ atoms at normal incidence creates layer defects that generally span one or two unit cells. The state of the semiconductor (SC) surface after sputtering at various beam energies and temperatures was studied using scanning tunnelling microscope (STM).

Images following room temperature sputtering with low-energy (300 eV) ions indicated that some material ejected from pits by ion impact remained on the surface as adatoms. However, the adatoms produced by sputtering at $600 \leq T \leq 775$ K were mobile, and thermal effects promoted local healing. In addition to this, with continued material removal from the topmost layer, additional vacancy sites can be produced in the newly exposed layer, leading to multilayer erosion, and roughening of the surface. Wang *et al.* [16] have shown that the sputtering yield for normal incidence bombardment of GaAs depends weakly on ion energy, but the vacancy size produced by individual ions averages 4-6 atoms at 3000 eV instead of 2-4 atoms at 300 eV. Multilayer erosion studies at 3000 eV revealed that sputtering leads to surface roughening below 775 K, but we also remember that As desorbs above 800 K, even without induced surface disorder [17].

Annealing and Surface Reconstructions of GaAs(100)

When the surface of a semiconductor is allowed to relax at high temperature, it can lower its total energy by forming dimers [18]. The (100) surface of GaAs is of intrinsic interest because it is known to manifest various surface reconstructions depending on the surface composition. Several recent STM studies have tried to catalogue the various surface reconstructions of GaAs(100), and establish their occurrence as a function of parameters such as substrate temperature and Ga to

[2]Gillingham [15] presents STM images of the (100) surface after sputtering and annealing treatments.

As flux ratio during growth [19–22]. Despite its conceptually simple operation principle, STM can resolve local electronic structures on an atomic scale with little damage or interference with the sample [23]. Coupled with low-energy electron diffraction (LEED) and/or reflection high-energy electron diffraction (RHEED), STM is thus an ideal tool to investigate the atomic structure of GaAs surface reconstructions.

The notations used to differentiate amongst surface reconstructions *e.g.* (1×1) or (2×4), represent the change in period of the surface symmetry, or surface density. For instance the (2×4) reconstruction of GaAs(100) is so labelled because the unit cell is 2 periods long in the $(0\bar{1}1)$ direction, and 4 periods long in the (011) direction.

Biegelsen *et al.* [19] present a survey of reconstructions obtained by cooling the substrate after GaAs growth to a range temperatures, and varying the As or Ga flux while doing so. They thus obtain and identify various surface reconstructions, and also suggest ball-and-stick models of surface atom placement for each reconstruction. They report to obtain a $c(4 \times 4)$ surface by cooling the grown GaAs epilayer to 300°C in either As_4 or As_2 flux, then moving the sample to UHV. They note in passing that the dimers observed in this $c(4 \times 4)$ reconstruction are aligned perpendicular to the As dimers observed in the well-documented $c(2 \times 8)$ surface, sometimes also named (2×4). This $c(2 \times 8)$ surface was prepared by cooling the as-grown samples to 500°C in the As flux, and then quenching in UHV. Attempts to obtain the (1×6) surface were made by annealing $c(2 \times 8)$ surfaces to 600°C for 5 minutes in vacuum. In fact, the STM images showed considerable ordering in the $2\times$ direction, and the unit cell appears to be (2×6). The surface cell is apparently two As dimers and four missing As dimers stacked along the $\times 6$ direction. Finally, the authors report on a Ga-rich $c(8 \times 2)$ surface, reported to have almost no surface-bonded As, obtained by annealing the samples at 690°C in UHV. We note that the subunit for this surface reconstruction is a (4×2) which consists of two Ga-Ga dimers adjacent to one another and two missing dimers.

Behrend *et al.* [20] investigate the transition from the As-rich to the Ga-rich phases in the reconstruction phase diagram. From an initial (2×4) As stabilised surface, Ga-rich surfaces are shown to appear through post-growth annealing. No significant change to the reconstruction is observed after a 5 minute anneal

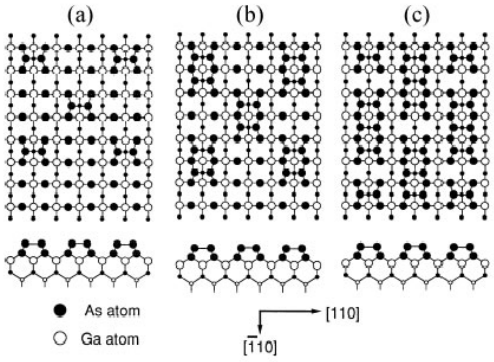

Figure 2.2: Ball-and-stick models for the GaAs(100)-$c(4 \times 4)$ surface reconstruction, as suggested by (a) Xue *et al.* [22]; (b) Larsen *et al.* [24]; and (c) Sauvage-Simkin *et al.* [25].

at 610°C in UHV, but when increasing the time and temperature of the heat treatment to 15 minutes with a ramp from 610°C to 640°C , a clear (4×6) pattern appears, as observed by RHEED. Interestingly, the STM images reveal a domain structure with (2×6) As-terminated and (4×2) Ga-terminated areas co-existing. This is why such a reconstruction is sometimes referred to as a pseudo- or $P(4 \times 6)$, as it is not an intrinsic reconstruction.

More recently, Xue *et al.* [22] have confirmed the existence of this $P(4 \times 6)$ reconstruction, but they have also explored the formation of a 'genuine', (4×6) surface reconstruction, the $G(4 \times 6)$. The 'genuine' (4×6) phase is uniquely characterised by an array of large oval protrusions located at each corner of the unit cell, as observed by STM. These are Ga clusters, which sit in between the Ga dimers. It is not specified how this reconstruction was obtained, though it is understood to be very difficult to stabilise, with a single missing-atom defect causing a transition back to the (4×2) sub-unit.

Xue *et al.* [22] also explore the As-rich reconstructions previously mentioned. In particular, the authors present an overview of the three known phases of the (2×4) reconstructions, denoted α, β, and γ, each with specific As coverage. They also suggest further ball-and-stick models for the $c(4 \times 4)$ reconstruction, and compare theirs to previous suggestions, as shown in figure 2.2.

Finally, from a theoretical viewpoint, pseudo-potential calculations have been made for a number of these surface reconstructions. For example, Srivastava *et al.* present *ab initio* pseudo-potential calculations for equilibrium atomic geometry

and chemical bonding on the As-terminated $\beta 2(2\times4)$ surface [21]. One particular finding in this case is that there are two distinct Ga-As bond lengths between the first and the second layers, due to the presence of both threefold and fourfold coordinated Ga atoms in the second layer.

2.2 Epitaxy and Magnetism of Fe/GaAs

Successful epitaxial growth of Fe on GaAs(100) was first reported by Waldrop and Grant, in 1979 [26]. They report room-temperature growth on an Ar^+-ion sputtered and then annealed substrate. Since then there have been numerous reports and studies of this system, also for growth for low (<100°C) and high (>300°C) temperatures. It is widely accepted that the epitaxial growth is attributed to the fact that the lattice constant of α-Fe (2.866 Å) is almost half of that of GaAs (5.653 Å)[3], yielding a misfit of 1.4% in cube-on-cube epitaxy, provided the doubling of the Fe lattice periodicity compared to that of the GaAs.

Wastlbauer and Bland [27] have produced a detailed review of the properties of ultrathin epitaxial Fe films on GaAs(100). We will therefore not repeat their work, but discuss the effect of the reconstruction on the growth, evolution of the anisotropies, and then the spin dynamics at the Fe/GaAs interface.

2.2.1 Influence of the Surface Reconstruction on Fe Growth

Due to the differences in number and arrangement of surface atoms, it is not surprising that surface reconstructions have a significant effect on the initial growth morphology of Fe on GaAs(100).

The first STM study of sub-monolayer Fe grown on GaAs was presented by Takeshita *et al.* [28]. At RT, they found that on As-rich $c(4\times4)$, Fe forms small round clusters whose diameter of roughly 15 Å does not change appreciably when the coverage increases from 0.4 to 0.8 ML. They suggest that these clusters nucleate at specific positions within the basis of the reconstruction. They also demonstrated that the size of the Fe clusters is strongly dependent on the GaAs reconstruction by growing on Te-stabilised (2×1) surfaces, where the size and distribution of the clusters was not uniform.

[3] In bulk Fe, the body-centred cubic (bcc) α phase is the only stable phase between RT and 910°C, and it also offers the smallest lattice mismatch to GaAs.

Keedler *et al.* [29] studied the magnetic and structural properties of epitaxial Fe films grown at 175°C on both the (2×4) and $c(4 \times 4)$ reconstructions. As a note, we now know that interdiffusion at the interface will be increased at such a growth temperature. Both of these reconstructions consist of aligned As dimers, but they are parallel to $[0\bar{1}1]$ and [011] on (2×4) and $c(4 \times 4)$, respectively. However the $c(4 \times 4)$ does not display a long-range row-like structure, but is spatially isotropic [27]. On (2×4), Fe is found to adsorb predominately on the As dimers on the surface for sub-monolayer coverages, forming local Fe_3As_2 and Fe_2As clusters. Compared to this, Fe atoms on the $c(4 \times 4)$ surface are found to accumulate in fewer, but larger, two-dimensional islands. Similarly to Takeshita *et al.* [28] at RT, no structural anisotropy was detected in the growing of the Fe film. As these two studies were performed at different temperatures, we can conclude that the shape of the Fe islands on the $c(4 \times 4)$ surface is not very sensitive to temperature.

Moosbühler *et al.* [30] and Ionescu *et al.* [31] study the growth of Fe on Ga-rich surfaces, namely the (4×2) and (2×6) reconstructions. These also present a pronounced row-like structure, though less pronounced than the above As-rich surfaces. Nonetheless, the STM data shows that the resulting three-dimensional (3D) islands are predominately arranged parallel to the direction given by the substrate reconstruction. Ionescu *et al.* [31] report that from a nominal coverage of 0.1 ML, the Fe starts to cluster solely atop the As rows[4]. After deposition of 0.3 ML Fe, the Fe clusters are still predominately on the top of the As rows, but a few have moved to the underlying top Ga dimer layer. The authors note that the reconstruction of the GaAs at this stage appears to still be intact, surrounding the Fe clusters. The main parameters of the Fe islands on GaAs(100)-(2×6) are shown in figure 2.3. We note in particular that at $\sim$0.4 ML the slope of the height becomes nearly constant, and that the island density remains almost constant from 0.3 to 0.6 ML. From then on, the coalescence of islands reduces their density by increasing the island size. This work further proposes a model for the initial nucleation at 0.3 ML, and suggests the formation of Fe_2As seed crystals for bcc Fe growth.

[4]We note that the (2×6) reconstruction is Ga-rich, but As-terminated.

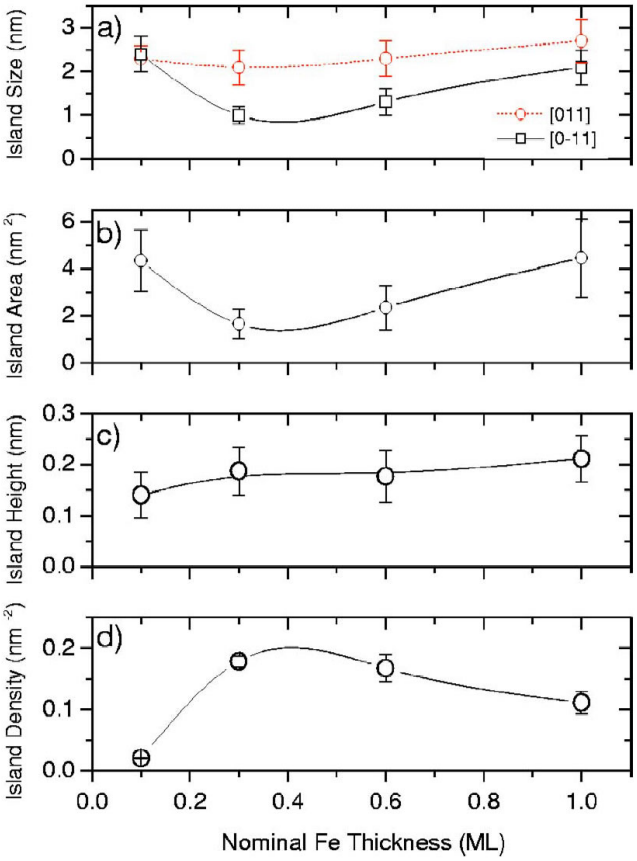

Figure 2.3: (from [31]) The island (a) size; (b) area; (c) height; and (d) density as a function of nominal coverage, for the growth of Fe on GaAs(100)-(2 × 6). The lines are guides to the eye.

2.2.2 Theoretical Studies of Fe/GaAs

Fe growth on GaAs has also attracted some theoretical interest. Indeed, several groups have attempted to model the system and interface from a chemical, electronic, and magnetic point of view.

Hong *et al.* [32] investigated the electronic and magnetic structure of Fe atoms grown on a GaAs(100) surface using the full potential linearised augmented plane wave method. The aim of this simulation is to enlighten the reason for the significantly reduced magnetic moment of Fe grown on GaAs(100). They calculate the physical properties at the interface by calculating the total energies of the systems for half and full monolayer coverage. In this study, any surface relaxation and reconstruction were not allowed and the Fe atoms were assumed to sit on the As (Ga) sites for the half monolayer on the Ga- (As-) terminated surface. For the full monolayer the other type of atom was added. Hong *et al.* [32] conclude that the outward diffusion of As atoms toward the surface is responsible for the local antiferromagnetism at the Fe/GaAs interface, and the probable reason for the reduction of the magnetic moment.

Erwin *et al.* [33] use density-functional theory to describe the initial stages of Fe film growth on GaAs(100), focusing on the interplay between chemistry and magnetism at the surface. The authors take two complimentary approaches, by studying the behaviour of single Fe adatoms deposited on GaAs and also the interface structure of complete Fe films at coverages up to several monolayers. Their study suggests four generic features that may play an important role. Namely:

- At sub-monolayer coverages, a strong chemical interaction between Fe and substrate atoms leads to substantial adsorption and intermixing. This interaction is strong enough to break surface Ga-Ga and Ga-As bonds to form Fe-As bonds;

- Between 1 and 2 ML coverage a crossover occurs from a preference for an intermixed film to an abrupt interface. This arises from the competition between maximising the coordination of the Fe atoms and minimising the amount of excess interfacial Fe. For Fe films of 2 ML and more the latter effect dominates and sharper interfaces become energetically preferred;

- Ga and As adlayers dramatically reduce the formation energies of Fe films. This is a stabilising effect that occurs for both Ga- and As- terminated interfaces, and both intermixed and abrupt interfaces;

- And these three generic features imply a fourth, which is the diffusion of Ga or As atoms liberated from the interface to migrate to the surface of the Fe film.

We note that Erwin *et al.* [33] state that these four conclusions apply to all GaAs reconstructions they considered.

2.2.3 Magnetic Anisotropies of Epitaxial Fe/GaAs

Magnetic anisotropy is determined by minimising the free energy per unit volume with respect to the magnetisation direction cosines. Different contributions to the total energy have to be added: magneto-crystalline anisotropy, demagnetising field energy (shape anisotropy), magneto-elastic coupling energy, etc. In thin films additional surface and interface, or strain dependent corrections are often included in order to take account of deviations from the bulk [34, 35]. Thin films of Fe grown on GaAs(100) display a remarkable and unexpected in-plane uniaxial magnetic anisotropy with a [011] easy axis. This is dramatically different from the cubic magnetic anisotropy of bulk Fe, which has $\langle 001 \rangle$ easy axes. The switch from the uniaxial to cubic anisotropy occurs between 50 and 60 ML coverage of Fe [36, 37]. There have been several studies of this uniaxial magnetic anisotropy, in attempts to determine its origins and the parameters affecting it.

Moosbühler *et al.* [30] approach the uniaxial anisotropy from a geometric point of view, and establish the link, if any, between the surface reconstruction and symmetry and the magnetic anisotropy. They grew epitaxial Fe films on the (4×2) and (2×6) Ga-rich reconstructions. These two reconstructions have terminating atomic rows running in perpendicular directions with respect to each other: [011] for (4×2), and $[0\bar{1}1]$ for the case of the (2×6) surface. Moosbühler *et al.* [30] grew Fe on a surface with both co-existing reconstructions present, and repeatedly imaged the same region by STM. As previously stated, they find that the deposited Fe atoms arrange following the surface reconstruction rows. The authors performed the magnetic characterisation using magneto-optical Kerr

effect (MOKE) measurements. They determine the anisotropy constants versus the Fe thickness for both reconstructions, and find that while the fourfold terms are identical for both reconstructions, the uniaxial constants are slightly different (10%), but only for the thinnest films (<10 ML). After assessing contributions from the Fe/GaAs and Au/Fe interfaces however, Moosbühler *et al.* [30] conclude that the magnetic anisotropy of Fe/GaAs(100) is not directly related to the specific surface reconstruction, though the exact atomic configuration at the interface needs to be further elucidated in order to understand the microscopic origin of the uniaxial anisotropy.

Thomas *et al.* [38] performed a grazing incidence X-ray diffraction study of epitaxial Fe ultrathin (1.5 - 13 nm) films on GaAs(100), revealing anisotropies of both domain shape and strain. With this range of thickness, the experiments cross the magnetic anisotropy transition, which was easily verified with MOKE measurements. The authors performed grazing incidence reciprocal space mapping to determine the in-plane coherent domain size and strain information. They find that for their thinnest (1.5 nm) sample, the Fe is perfectly pseudomorphic with the GaAs substrate, as the diffuse layer and sharp substrate peaks are super-imposed. For their thickest sample (13 nm) however, the maximum of the Fe peak has shifted away from the substrate peak, indicating that the Fe has relaxed at that thickness. They find that below 2 nm the Fe film is pseudomorphic, but above 2 nm anisotropic relaxation takes place, the film being more relaxed along [011] than along $[0\bar{1}1]$. The coherent domain study revealed that the in-plane size is anisotropic, being elongated along the $[0\bar{1}1]$ direction for thicknesses below 3 nm, and along the [011] direction above that thickness. Thomas *et al.* [38] concluded that considerable strain and shape anisotropies exist in Fe films, with the interfacial effect being the principle contributor to the observed uniaxial magnetic anisotropy for thin films, and the strain anisotropy the main factor responsible for the reversal of the anisotropy at high Fe thickness.

Finally, Zhai *et al.* [39] studied the evolution of the magnetic anisotropy in epitaxial Fe by ferromagnetic resonance (FMR), for both the in-plane and perpendicular cases, but only for film thicknesses from 4 to 33 ML. They first confirm the uniaxial anisotropies previously established. Also, they find that for $t \geq 5.2$ ML the FMR curves become asymmetrical, thus requiring an additional term with fourfold anisotropy to fit. When the film thickness reaches 18 ML

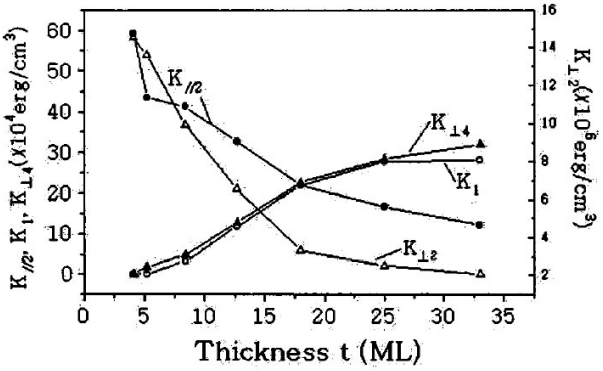

Figure 2.4: (from [39]) Various anisotropy constants for Fe/GaAs(100) as a function of film thickness. $K_{\|2}$ and K_1 are the uniaxial and cubic anisotropy constants, respectively. $K_{\perp 2,4}$ are the perpendicular anisotropy constants.

the in-plane magnetic anisotropy of fourfold symmetry is clearly seen, and it increases with thickness. As bulk Fe is of bcc structure, Zhai *et al.* [39] reasonably assume that the anisotropy of fourfold symmetry indicates the appearance of cubic anisotropy. For the case of perpendicular anisotropy, the authors find a very strong anisotropy constant for low thickness, which decreases with increasing film thickness. Various anisotropy constants are summarised in figure 2.4. Here we see that the in-plane uniaxial anisotropy constant ($K_{\|2}$) is as high as 59×10^4 erg/cm^3 for the film thickness of 4.1 ML, and decreases with increasing film thickness, reaching 12×10^4 erg/cm^3 for the 33 ML film. However the authors note the decrease in the slope of $K_{\|2}$ versus thickness, which indicates that the uniaxial anisotropy originates from the magneto-elastic interaction due to the strain at the interface. Thus, it decreases with increasing thickness due to lattice relaxation. The cubic magnetic anisotropy K_1 appears after 8.4 ML and its strength increases with film thickness, indicating the formation of a ferromagnetic continuous film. For their thickest sample (t = 33 ML), the cubic anisotropy constant reaches 28.2×10^4 erg/cm^3, which is about 60% of the value of bulk bcc Fe.

2.2.4 Spin Dynamics in Ultra-Thin Fe/GaAs

The system of Fe/GaAs(100) is an ideal model to study the magnetism of nanoparticles with controlled anisotropies close to or at the boundary between super-

paramagnetism and ferromagnetism. This transition for the Fe/GaAs system has been reported to occur at a thickness of ∼4 ML [36]. This transition is related to the three-dimensional growth mode of the Fe. At low coverages, we have seen that the Fe forms clusters on the substrate surface which grow in size with the deposition of more material. At a certain cluster size, short range ferromagnetic order is established within each of these clusters, though they still do not correlate. This is the superparamagnetic phase. At the critical thickness, the clusters coalesce and the system devolves into the ferromagnetic phase.

Steinmuller *et al.* [40, 41] have studied spin dynamics in ultrathin Fe/GaAs at the superparamagnetic/ferromagnetic (SP/FM) phase transition. They used a combination of *in situ* MOKE, STM and *in situ* Brillouin light scattering (BLS) measurements on samples in the range of 3.2-20 ML to probe the static and dynamic magnetic response of the system directly after deposition. STM imaging was performed to verify the growth mode, and coalescence of the Fe film in the FM regime, already observable for a thickness of 3.9 ML ($d_c \simeq 3.8$ ML). The BLS measurements show a significant decrease in spin wave frequency as well as a sharp increase in spin wave line-width with decreasing thickness in a very narrow thickness region (∼0.4 ML) close to d_c. This indicates the clear influence of spin fluctuations in the vicinity of the phase transition. In the SP regime spin wave modes are still observed but with a frequency close to that of the uniform cluster mode. However there are indications of a propagating mode, so they are attributed to spin waves propagating from cluster to cluster, mediated by dipolar interactions.

2.3 Epitaxial Spin-Valve Structures

Introduction and Outline

Heterostructures such as Fe/GaAs have numerous research applications for spintronic devices. Magnetic multilayers however are already being used in various device applications, and have great importance in storage technology. The knowledge and understanding of magnetic multilayers is a strong motivation in constant attempts to increase storage capacity, reliability and speed. In this section we will present an overview of epitaxial spin-valve (SV) structures. These

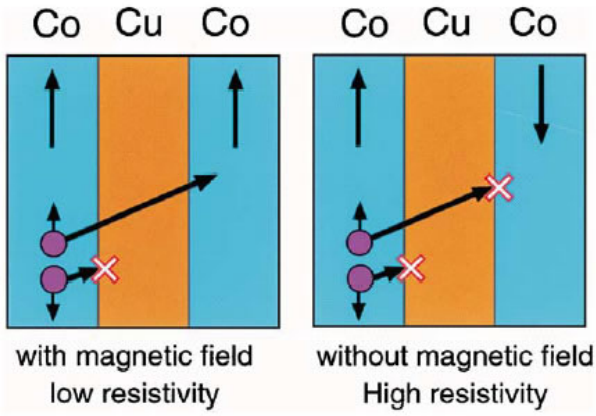

Figure 2.5: (from [48]) Schematic of a Co/Cu/Co trilayer, and illustration of the GMR effect. When a bias voltage is applied between the two Co layers, the spin up and down electrons in Co_{left} form two independent current channels to travel across the trilayer. Due to the potential barrier between the Co and Cu electrons, the spin down electrons are scattered back at the first interface, independent of the relative magnetisation orientations between the two Co layers. The spin up electrons in Co_{left} have much less difficulty to reach Co_{right} when the magnetisation of the two Co layers are parallel, as compared to the anti-parallel case. As a result, the resistance of the trilayer is minimum (maximum) when the magnetisation of the two Co layers are parallel (antiparallel).

are typically magnetic layers separated by a thin non-magnetic spacer.

Two such magnetic layers will interact through the mechanism known as interlayer exchange coupling. This is the coupling mechanism of nuclear magnetic moments or localised inner d shell electron spins in a metal by means of an interaction through the conduction electrons, and is described by Ruderman-Kittel-Kasuya-Yosida (RKKY) theory [42–45]. Perhaps the most significant application of the RKKY theory has been to the theory of GMR, which was first observed by Baibich *et al.* in 1988 [46]. GMR is generally described as interplay between spin dependent scattering in successive magnetic layers. The condition for this interplay is that the individual layer must be small compared to the electron mean free path. Conduction electrons flowing through a metal may collide with obstacles within the material and change direction. These obstacles include interfaces and defects in the sample, and vibrations of the crystal lattice (phonons) or of the electron spins in magnetic materials (magnons). Such scattering events cause electrical resistance, and so the more obstacles a sample contains, the higher its resistance will be [47].

MR occurs when an external magnetic field changes the scattering within the

material. The source of GMR is 'spin-dependent' scattering through magnetic layers. Depending on the magnetisation direction a magnetic metal layer will scatter carriers with 'up' or 'down' carriers, but not to the same extent. This is illustrated in figure 2.5, where we see that in the antiparallel case the electrical resistance is much higher because all of the conduction electrons will be scattered heavily, if not by one interface, then the next. In order to maximise the GMR response, it is necessary to somehow stabilise an antiparallel alignment between the FM layers. Spin valves offer a suitable way of doing this, for instance by having one magnetically 'hard' reference and one magnetically 'soft' free layer, where the free layer may be rotated by an external field, while the reference layer remains pinned in some way.

In this section we will present an overview of work on the structural and magnetic characteristics of epitaxial spin valves. We will also present some dynamic magnetic studies, and report on recent work on mirror domains in SV structures.

2.3.1 Structural & Magnetic Studies of Epitaxial Spin Valves

Growth and Structural Properties

Ercole and Samad [47, 49] studied very similar SV structures grown by molecular beam epitaxy (MBE) in UHV. These were Co/Cu/FeNi structures grown on a Cu buffer layer on a Si(100) substrate. The growth of a thick (∼50 nm) Cu buffer layer allows the fcc structure to be grown epitaxially on Hf-passivated Si substrates. These multilayers follow the epitaxial relation: Co(100)[001]‖ Cu(100)[001]‖ FeNi(100)[001]‖ Si(100)[011]. Lew *et al.* [50] grew a similar SV structure on GaAs(100), but depositing the Co layer first. They had NiFe/Cu/ Co/GaAs(100), and the epitaxial relation: NiFe(100)[001]‖Cu(100)[001]‖Co(100) [011]‖GaAs(100)[011], thus the Cu and NiFe layers were rotated by 45° in-plane with respect to the Co [001] axis.

In all of these cases, structural characterisation was performed *in situ* by Auger electron spectroscopy (AES) and RHEED. AES probes surface atomic species, and although spectra taken on the substrate showed traces of C and O peaks, these disappeared soon after the growth of the buffer or first layer. RHEED images of the substrate and each layer confirm epitaxy throughout the whole sample. In the case of the GaAs substrate, the RHEED patterns indicate

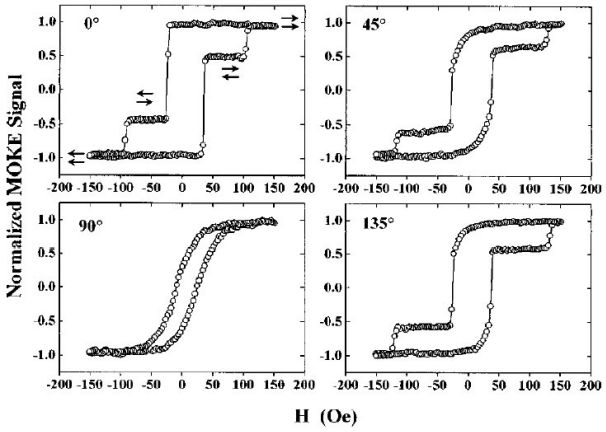

Figure 2.6: (from [50]) Hysteresis behaviour measured by MOKE magnetometry along the four principal axes of a SV with structure Cu/NiFe/Cu/Co/GaAs(100).

stabilisation of the bcc phase of Co(100), and fcc growth (after rotation) of the Cu spacer and NiFe top layer.

Magnetic Properties

The magnetic properties of SV samples have been studied using several methods, including MOKE, BLS, and PNR.

MOKE Typical MOKE magnetometry measurements of an epitaxial SV structure are shown in figure 2.6. The sharp switching and plateau regions are consistent with ideal SV behaviour, showing the switching of one, then the second FM layer. These MOKE loops reveal the presence of a fourfold cubic anisotropy, but a twofold uniaxial anisotropy also occurs. In this case, the uniaxial anisotropy is induced by the Co/GaAs interface. MOKE loops for the samples grown on Si do not display this uniaxial anisotropy, but only the fourfold cubic behaviour.

BLS Ercole *et al.* [49, 51] determined the relevant magnetic anisotropy fields of an epitaxial Co/Cu/FeNi SV on Si(100) substrate by BLS. The BLS data was fitted to a spin-wave theory assuming uncoupled magnetic layers, and calibrating layer thickness with PNR results. Thus, Ercole *et al.* [49, 51] were able to determine the cubic anisotropy constant, the in-plane uniaxial anisotropy constant, the effective demagnetising field, and the magnetisation of each FM layer. They

find that the anisotropy in the Co layer is predominately fourfold in character, and anisotropy constants provide further evidence of the high quality of the layer, as compared to values from the literature. Finally, low-temperature BLS on this sample revealed the presence of anti-ferromagnetic Co oxide, and the exchange coupling between this and the FM layer resulted in an increase in the spin wave frequency.

PNR The anisotropies of epitaxial SV samples are of mixed fourfold and twofold symmetry, which complicates their switching behaviour. PNR can provide the layer-dependent moments and allows vector magnetometry to determine the relative orientation of the layer magnetisation.

Bland *et al.* [52] used PNR combined with SQUID magnetometry to determine the interface and interior moments for each of the ultra-thin FeNi and Co layers in an epitaxial Co/Cu/FeNi SV structure. Upon fitting the data, they tried to fit the nominal structure but also used a model in which additional intermixed interface layers were introduced. They find that although the nominal model reproduces the features of the PNR data well in the low wave-vector range, it is not consistent with the total moment measured by SQUID magnetometry. With the interface model however, the fit closely reproduces all the features of the data very well. This was also the case for low temperature (1.5 K) PNR data. The interface regions are found to extend over a thickness of 9-11 Å, and to have significantly lower effective magnetisation than the corresponding values expected for FeNi and Co layers, which is consistent with chemical intermixing.

In continuation with this sample, Bland *et al.* [52] measured spin asymmetry spectra as a function of the relative layer magnetisation. This was done by applying a saturating field of 3 kOe in one direction, then reducing the field to 50 Oe, which is enough to switch the FeNi layer but not the Co layer magnetisation. This 50 Oe field was then rotated for measurements in the parallel, anti-parallel, and perpendicular cases. The spin asymmetry data display dramatic variations according to the direction of the applied field, and the fits follow the data closely, indicating that the FeNi magnetisation indeed rotates as a single domain to become aligned parallel to the applied field, and that to a good approximation the Co layer is unchanged, thus exhibiting real SV behaviour.

Patel *et al.* [53] took PNR measurements on an epitaxial SV which was also

also a Co/Cu/NiFe structure. They took PNR spectra for both the parallel and anti-parallel cases and fitted the data to obtain layer properties such as thickness and roughness, but also the magnetic moments of the thin films. Patel *et al.* [53] and Samad [47] observe a slightly reduced moment of the Co layer, which they attribute to intermixing. As above, their PNR fits were only poor when no intermixing was allowed, but greatly improved when 5 Å of FeNiCu or CoCu were introduced (in the fit) between the FM layers and the buffer and spacer, and between the Co layer and Cu cap.

2.3.2 Dynamic Hysteresis Behaviour in Epitaxial Spin Valves

Over the past decade, the dynamics of magnetisation reversal has attracted significant attention as a test of universality hypotheses, and scale-invariant descriptions of the energy loss per cycle as a function of external parameters. Several theories and models have tried to establish the relation between the hysteresis loop and these parameters, which are usually the applied field strength, frequency, and temperature. A number of experiments[5] have been performed to describe the dynamics of magnetisation reversal in various systems, but critical values obtained both *in situ* and *ex situ* significantly differ for different materials and different dynamical regimes. These discrepancies could be attributed to different measurement methods or to intrinsic differences in the dynamic response of the sample.

In order to test the universality of dynamic scaling behaviour in FM ultrathin films and to clarify the effect of magnetic anisotropy strength on the dynamic hysteresis scaling, Lee *et al.* [54, 55] studied fcc epitaxial NiFe and Co grown on Cu/Si(100). They take advantage of the striking difference in the cubic magnetocrystalline anisotropy fields, which differ by more than one order of magnitude, and study the behaviour of both layers in one SV sample. A further motivation in using an epitaxial SV sample is that it allows them to directly compare the dynamic reversal behaviour for ultrathin films deposited on the same substrate, with the same fcc structures, and under the same growth conditions. This largely eliminates uncertainties due to intrinsic differences associated with the substrate or growth conditions.

[5] *cf.* references 1-7 in reference [54].

Lee *et al.* [54, 55] study the reversal dynamics of their epitaxial SV, and compare it to the dynamic response of single NiFe and Co epitaxial layers. They find that the single NiFe and Co layers do exhibit different scaling behaviours as a function of sweep rate, and so expect distinct scaling behaviour in the case of the SV sample. At low sweep rates, the SV displays 'double switching', but this behaviour gradually becomes less clear as the sweep rate increases. The behaviour transforms to 'single switching' when the rate reaches ∼154 kOe/sec. This, and a similar transformation observed in a double SV sample, indicates a different dynamic response of the NiFe and Co layers to a time-varying magnetic field. Hence the authors conclude that the dynamic response to field sweep rate is dependent upon the magnetic anisotropy strength.

2.3.3 Mirror Domain Structures in Epitaxial Spin Valves

Several types of the interlayer coupling between two FM layers across a non-magnetic layer have been studied, both theoretically and experimentally. For metallic spacer layers, oscillatory interlayer exchange coupling has been observed, and for insulating materials a weak interlayer exchange coupling has also been reported[6]. Thomas *et al.* [57] address the influence of magneto-static coupling associated with the presence of domain walls in magnetic layers. They note that non-uniformity in a magnetised layer containing for instance a domain wall or vortex (*e.g.* during magnetisation reversal) induces stray fields which could give rise to coupling between the layers.

Lew *et al.* [56] investigated the effect of these domain wall stray fields, and the possible pinning effects that these might induce. To probe this pinning effect one of the magnetic layers in the sample must be magnetically hard and able to provide magnetically stable domains, and the other layer must be relatively soft towards the pinning field that arise from the hard layer. As high-quality films with low interface roughness are essential to minimise the effects of roughness-induced magneto-static coupling, the authors chose an epitaxial SV structure for this study.

Lew *et al.* [56] present GMR minor loops taken for different values of minimum applied field, but without ever completely switching the Co layer. As

[6] *cf.* references 1-4 in reference [56], and references 1-4 in reference [57].

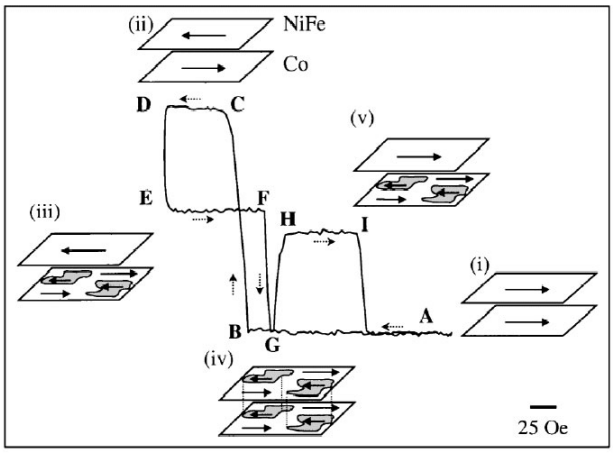

Figure 2.7: (from [56]) GMR loop of an epitaxial NiFe/Cu/Co SV, and schematics of magnetisation directions. Mirror domain structures as shown in schematic (iv) are induced in the structure at point *G*.

explained previously, the maximum and minimum resistance values correspond to the parallel and anti-parallel configurations, respectively. One notable feature which they observe is a drop in the resistance to its absolute minimum during the reversal of the NiFe layer. This is illustrated in figure 2.7, at point *G*. Starting from point *A*, where the magnetisation of the two FM layers are parallel, the applied field was then reduced to a negative value, where the soft NiFe layer began to switch, at *B*. By the time *C* is reached, the NiFe has become anti-parallel to the Co, explaining the rise in resistance. As the minimum applied field is slightly larger than the nucleation field of the Co at *D*, the magnetisation reversal is about to begin and a reverse domain evolves, at *E*, whereupon the magnetisation of the two layers are no longer completely anti-parallel, so the resistance value is decreased. The amount of this decrease depends on the fraction of the evolved reverse Co domains. As the field is increased again towards *F*, the NiFe magnetisation begins to switch, by evolving reverse domains, and at *G* the resistance suddenly drops to its minimum value. This is due to the formation of a unique parallel configuration in the tri-layer. This has both the NiFe and Co domains with the same magnetisation directions, perfectly mirroring each other. When the NiFe develops into a single domain state at *H* the unique configuration is lost but the two FM layers are still partially anti-parallel to each other (as the Co remains in domains) so the resistance value increases again, until *I*, where

the Co magnetisation switches back to a single domain state, in the direction of the applied field, thus creating the parallel configuration again. By varying the minimum applied field, the authors observed different fractions of reverse Co domains, each yielding specific resistance decreases at the position of point *E*. However, they always observed the reduction to the minimum (at *G*) during the NiFe reversal.

Lew *et al.* [56] also observe the pinning due to domains in the Co layer through MOKE magnetometry, and by varying the minimum applied field. In this case, they observe two-step switching of the NiFe, as it is trapped by the pinning field created by the Co domain walls. Here again, they are able to switch increasing fractions of the Co film, and observe their proportion by the position of the step in the NiFe switching. However, they find that the domain wall width being dependent on anisotropies and material stiffness, the mirror domain behaviour does not occur in *e.g.* fcc Co-based SV samples. In conclusion, they have observed long-range domain wall pinning through a thick spacer layer, which is induced by mirror domain configurations in certain SV structures.

Conclusion and Outlook

In this chapter, we have presented an overview of past and current work with epitaxial samples. In the case of the Fe/GaAs system, there have been numerous experimental and theoretical studies, which provide a useful insight into magnetic properties, such as the evolution of the anisotropies and spin dynamics at very low coverage. These will be critical in device applications where interface morphological effects might govern important parameters such as the spin injection efficiency.

We have also reviewed epitaxial spin valve structures, presented their structural and magnetic properties. Spin valve structures are already widely used in devices such as hard-drive read heads, but due to production requirements these are polycrystalline at best. Epitaxial spin valves however provide a excellent system in which to investigate fundamental properties of ultra-thin magnetic film behaviour.

When growing and studying such heterostructures and multilayers, we will have to consider the various fundamental effects and properties described here.

Chapter 3

Experimental Techniques

Introduction and Outline

In this chapter we will present an overview of the principle experimental techniques used throughout the course of work for this thesis. Further specific methods will be briefly described as necessary in each of the following chapters. Here we will focus on the ultra-high vacuum chamber system, magneto-optical Kerr effect magnetometry, and the X-ray techniques which we used several times during our work.

3.1 The Ultra-High Vacuum System

3.1.1 Overview of UHV

Reasons for UHV

Ultra-High Vacuum is the pressure regime characterised by pressures below 10^{-8} mbar. At such pressures, the mean free path of a molecule inside the chamber is much larger than the chamber size (>1 km), and there are less than 10^{10} molecules per cm^3 in the chamber. Gas molecules will collide with the chamber walls many times before colliding with each other, therefore almost all interactions take place at the various surfaces inside the chamber.

Any experiment requiring collision-free environments or clean surfaces will necessitate UHV. Such applications include electron microscopes, evaporation and coating, and materials testing for space. In our case, for epitaxial growths

and interface studies, we require a sample surface which is clean and known. The need for UHV arises from the time required for a monolayer to form on a surface at that pressure. At 10^{-9} mbar, this is calculated as being ∼2000 seconds; about half an hour [58]. In general, this time is longer than the time required to take a measurement, thus allowing us to probe clean surfaces, and obtain the highest-quality interfaces.

Obtaining UHV Pressures

Cleanliness and Choice of Materials in the Chamber The attainment of UHV conditions is a delicate task. Careful design of the chamber and pumping channels is required, and only certain materials with low vapour pressure such as stainless steel and ceramics should be used in the chamber. During use, it is common to chill the chamber walls to cryogenic temperatures, in order to further reduce outgassing. Special seals at windows and flanges should be used to prevent leakage. These all-metal seals consist of two knife edges cutting into a soft Cu gasket, and can in theory maintain pressures down to 10^{-12} mbar. When the chamber is pumped down after being exposed to air, it must be baked at ∼200°C for several hours to remove water and/or hydrocarbons adsorbed to the walls. It is critical to avoid all traces of hydrocarbons, including skin oils from a fingerprint in the chamber, and hence to always wear gloves when handling UHV equipment.

Pumping Techniques The pressure inside a vacuum chamber will be a balance between the pumping speed and the leak/outgassing rates. High pumping speeds are necessary as small leaks are unavoidable. Any material will tend to outgas, and also the chamber walls are often permeable, to a certain extent, to the lighter constituents of the atmosphere. There is no single vacuum pump which can operate from atmospheric pressure down to UHV. Therefore, the required pumping capacity and speed will be achieved through multiple vacuum pumps in series and/or parallel. In our system, the first stage of pumping is achieved by a rotary pump, which backs a diffusion pump. An ion pump and titanium sublimation pump are also used in the UHV pressure regime.

Rotary pumps are the most common mechanical pumps. The simplest design of these is a circular rotor rotating inside a larger circular cavity, with the narrow

space between the moving and stationary parts being sealed by oil. Spring-loaded blades slightly off-centre create two cavities of different volumes, and this system forces gas out of the pump with each rotation. Rotary pumps are often used as backing pumps. The ultimate pressure for rotary pumps is typically $\sim 10^{-4}$ mbar, which is an easily sufficient roughening pressure before high-vacuum pumps can take over.

With no moving parts, the diffusion or vapour-jet pump is one of the most reliable designs of high-vacuum pumps. A diffusion pump can operate from pressures of $\sim 10^{-2}$ mbar and into the UHV pressure regime. The typical diffusion pump consists of a vertical body fitted with a boiler at the bottom and cooling coils around the top two thirds. In operation, a vapour of oil is created by electrical heating and this is ejected through a nozzle down against the water-cooled walls of the pump body. Gas molecules in the vapour jet are given downward momentum. The gas-vapour mixture travels downwards, and the vacuum oil is condensed on the cooled walls. The gas molecules continue their path downwards where they are removed by the mechanical backing pump. The condensed oil vapour returns to the boiler and is re-vaporised for the following cycle [58]. One major disadvantage of diffusion pumps is the tendency to back-stream oil into the vacuum chamber. This oil can contaminate surfaces inside the chamber or upon contact with hot filaments or electrical discharges may result in carbonaceous or siliceous deposits. Often cold traps and baffles are used to minimise back-streaming, although this results in some loss of pumping ability [45].

Ion pumps are also very reliable as they have no moving parts. However their operating range only begins at pressures $\lesssim 10^{-8}$ mbar. Electrons trapped in a magnetic field and accelerated in between an anode and cathode ionise gas molecules by collision. This generates both an electron and a positive ion. The ions are accelerated to the cathodes, typically made from a chemically reactive metal such as titanium, and are neutralised. The electron produced in the original collision contributes to ionising further gas molecules.

Sublimation pumps are also 'getter' pumps, which trap gas molecules on reactive surfaces. These deposit a film of metal on selected surfaces, either continuously or periodically. Titanium is the preferred metal, and is deposited by sublimation from a high-temperature filament source. The removal of gas by a sublimation pump involves a process of chemisorption on a titanium surface.

The probability of a reactive gas atom or molecule being adsorbed on first impact on an atomically clean titanium surface is between 0.1 and 1, depending on the particular gas [58]. The upper pressure limit for operation of a sublimation pump is defined by the time necessary to form an absorbed monolayer, and they become ineffective at pressures $\gtrsim 10^{-4}$ mbar.

Measurements of Vacuum

Similarly to pumps, no single gauge can measure pressures ranging from atmospheric to UHV. In our chamber, we use a Piriani gauge at roughening pressures and an ion gauge in the UHV regime.

A Piriani gauge is an indirect measure of the pressure, as it does not measure the pressure directly, but a change in the property of the surrounding gas. In the case of a Piriani gauge, a sensing filament producing heat is surrounded by the gas to be measured. As the pressure changes, the thermal conductivity changes, thus varying the temperature of the sensing filament, which then can be related to the pressure.

Also an indirect measure of vacuum, ionisation gauges are the most sensitive gauges for very low pressures. In ion gauges, thermionic emission generates electrons, which collide with gas atoms and generate positive ions. The ions are attracted to a biased collector electrode, and the current in the collector is proportional to the rate of ionisation, which is a function of the pressure in the system. Hence, measuring the collector current gives the gas pressure [45].

3.1.2 The 'Big' Chamber

Overview

The UHV chamber described here and used for the work carried out in this thesis is usually referred to as the 'Big' chamber in the Thin Film Magnetism and Materials (TFMM) group. Two views from either side of the chamber are shown in figure 3.1. Here we see the extensions of the chamber, which include evaporators, LEED, RHEED, an attached STM chamber, and also MOKE and BLS windows. The chamber contains a magnet capable of producing a 2 kOe field *in situ*.

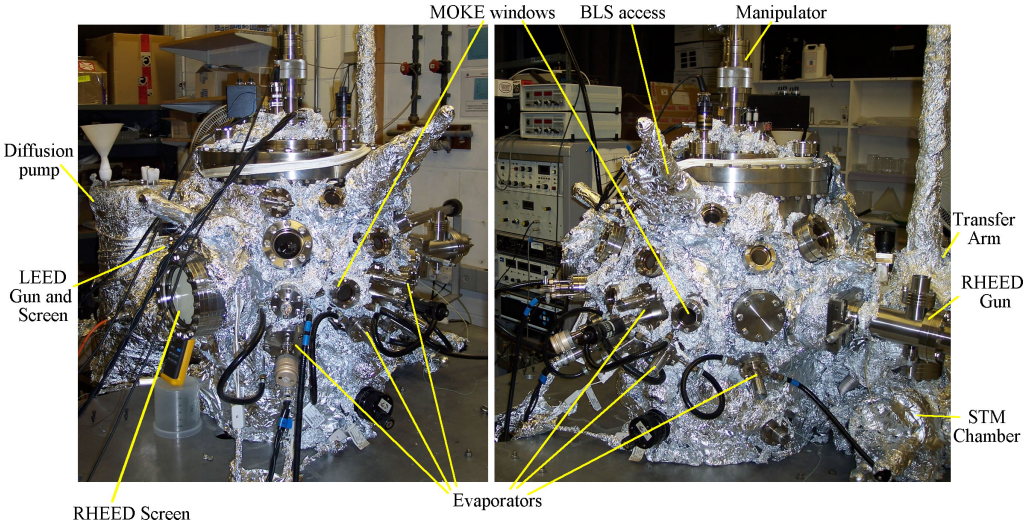

Figure 3.1: The 'Big' chamber. The aluminium foil insulation wrapping is used in the baking cycles.

The Manipulator and Sample Holder

The manipulator and sample holder are central to the use of the chamber. A rotation around the vertical axis of the chamber allows us to direct the sample surface to face any of the evaporators or instruments. The second rotation capability, in the plane of the sample, enables orientation-dependence of all the *in situ* characterisation measurements. Both of these are controlled by mechanical feedthroughs at the top of the chamber (figure 3.1). The large manipulator flange also contains several electrical feedthroughs, for sample heating, temperature measurement, and also a mass-spectrometer.

The sample holder is a copper block on which we attach the substrate with tantalum clamps. We usually insert a thin tantalum sheet in between a semiconductor substrate and the copper sample holder to avoid any segregation of Cu into the semiconductor during heating cycles. In order to insert a sample into the UHV chamber without venting it to air, the prepared sample holder and sample are first loaded into a load-lock, which has a small volume and can be pumped down from atmospheric pressure to $\sim 10^{-9}$ mbar within $\sim$2 hours. Once the pressure in this transfer arm is low enough, we open a gate valve to the chamber, and although this causes a pressure spike, the chamber recovers in a few hours. With the transfer arm valve open, we can slide the sample onto the manipulator,

where we secure it by screwing it on a thread stub.

Substrate heating is achieved in two stages. Running a current through a tungsten filament surrounding the sample holder stub on the manipulator will bring the copper block up to ∼200°C. This is the temperature at which we usually originally degas the sample holder and substrate. In order to reach annealing temperatures, we can apply a positive high voltage to the sample holder. This will accelerate electrons from the hot filament and create an electron-beam to the sample holder. This enables us to reach temperatures of up to ∼600°C.

3.1.3 Sample Growth

Evaporators

Similarly to the sample heating, the evaporators heat the source material using an electron beam, whereby a high-voltage accelerates electrons from a hot filament to the source. When heated, certain materials will melt and then evaporate, but others will sublimate directly from the solid to gaseous state. This is the case for *e.g.* Fe, Co, and Cr. For such materials, the high voltage can be applied directly to the source. This is usually a high-purity (99.99+%) rod or flake of the source material which is connected to the high-voltage feedthrough of the evaporator. In the case where the material initially melts, we must use a crucible, or boat, to heat up and contain the molten metal. Such materials are *e.g.* Cu and Au. The crucibles for these evaporators have to be machined from a metal (in order to accelerate the electrons) and it must have a significantly higher melting point than the material we want to evaporate. Crucibles are typically machined from Mo or Ta. Evaporation from a crucible also enables us to grow semiconductors and insulators, as we have done with Si and MgO.

The enormous heat produced by an evaporator will be detrimental to the pressure in the vacuum chamber. As we have discussed, heating walls and components in UHV will cause them to outgas more. Therefore each evaporator is enclosed in a water-cooled shield. This has two purposes, in containing the heat, and also directing the evaporation flux towards the sample.

Growth Rate

The evaporation rate can be controlled by varying the high-voltage applied to the source material or its crucible. In order to quantify the flux rate, we first direct it onto a quartz microbalance crystal. A frequency counter connected to this displays the oscillation frequency of the crystal. As material is deposited, the crystal mass increases, and the oscillation frequency drops. Using previously established calibration tables,[1] we are able to determine and control the rate of evaporation of the material, and hence estimate the time required to reach the desired thickness. Unfortunately, with the current set-up of the manipulator and sample holder, it is not possible for us to grow the film and calibrate on the quartz crystal at the same time, as the substrate and microbalance are back-to-back. Therefore, we must establish the rate, expose the substrate for a determined length of time, and re-calibrate the rate after deposition.

The error in this system can be quite large, especially in two cases. Firstly, if we want a very slow growth or if the evaporated material has a low density, the calibration using the frequency counter lacks accuracy. Indeed, if a drop of several Hz takes several minutes, we require an extensive calibration time. The second case where this method proves inaccurate is for thicker films, requiring long growth periods. In this case, variations of the evaporation flux will cause the actual thickness to differ from what is sought. In order to minimise this effect, we often check the evaporation rate mid-growth for thicker films.

Growth on a Patterned Substrate

In addition to films, we have also grown layers on polymethyl methacrylate acrylic (PMMA)-patterned GaAs substrates. PMMA used as a resist can be patterned by electron beam, deep ultra-violet light, or X-rays. Exposure to these creates chain scission in the PMMA, and enables subsequent selective removal of the exposed area by a chemical developer. PMMA allows for extremely high resolution patterns to be made [45].

In order to control the eventual contamination of the chamber during the evaporation on a PMMA-patterned substrate, we monitored the ion gauge pres-

[1] These were established by atomic force microscope (AFM) and X-ray reflectivity (XRR) measurements.

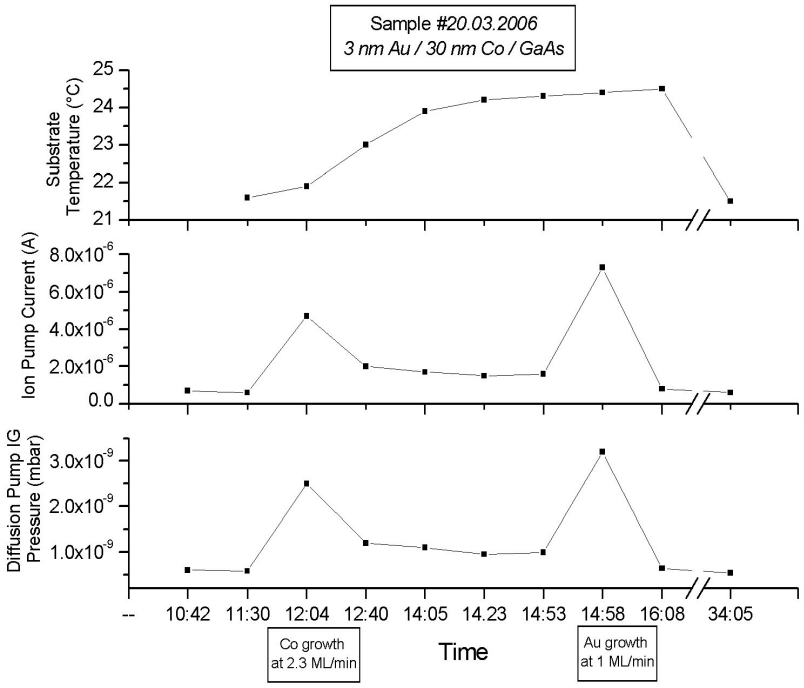

Figure 3.2: Sample ♯*20.03.2006*; Growth on a PMMA-patterned substrate. Evolution of the (a) substrate temperature; (b) ion pump current; and (c) ion gauge pressure reading. The final point at 34:05 hours is taken the morning after the growth.

sure closely, as well as the partial pressures of residual gases throughout the growth. In our case, the substrate had been patterned by electron-beam, and had therefore already been exposed to vacuum, but the heat generated by the evaporators and the material flux could potentially release the acrylic into the chamber.

The data collected during this growth is shown in figures 3.2 and 3.3. We note that in both of these figures, the final point at 34:05 hours corresponds to data taken the morning following the growth, after the chamber had recovered overnight. As one concern was the heating, and degradation of the PMMA, we did not thermally treat the substrate prior to the growth. Furthermore, we monitored the substrate temperature during the entire growth process. As we see in figure 3.2(a), the substrate temperature rises only slightly to 24.5°C due to the evaporators' heat.

The pressure variations throughout the growth recorded by the ion pump, ion gauge, and mass spectrometer follow each other closely. The two peaks

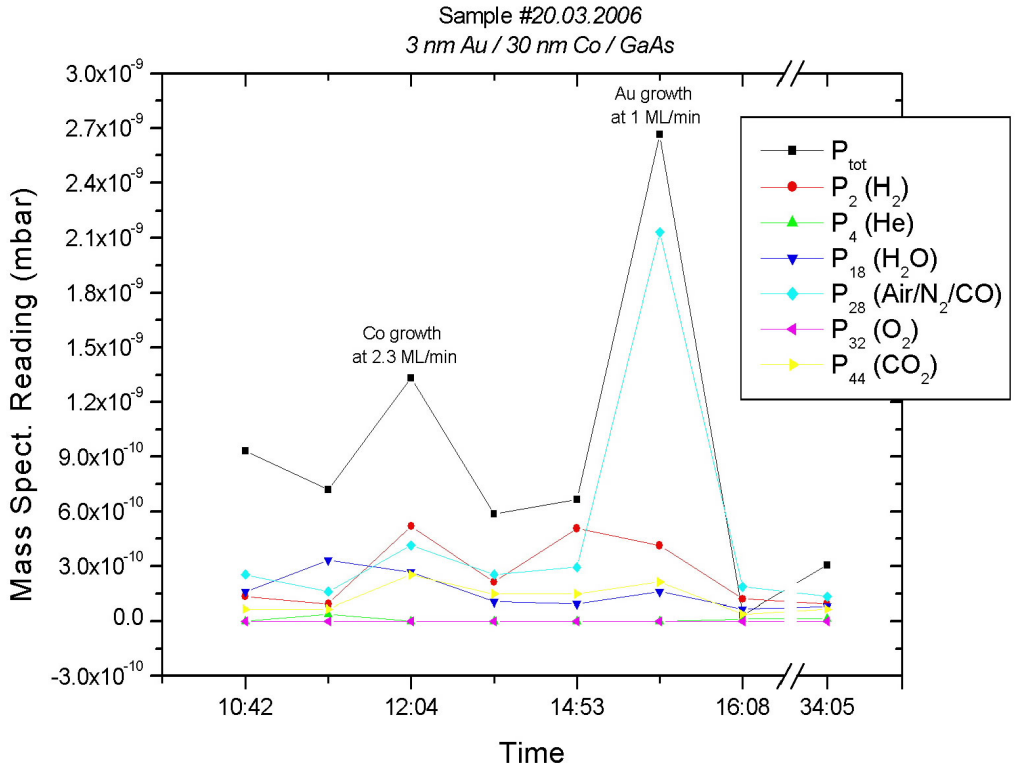

Figure 3.3: Sample ♯*20.03.2006*; Partial pressures of selected residual gases during a growth on a PMMA-patterned substrate, as indicated by the mass spectrometer readings. The final point at 34:05 hours is taken the morning after the growth.

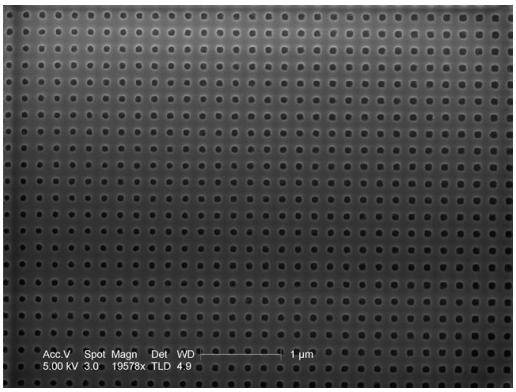

Figure 3.4: SEM image of an anti-dot array in a Hall bar. The dot size is 100 nm, and the film is 3 nm Au/30 nm Co/GaAs. SEM image courtesy of Tiejun Meng, Semiconductor Physics Group, Cambridge.

present correspond to the switching on of the Co and Au evaporators. In the first instance, upon being heated the source material will outgas water and air trapped in the source. In this case, we see from the mass spectrometer readings in figure 3.3 that N_2 or CO_2 are the dominant gases which are being released. We also see that the outgassing of the Au source is significantly stronger than that of the Co rod. This is due in part to the chemical properties and softness of Au, but also the aforementioned fact that Au melts before evaporating, thus enabling it to trap and release more gas bubbles than in the case of sublimation. As soon as the evaporator is switched off, the source stops outgassing, and the chamber rapidly recovers to its base pressure in the 10^{-10} mbar range.

For this specific sample, we grew a 30 nm Co layer and capped it with 3 nm Au. The pattern was a 30 μm $\times$ 10 μm Hall bar with an anti-dot array, with features in the PMMA pattern as small as 100 nm. Liftoff for such small features was not always successful for the whole Hall bar, and depends on the PMMA thickness and electron-beam exposure. A scanning electron microscope (SEM) image of a successful liftoff region is shown in figure 3.4. Our conclusions regarding the chamber were that the growth on a PMMA-coated substrate did not affect the vacuum or contaminate the chamber.

3.1.4 *In situ* Characterisation

A surface can be defined as a boundary between materials and a vacuum. Nowadays, a wide variety of diffraction, spectroscopy, and microscopy techniques are available for the characterisation of thin films and surfaces. Here we will present the techniques of RHEED and LEED, which we used *in situ* to characterise our surfaces and films.

The origin of diffraction patterns from a crystal are most easily understood by the use of a reciprocal space lattice and the Ewald sphere construction. If a 3D crystal is defined by the primitive vectors $\mathbf{a}$, $\mathbf{b}$, and $\mathbf{c}$, we have the corresponding reciprocal lattice defined by $\mathbf{a}^*$, $\mathbf{b}^*$, and $\mathbf{c}^*$. For an incident plane wave with wave vector $\mathbf{k}_0$, there will be a set of diffracted waves from the crystal with wave vector $\mathbf{k}'$ defined by $\mathbf{k}' - \mathbf{k}_0 = \mathbf{g}$, where $\mathbf{g}$ is a reciprocal space vector (*i.e.* $\mathbf{g} = h\mathbf{a}^* + k\mathbf{b}^* + l\mathbf{c}^*$, where h, k, l are integers). This defines the condition for diffraction maxima, and is a statement of the normal Laue diffraction conditions. The diffracted beams in the backward direction are referred to as Bragg maxima, and in the forward direction as Laue maxima [59].

Reflection High-Energy Electron Diffraction

RHEED was first used by Miyake in 1937 and has since then been widely applied to monitor thin films during and after deposition. Figure 3.5 shows the scattering geometry of RHEED. The incident electron beam strikes the sample surface at a grazing angle of 1-3°. The electron beam energy can range from a few keV to 1000 keV, though in our system we always set the beam energy to 12-15 keV. The electrons then diffract onto a phosphorescent screen positioned opposite the electron gun. On this screen we can observe and capture the diffraction pattern, which might be spots, streaks, or half-rings.

There are several possible sources for producing streaks perpendicular to the surface on RHEED patterns. The first is the small penetration depth of the beam into the crystal surface, which is equivalent to sampling a thin sheet crystal which is thin in the direction nearly perpendicular to the incident beam. The other source is surface morphology and disorder, which produce reflections that do not fall on the position of Bragg maxima. Finally, the curvature of the Ewald sphere for electron energies of a few tens of keV is significant, also giving rise to

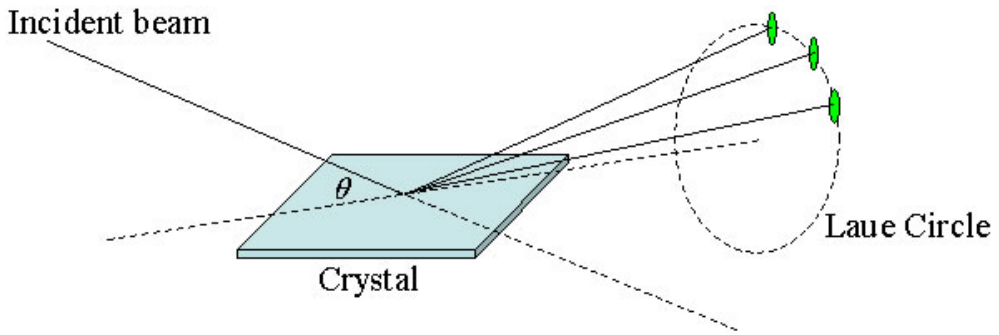

Figure 3.5: Schematic of RHEED apparatus and diffraction from a crystal surface. The angle of incidence θ is usually constrained to a few degrees in order to limit the penetration of the electrons into the bulk.

streaks in the RHEED pattern [60].

Low-Energy Electron Diffraction

LEED electrons are at a much lower energy than those used in RHEED, typically $80 - 150$ eV. These are accelerated to the sample surface and back-scattered through a series of grids. The scattered electrons may have been elastically or inelastically scattered, though only the former are used in the case of LEED. A schematic of the LEED apparatus is shown in figure 3.6, where we see the three detection grids. The first grid is at the potential of the sample (earthed), but the second is held at a potential close to the beam voltage so that only elastically scattered electrons can pass through it. The inelastically scattered lower-energy electrons are stopped. The final grid may be positively charged to accelerate the accepted electrons onto the fluorescent screen, which will also be held at a high voltage $\sim$5 kV to allow for the excitation of the phosphor. We note that in LEED, the electrons diffract off the surface layer almost exclusively, due to their low energy, and so do not provide information on the bulk structure of the crystal, but can be very powerful to recognise surface crystallography *e.g.* surface reconstructions [59, 61].

Magnetic Characterisation

As we have mentioned above, our UHV chamber contains a magnet capable of applying a 2 kOe field in the plane of the sample. This enables us to perform

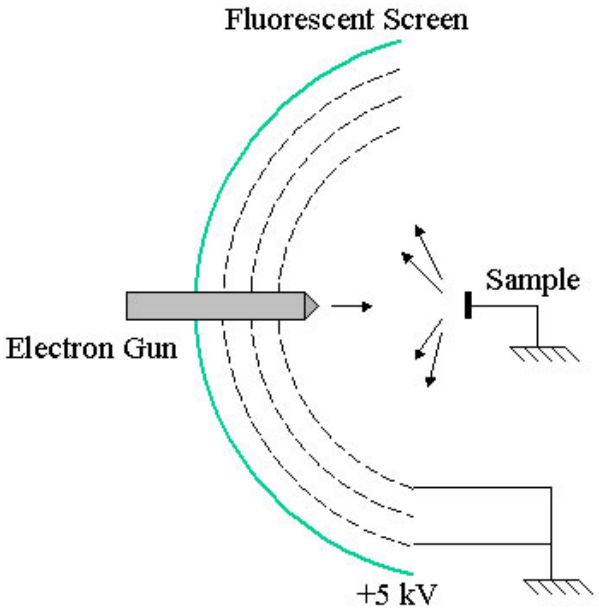

Figure 3.6: Schematic of LEED apparatus. The potential of the second grid is held close to the beam voltage so that only elastically scattered electrons can pass through it.

in situ magnetic characterisation measurements at the different growth steps of samples. The two *in situ* techniques we have used in our UHV chamber are MOKE and BLS.

***In situ* MOKE** The principles of MOKE will be discussed in detail in section 3.2.1 below. The basis of the experiment lies in the detection of polarisation rotation of light due to the magnetisation of a reflective surface. The laser, focussing and polarising optics, and detector are all on the outside of the chamber. All we require is for the beam to be reflected off the sample surface inside the chamber. This is done through the UHV viewports seen in figure 3.1, which specifically angle out from the magnet gap position at the manipulator.

There are two main challenges when taking MOKE measurements on a sample in a UHV chamber. The first, as with any optical set-up, concerns the alignment. As it sits in the chamber, the sample can be rotated in three dimensions, but its movement is still very limited as it must remain in the magnet gap, and the beam must be reflected through the viewport. The second obstacle regards the conservation of the beam polarisation as it passes through the UHV viewports. Typical

UHV viewports are glass sealed in the UHV flange mounting. Unfortunately this seal can produce an uneven force throughout the viewport. In addition to this, upon tightening the flange to the chamber we may also induce uneven forces in the viewport. This stress will not damage the glass, but may have depolarisation effects on passing light by introducing stray birefringence.

***In situ* BLS** BLS requires the collection of back-scattered light from the sample. For the *in situ* set-up, the beam enters the chamber through a lens and viewport mounted on bellows (unfortunately wrapped in Al foil in figure 3.1). The lens on the bellows allow us to focus the incident beam onto the sample and collect the back-scattered light. The energy shift of the back-scattered light is then detected and determined *ex situ*.

3.2 Magnetic Characterisation

3.2.1 Magneto-Optical Kerr Effect Magnetometry

Our understanding of magneto-optical effects is historically rooted in the work of Michael Faraday (in 1846) and of Rev. John Kerr (in 1877), who were the first to study the influence of magnetised media on the polarisation of transmitted and reflected light, respectively. The surface-MOKE effect made its debut as an experimental technique to study magnetism in 1985, when it was first used to detect ferromagnetic hysteresis loops from epitaxial Fe deposited on Au(100) [62].

Theoretical Formalism

Macroscopically, the Kerr effect can be described by off-diagonal terms in the dielectric tensor ϵ. In the case where the incident light and magnetisation are both along the surface normal, we have:

$$\epsilon = N^2 \begin{pmatrix} 1 & iQ & 0 \\ -iQ & 1 & 0 \\ 0 & 0 & 1 \end{pmatrix}, \tag{3.1}$$

where N is the refractive index and Q is the magneto-optical constant (Voigt constant) of the medium. The light entering the magnetised medium can be decomposed into beams that contain exclusively left- or right-circularly polarised modes. Different indices of refraction n are assigned to these two modes and we have:

$$n = N(1 \pm gQ), \tag{3.2}$$

where g is the direction cosine between the propagation vector of the light $\mathbf{k}$ and the magnetisation direction $\mathbf{M}$. The two circular modes travel with different velocities, attenuate differently, and upon emerging from the medium in reflection they recombine to yield a rotated axis of polarisation.

On a microscopic level, MOKE is a consequence of the interaction between the electro-magnetic wave comprising the light and the electrons in the medium. The electrons in the material are coupled to the internal magnetic field which leads to a change of the electro-magnetic wave. The following formalism of the magneto-optical (MO) effect is based on [63] and [64].

Let us first consider the case of a single layer and light travelling from medium 1 into medium 2, where the xy-plane is the boundary between the two media. Expressed in terms of the electric fields of the incident (i) and reflected (r) waves we have:

$$F = \begin{pmatrix} E_x \\ E_y \\ H_x \\ H_y \end{pmatrix} = AP = A \begin{pmatrix} E_s^{(i)} \\ E_p^{(i)} \\ E_s^{(r)} \\ E_p^{(i)} \end{pmatrix}, \tag{3.3}$$

where E_x, E_y and H_x, H_y are the tangential components of the light's electric and magnetic fields, respectively. The 4×4 matrix A which connects the column vectors F and P is called the medium boundary matrix. The elements of A are constructed from the geometric angles of the problem and from the N and Q values of the medium. The boundary condition across the single boundary in the 2-medium case requires:

$$A_1 P_1 = A_2 P_2. \tag{3.4}$$

If there is more than one boundary, the wave propagation inside the medium

at a penetration depth z from the interface is described using the medium propagation matrix $\overline{D}$, and we can write

$$P_2(z=0) = \overline{D}_2(z)P_2(z). \tag{3.5}$$

If we consider a multilayer system of l layers, noting i the initial medium, and f the final layer, or the substrate. For the l layers we have:

$$A_i P_i = \prod_{m=1}^{l} (A_m \overline{D}_m A_m^{-1}) A_f P_f, \tag{3.6}$$

which we can reformulate as $P_i = MP_f$ with

$$M = A_i^{-1} \prod_m A_m \overline{D}_m A_m^{-1} A_f \equiv \begin{pmatrix} G & H \\ I & J \end{pmatrix}, \tag{3.7}$$

and the 2×2 matrices G and I can be used to obtain the Fresnel transmission and reflection coefficients t and r, as:

$$G^{-1} = \begin{pmatrix} t_{ss} & t_{sp} \\ t_{ps} & t_{pp} \end{pmatrix} \quad \text{and} \quad IG^{-1} = \begin{pmatrix} r_{ss} & r_{sp} \\ r_{ps} & r_{pp} \end{pmatrix}. \tag{3.8}$$

Finally, the Kerr rotation ϕ' and ellipticity ϕ'' for s- and p- polarised light can be expressed as:

$$\phi_s = \phi'_s + i\phi''_s = r_{ps}/r_{ss} \quad \text{and} \quad \phi_p = -\phi'_p + i\phi''_p = r_{sp}/r_{pp}. \tag{3.9}$$

Details of the matrices A and $\overline{D}$ are given in reference [64].

Experimental Details

There are three geometries which are most commonly used for MOKE, illustrated in figure 3.7. These are the longitudinal, transverse, and polar geometries. In the longitudinal geometry, the film magnetisation lies in-plane, and parallel to the plane of incidence of the light. The field is also in-plane for the transverse geometry, however the magnetisation is now perpendicular to the plane of incidence. Finally, in the polar geometry the film magnetisation is along the surface normal. In theory the magnetisation can be in any arbitrary direction, but these

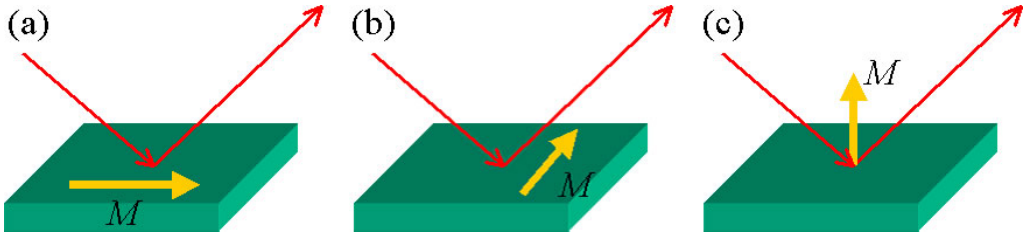

Figure 3.7: Geometries for MOKE measurements: (a) longitudinal; (b) transverse; and (c) polar.

three geometries simplify the algebra in describing the interaction. Further simplification is realised by considering only p- or s-polarised light, for which the polarisation vector is in the plane of incidence or perpendicular to it, respectively.

We used a stabilised Melles-Griot^{TM} HeNe laser operating at 632.8 nm. A schematic of the set-up is shown in figure 3.8. The laser light is already linearly polarised but we enhanced the degree of polarisation, and hence the s-component selectivity, by passing it through a first polariser P1. The light is then focussed on the sample, and the reflection passes through a second polariser P2 before being focussed on a photodiode. The sample sits in between the pole-pieces of an electro-magnet capable of producing a 2 kOe field, and can be rotated in the field.

In the longitudinal and polar geometries, the magnetisation of the sample surface changes the polarisation of the reflected light[2]. In these cases, the film magnetisation gives rise to a modulation of the p-component of the reflected light. In our experiments, polariser P2 is rotated 0.5-1° away from the extinction point (P1 and P2 crossed) in order to maximise the signal-to-noise ratio. Indeed, it has been shown that the quantity $\Delta I/I$, which is the difference in intensity between the light amplitudes for opposite magnetisation divided by the average amplitude, peaks at a very small angle $\sim$1°[66].

[2]In the transverse geometry there is no change in the polarisation of the reflected light as there is no component of the light propagating along the magnetisation direction. Transverse MOKE involves only a small change in the reflectivity, hence the intensity of the reflected beam, upon magnetisation reversal for p-polarised light [62, 65].

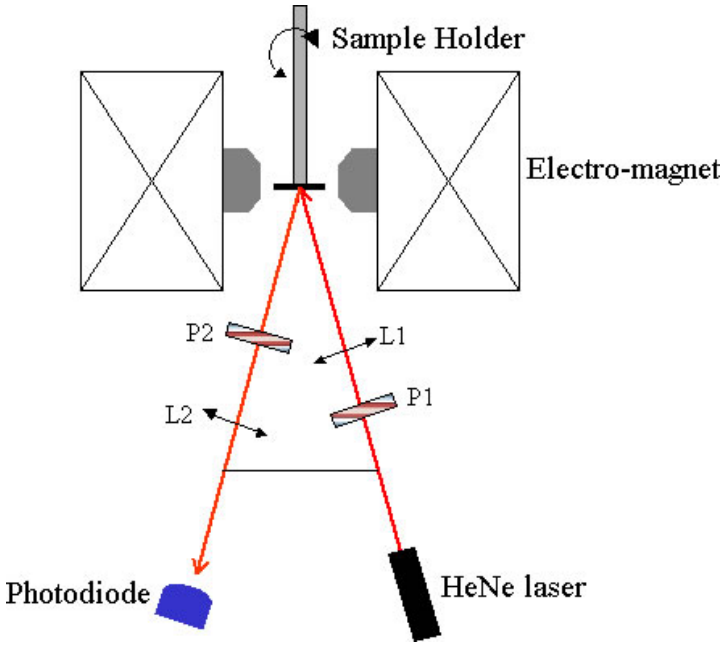

Figure 3.8: Schematic of the longitudinal MOKE set-up. The sample can be rotated in the field.

3.2.2 PNR and SQUID

The following overview of the PNR technique is adapted from *Polarized Neutrons* by Williams [67]. The method of measuring the critical reflection of polarised neutrons to obtain information on the depth profile of surface magnetism was pioneered at the Argonne National Laboratory by Felcher in 1981. An evaluation of the neutron reflectivity of a surface at angles slightly greater that the critical angle θ_c provides a very sensitive probe to the way that the refractive index n changes as a function of its distance z from the surface. For polarised neutrons and magnetic materials, n takes two values, one for polarised neutrons parallel, and one for polarised neutrons antiparallel to the direction of the magnetic induction in the material. Knowing this we can determine the two distinct spin reflectivities, which are finite and detectable at glancing angles of incidence.

A SQUID is formed from a superconducting loop containing at least one Josephson junction[3]. If the loop encloses some magnetic flux, there must be some circulating current because it is superconducting. This current consists of

[3]Josephson Effect: Current flow across two weakly coupled superconductors, separated by a very thin insulating barrier, for example.

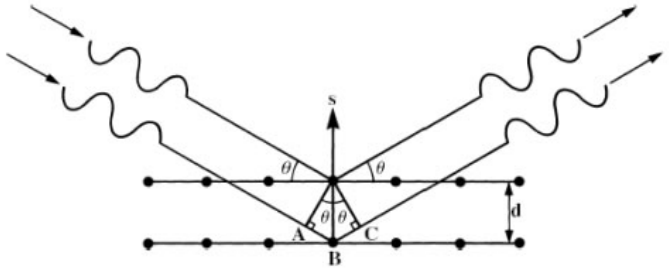

Figure 3.9: Illustration of Bragg's law of diffraction from a crystal with inter-plane spacing d. Constructive interference occurs when $AB + BC = n\lambda$.

Cooper pairs[4] whose wave functions form standing waves around the ring. There is a phase discontinuity across the junction, which is a function of the current flowing and hence of the magnetic flux [68].

3.3 X-Ray Diffraction and Reflectivity

X-rays are made by accelerating electrons from a W filament onto a target which is usually Cu. This process is very inefficient, generating mostly heat, some white radiation, but also some radiation at a characteristic wavelength, typically Cu K_α for which $\lambda = 1.5418$ Å. X-ray diffraction (XRD) and XRR are powerful tools to determine the crystal structure and layer properties in thin film samples. XRD can provide information on crystalline orientation and XRR will yield layer thickness and roughness data. We have used both of these techniques to characterise samples throughout the course of this work. All of these measurements were performed on a Philips X'Pert Pro^{TM} high-resolution diffractometer at the Department of Materials Science and Metallurgy, University of Cambridge. Here we will present an overview of the principles of XRD and XRR.

3.3.1 X-Ray Diffraction

Bragg's law, illustrated in figure 3.9, is the condition for constructive interference from a series of planes, and can be expressed by the simple relation:

[4]Cooper electron pairs: Bound pairs of electrons with boson-like behaviour to which superconductivity is attributed.

$$2d\sin\theta = n\lambda, \tag{3.10}$$

where d is the interlayer spacing, θ is the angle of incidence, λ is the incident wavelength, and n is an integer. Thus, by varying the incident angle[5] θ, we can determine the interlayer spacing.

There are three diffraction peak properties that will provide information on the measured sample. These are the position, intensity, and profile, commonly referred to as the 'P-I-P'. All three of these are dependent on the instrumental parameters but also various properties of the sample, and each can be useful in different applications of XRD.

Peak Position A peak occurs at a point of constructive interference. As we have seen, the peak position is controlled by the repeat distance in the sample, and the wavelength. Determination of the peak position will therefore be useful in applications such as the determination of lattice parameters, phase identification and film strain. In high-quality films or super-lattices it is also possible to extract thickness information from fringe peaks.

Peak Intensity The peak intensity is related to the structure factor. This is a mathematical description of how the crystal scatters incident radiation, which depends on the hkl Miller indices of a given reflection. The intensity also depends on the type and position of atoms, and the amount of the sample in the path of the X-ray beam. The intensity will provide information on the chemical composition, crystallinity and crystalline defects of the sample.

Peak Profile Finally, the peak profile or width is inversely proportional to the crystallite size, or the dimension D_{hkl}, perpendicular to the hkl plane[6]. If this is very small the peaks will broaden. The peak profile is determined by the sample perfection, and provides information on the crystallinity, crystallite size and crystalline defects.

[5] In Laue diffraction, the wavelength λ is varied, at fixed θ.

[6] The Debye-Scherrer equation: $D_{hkl} = \frac{K\lambda}{\beta\sin\theta}$, where K is usually taken as 1, and β is the width of the peak, in radians.

3.3.2 X-Ray Reflectivity

XRR is an extension of optical reflectivity to the X-ray domain. In the ideal case we consider specular reflections from a surface and multilayer. That is, the angle of reflection is the same as the angle of incidence. The XRR signal is collected as both angles are varied simultaneously.

One of the simplest formulas describing theoretically expected reflectivity from ideally smooth, sharp, and structureless interfaces was derived by Augustin-Jean Fresnel in the early 19^{th} century and is known as Fresnel reflectivity. For angles of incidence above that of total reflection, the intensity of the specularly reflected beam is given by:

$$R = \left| \frac{n_1 \sin\theta_1 - n_2 \sin\theta_2}{n_1 \sin\theta_1 + n_2 \sin\theta_2} \right|^2 , \tag{3.11}$$

where $n_{1,2}$ are the refractive indices in the first and second media, and $\theta_{1,2}$ are the angles of propagation away from the *plane of the sample*. This can be extended to many interfaces, or simplified to the case of one layer, where we can consider the path difference to determine the occurrence of constructive interference, thus leading to an expression for the thickness t, as will be given below (equation 3.12).

XRR is highly sensitive to electron density changes and gradients irrespective of crystallinity [69]. Fitting XRR scan data enables us to extract information on thicknesses, interface roughness amplitudes, and densities of single and multi-layered samples. Figure 3.10 shows a simulation of an XRR scan of a 50 nm Fe layer grown on GaAs, and capped with 5 nm Au. There are three main features to be noted. Firstly, the critical angle, at (a), whose position yields the average electron density. The second feature is the spacing of the interference fringes, the Kiessig fringes. This will enable us to calculate the thickness, t, of the corresponding layer. We can accurately estimate t by using the relation:

$$t = \frac{\lambda}{2\Delta\alpha}, \tag{3.12}$$

where $\Delta\alpha$ is the fringe spacing. As we see, the fringe spacing is inversely proportional to the layer thickness. In figure 3.10 we can identify the two oscillations corresponding to (b) the thick Fe layer, and (c) the thin Au cap. Finally, the

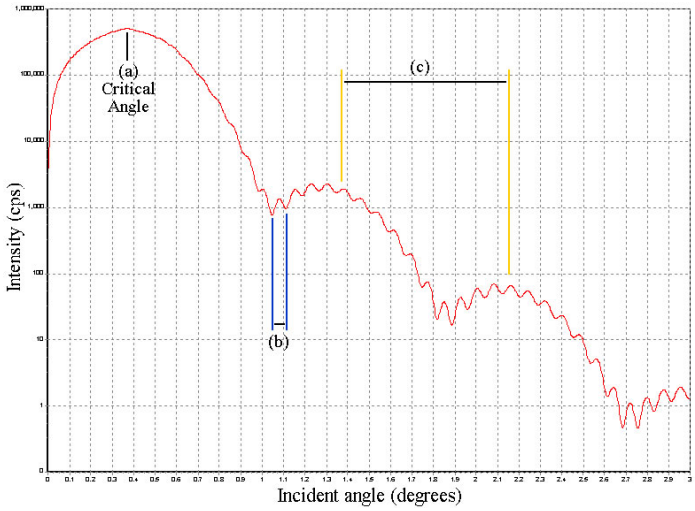

Figure 3.10: Example of calculated XRR data. In this case the sample is 5 nm Au/50 nm Fe/GaAs. The roughness amplitude for each of the interfaces and surface was set to 5 Å. (a) the critical angle; (b) Kiessig fringes from the Fe layer; and (c) Kiessig fringes from the Au cap.

roughness of each interface can also be extracted from XRR data. This can be deduced from the amplitude of oscillation of the Kiessig fringes, and also the decay of the signal. Interface roughness reduces the specularly reflected intensity; the 'missing' intensity is scattered in different directions than that of the detector, and hence the count rate decreases.

Chapter 4

Fe/GaAs and Fe/InAs Magnetic Moment

Abstract

We present magnetometry data for a range of Fe thicknesses (0.4 - 23 nm) grown on GaAs and InAs substrates in order to determine the factors governing the evolution of the magnetic moment of epitaxial Fe grown on a zinc-blende semiconductor. In this comparative study, all the samples on both substrates were grown under the same conditions. We observe a greater reduction of the Fe magnetic moment for films grown on InAs as compared to GaAs. We conclude that the growth conditions, in particular interface and interdiffusion effects, are the dominant mechanisms influencing the value of the magnetic moment for ultra-thin Fe films on GaAs and InAs.

Introduction and Outline

The pioneering of magnetic materials deposition on semiconductors in the 1980's opened new avenues of research and device possibilities [34]. Since then, ferromagnet/semiconductor (FM/SC) heterostructures such as Fe/GaAs and Fe/InAs have attracted considerable attention due to their possible application in future magneto-electronic devices. Such devices make use of the spin of the electron in addition to its charge, the token example being the spin-polarised transistor,

proposed by Datta and Das in 1990 [5]. Much of the current research on thin magnetic films has focussed on the Fe/SC system, and in particular the Fe/GaAs system [36, 70–74]. However, it has become apparent that the interface between the SC and FM layer in these spintronic devices is crucial to their potential uses. Indeed the quality of this interface, and specifically morphological and interdiffusion effects may drastically affect ultra-thin magnetic films grown on SC substrates [31].

We carried out a comparative study of the two systems Fe/GaAs(100) and the closely related Fe/InAs(100) [75, 76] to determine the evolution of the Fe magnetic moment as a function of thickness. First we will briefly discuss the preparation of the substrates and growth of the epitaxial Fe layers. Then we will present structural and magnetic characterisation data for the range of samples, using both *in situ* and *ex situ* methods. Finally we will present our conclusions on the evolution of the Fe magnetic moment on GaAs and InAs as a function of thickness, interpret the data trends and compare ours to previous work and results [77, 78].

4.1 Growth and *In situ* Characterisation

4.1.1 Substrate Preparation and Sample Growth

The GaAs substrates we used for this study were prepared with an undoped GaAs buffer-layer in a separate SC UHV MBE chamber, and As-capped before transfer into our metals deposition chamber described in chapter 3. After loading, we first degassed the As-capped substrates and sample holder at 200°C for 2 hours. Then the temperature was raised to ∼420-480°C for 20 minutes to desorb the As cap, and ensure the arsenic was pumped out of the chamber. In the final surface preparation step we increased the temperature to ∼550°C for 1 hour, to obtain a clean and ordered GaAs(100)-P(4×6) reconstructed surface.

For the InAs substrates we used commercial 'epi-ready' wafers n-doped with sulfur ($n \approx 10^{18}$ cm^{-3}). These did not have an InAs buffer layer or As-cap, so required wet-etch preparation before loading into the UHV chamber. The wet-etch procedure included an acetone ultrasonic bath, isopropanol and then deionised water rinse. We then cleaned the substrate in an oxygen plasma etch

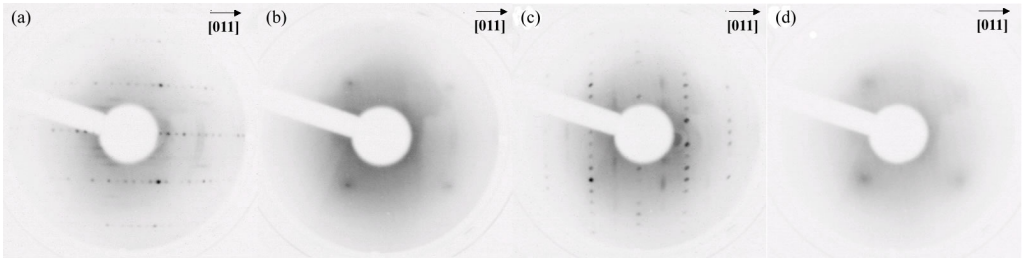

Figure 4.1: LEED patterns from: (a) GaAs substrate exhibiting the P(4×6) reconstruction; (b) 0.4 nm Fe/GaAs; (c) InAs substrate exhibiting a c(8×2) reconstruction; and (d) 1.3 nm Fe/InAs.

for 30 seconds, before dipping them in HCl:H_2O (1:4) solution for 30 seconds to etch the native oxide layer. We then rinsed the substrates in deionised water and isopropanol again, and loaded them as quickly as possible in the vacuum chamber. After loading, we also degassed the substrates and sample holder at 200°C for 2 hours, and then annealed them at ∼500°C for 1 hour, to obtain a clean and ordered InAs(100)-c(8×2) reconstructed surface.

We grew the ultra-thin (thickness ranging from 0.4 to 23 nm) Fe films epitaxially at RT in the UHV MBE system described in chapter 3, from the tip of a high-purity (99.99+%) Fe rod. The base pressure in the chamber was $\sim 3\times10^{-10}$ mbar, and the pressure during growth was kept below 3×10^{-9} mbar, with a deposition rate of ∼1 ML/minute for the Fe. After the Fe growth, we capped each sample with either Au or Cr, in order to protect the Fe layer from oxidation and degradation upon exposing it to air. The thickness of the capping layer was always above 3 nm. We usually grew a thick (∼ 10-15 nm) Au cap so that it would be very different to the Fe layer's thickness, and subsequently ease the fitting of the XRR and PNR data.

4.1.2 *In situ* Characterisation

Once the substrate was loaded and the surface was cleaned and ready for growth, we controlled its quality *in situ* using LEED and RHEED. Representative LEED patterns of the GaAs and InAs substrates are show in figure 4.1(a) and (c), respectively. Due to the relatively high annealing temperatures of the substrates and the volatility of surface As, we expect a Ga-rich surface, verified by the observed GaAs(100)-P(4×6) reconstruction. The same applies for the surface As

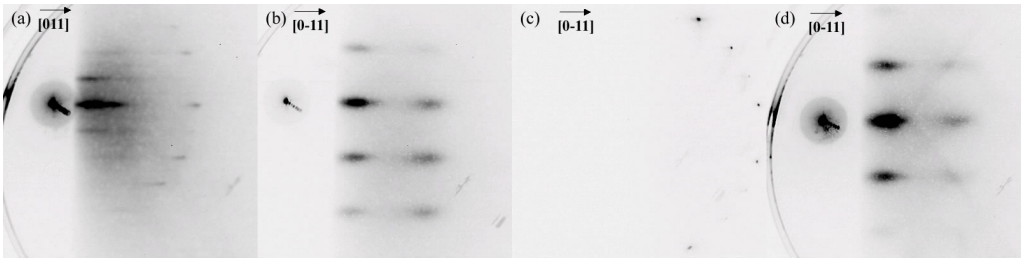

Figure 4.2: RHEED patterns from (a) GaAs(100) substrate; (b) 1.1 nm Fe/GaAs; (c) InAs(100) substrate; and (d) 5 nm Fe/InAs.

atoms of the InAs, though in addition to this we also expect In clustering at the surface [79]. Finally, the high content of S dopant atoms lead us to expect the c(8×2) surface reconstruction, which we observe in figure 4.1(c). Figures 4.1(b) and (d) show the first visible LEED patterns from the (thinnest) grown Fe film. The faint spots we observe for the growth on both substrates are already indicative of the emerging body-centred tetragonal (bct) (strained bcc) structure of the Fe films. The fact that a pattern is visible for such a low thickness and coverage of Fe (< 0.5 nm) suggests a flat Fe film surface. We note however that there was no visible LEED pattern for the thinnest (0.6 nm) Fe film on InAs(100). The larger lattice mismatch between Fe and InAs (-5.37%) disfavours early stage epitaxy at RT and therefore requires thicker films as compared to Fe/GaAs (lattice mismatch of 1.36%).

We also monitored the surface quality of the substrates prior to growth using RHEED. Whereas the LEED provides valuable information regarding surface reconstructions, the RHEED allows one to gauge the roughness of a surface, due to the low incidence angle of the incident electron beam. Representative RHEED results are shown in figure 4.2. Again, figures 4.2(a) and (c) show the patterns for the substrates prior to growth, where we observe Kikuchi arcs and even sharp spots on the second Laue ring, indicative of smooth and long-range ordered crystalline surfaces. Figures 4.2(b) and (d) show RHEED patterns from Fe/GaAs and Fe/InAs films, indicating smooth and epitaxial films, in agreement with the LEED results. As previously mentioned, after the *in situ* characterisation and growth we capped the samples with Au or Cr to protect the magnetic layers before removing them from the UHV chamber.

4.2 *Ex situ* Characterisation

4.2.1 Thickness and Roughness through XRR

We performed further structural characterisation *ex situ* by XRR. This confirmed that the Fe/SC interfaces were very sharp, and provided an additional calibration for the thickness of the Fe films, to complement the quartz microbalance readings used during the deposition (*cf.* chapter 3). Figure 4.3 presents two of these XRR scans, which are representative for all samples. Fits to the data provide values for the thickness and roughness of the heterostructures. For these fits, the Fe atomic density was kept constant at its bulk value, while the density of the capping layer was allowed to vary slightly, to account for oxidation (of the Cr) and/or the possibility of imperfect epitaxial growth. Assuming reacted interface layers [70, 76] and/or oxidised capping layers [80] did not change the fits significantly, suggesting that they cannot be distinguished from our stated errors for the Fe thickness and roughness [81], and only add unnecessary parameters to the fits.

The thickness values we obtained from the XRR scans and fits were in general agreement with the calibration from the growths of the samples. However we found that for very thin films, the number of fringes on the XRR scan (inversely proportional to film thickness) was sometimes too small to allow us to deduce an accurate value for the thickness. For the thicker films we sometimes came across slight discrepancies between the nominal thickness and the XRR fit result, which we attribute to variations of the MBE flux during the evaporation of Fe. With a slow deposition rate of $\sim$1 ML/min, a typical Fe film (*e.g.* 15 nm) would take us slightly over an hour to evaporate.

The roughness amplitude values for the Fe/SC interfaces were $\sim 0.3 \pm 0.2$ nm for Fe/GaAs, and $\sim 0.6 \pm 0.2$ nm in the case of Fe/InAs. The roughness amplitude between the magnetic layer and Au or Cr capping layer was estimated as $\sim 0.5 \pm 0.2$ nm. These values remained fairly similar for the whole range of samples. We attribute the larger roughness at the Fe/InAs interface (as compared to the Fe/GaAs case) to two main reasons. Firstly, we note that our InAs(100) were not As-capped, and therefore presented a potentially lower-quality surface to grow Fe on, despite the various etching and preparation steps detailed in section 4.1.1 above. In addition to this, the higher lattice mismatch for the case of Fe/InAs is expected to lead to more defects and strain relaxation sites, and hence greater

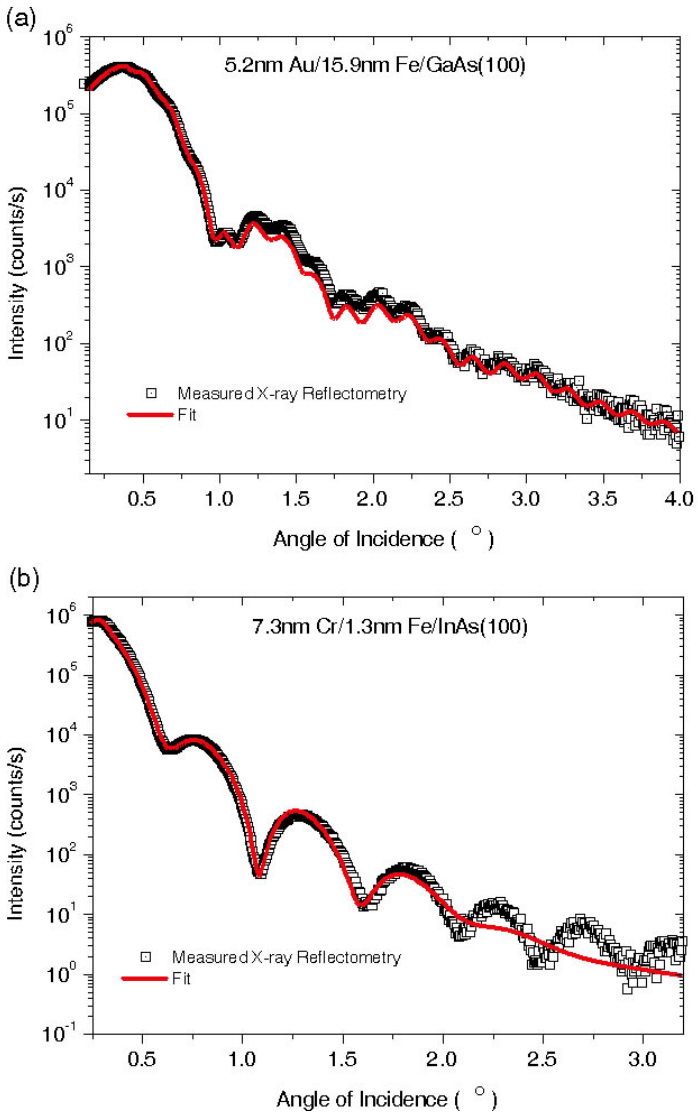

Figure 4.3: Low-angle XRR measurements and fits of (a) 5.2 nm Au/15.9 nm Fe/GaAs(100); and (b) 7.3 nm Cr/1.3 nm Fe/InAs(100). The fits assume bulk density for the Fe.

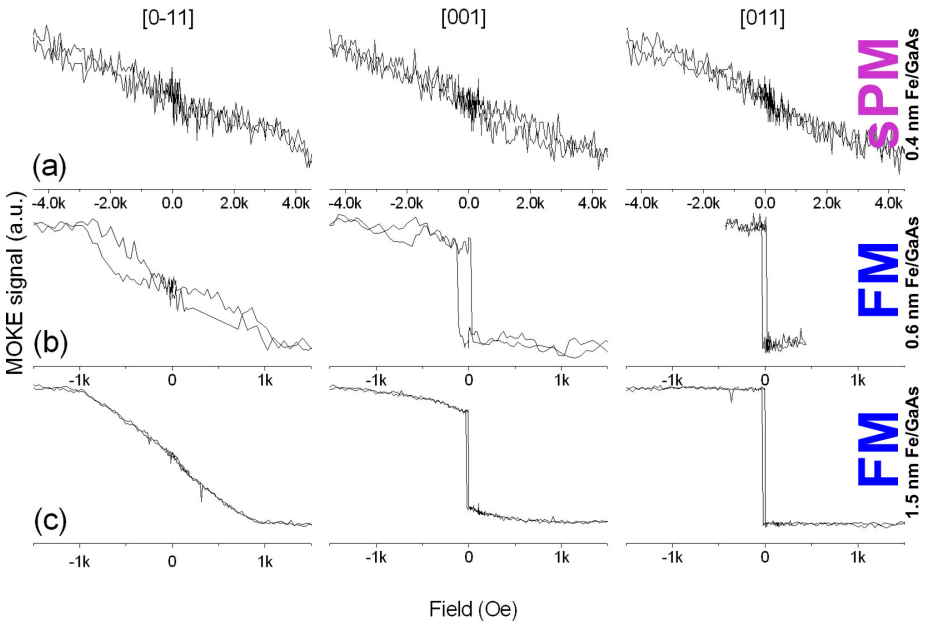

Figure 4.4: MOKE loops of (a) 0.4 nm; (b) 0.6 nm; and (c) 1.5 nm thick Fe layers on GaAs(100), with the field applied in-plane along 3 directions.

roughness at the interface.

4.2.2 Magnetic Characterisation

We conducted magnetic characterisation of the films using vector MOKE measurements, PNR and SQUID measurements at RT (SQUID also at low temperatures).

We took longitudinal MOKE measurements along three in-plane axes to determine the saturation fields, magnetic anisotropies and the magnetic state of the different heterostructures. The results for the thinnest films on GaAs and InAs are shown in figures 4.4 and 4.5, respectively. These showed that the thinnest Fe films (0.4 ± 0.2 nm) on GaAs were still in a superparamagnetic state. Similarly, three axes in-plane MOKE results for the Fe/InAs films show that films of thickness 0.6 ± 0.2 nm and below are still in a superparamagnetic state [41, 71, 75]. As we actually expect a 0.6 nm Fe film on InAs to have switched to a FM state [75], we deduce that our thinnest film must be at least 0.1 nm thinner than the nominal growth thickness.

The anisotropies for the cases of both substrates were verified to switch from

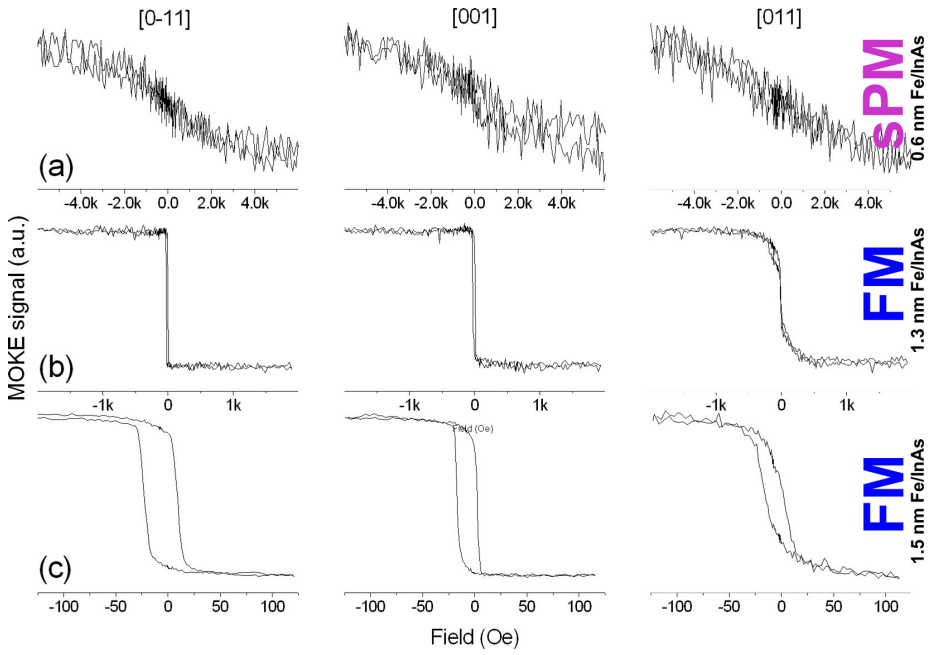

Figure 4.5: MOKE loops of (a) 0.6 nm; (b) 1.3 nm; and (c) 1.5 nm thick Fe layers on InAs(100), with the field applied in-plane along 3 directions.

uniaxial to cubic with increasing thickness. This occurs after ∼50 ML ≈7.2 nm in the case of GaAs [36, 37]. The in-plane uniaxial magnetic easy axis for Fe/GaAs is along the [011] direction, with the hard axis along the $[0\bar{1}1]$ direction. This uniaxial anisotropy can be seen emerging in figure 4.4. For Fe/InAs however the switch from uniaxial to cubic anisotropy happens earlier, at ∼12 ML ≈1.7 nm [82]. In this case, as shown in figure 4.5, the uniaxial magnetic in-plane easy axis is along the $[0\bar{1}1]$ direction, with the uniaxial hard axis along the [011] direction.

PNR allows us to simultaneously determine the magnetic moments, as well as thicknesses and interface roughnesses, which can also be determined by XRR. We also performed SQUID magnetometry measurements to estimate the magnetic moment of some of our films. Representative SQUID loops for this study are shown in figure 4.6. As the SQUID is sensitive to the total magnetisation of the sample rather than to the atomic moment, we used the XRR thickness calibration to calculate the volume of the deposited Fe for each sample, and estimate the magnetic moment per atom. We used the PNR measurements combined with the SQUID/XRR data to determine the value of the magnetic moment of the Fe films and thereby the evolution of the Fe magnetic moment with thickness at

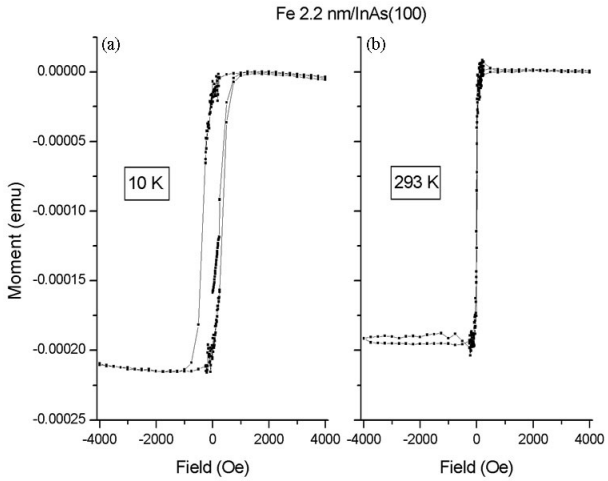

Figure 4.6: SQUID loops of a Fe/InAs(100) film, of nominal thickness 2.2 nm, taken at (a) 10 K; and (b) 293 K. XRR revealed that the Fe film was in fact 1.5 ± 0.2 nm.

RT.

4.3 Results and Discussion

4.3.1 Evolution of the Magnetic Moment

Figure 4.7 shows a compilation of our experimental results, obtained from PNR and SQUID/XRR results. The fits correspond to a power law (insets in the figure) used to approximate the evolution of the magnetic moment with thickness, which includes a bulk and a surface term. The green horizontal lines represent the bulk magnetic moment of Fe at RT. For comparison, we include the magnetic moment values estimated previously by other groups for both types of heterostructures [71–74, 76, 83–85]. It must be noted that some of these values from the literature are extrapolated to RT, or the samples were grown under slightly different conditions to ours. We conclude from our and other groups' results that the interface drastically affects the magnetic moment of ultra-thin Fe layers.

For the RT growth of Fe, we chose the Ga-rich P(4×6) reconstructed GaAs(100) and In-rich c(8×2) InAs(100) surfaces, to avoid excessive As segregation into the Fe films. It has been shown that for Fe/GaAs(100) heterostructures that Ga tends to segregate into the Fe films but remains close to the interface for thick-

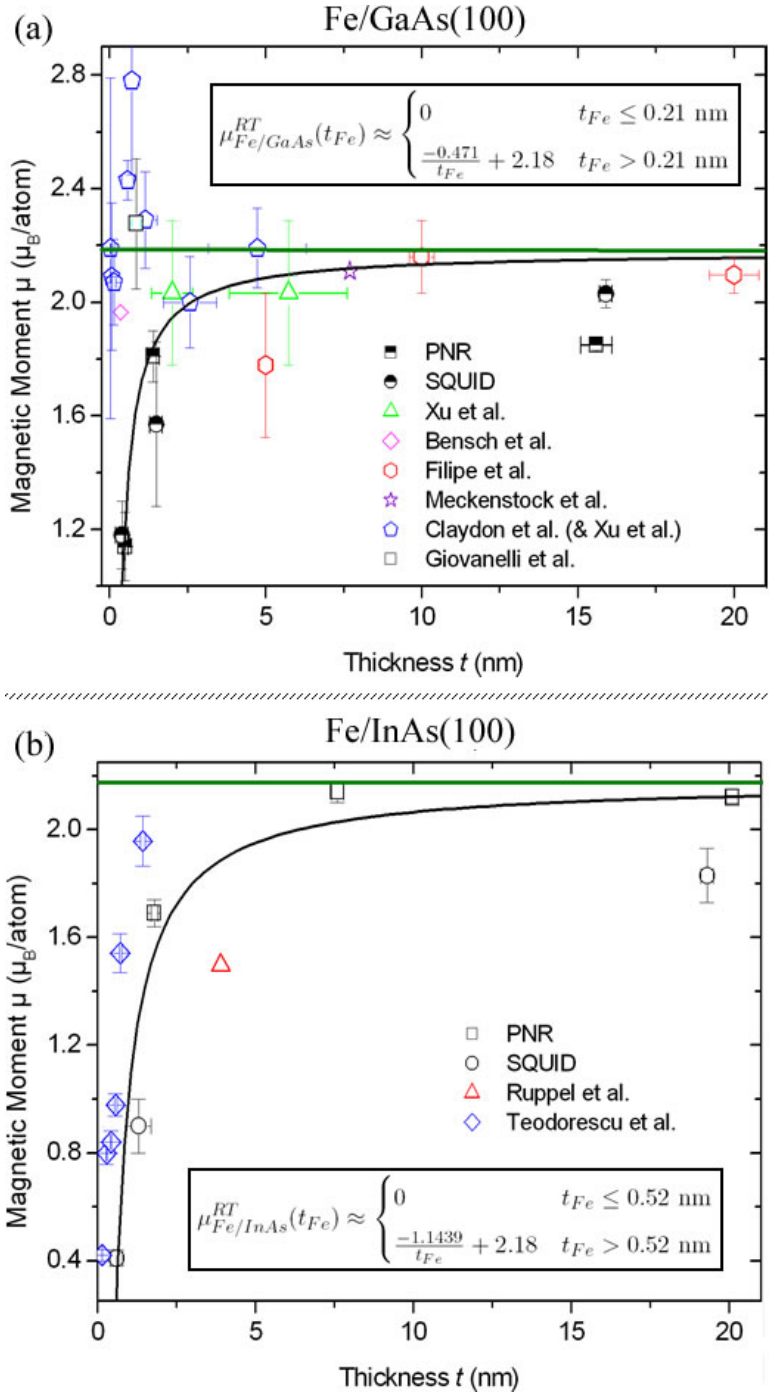

Figure 4.7: The magnetic moment μ_B/atom vs. thickness for (a) Fe/GaAs(100); and (b) Fe/InAs(100). The horizontal green lines represent the bulk magnetic moment of Fe at RT, and the fits are simulations to our data. For comparison, we also present magnetic moment values estimated by other research groups. *Insets*: the power-law fits to our data. At very low coverages, the magnetic moment value goes to zero due to magnetically inactive compound layers (see main text).

nesses above 0.4 nm, and does not float on the surface for RT grown films [70]. In contrast, indium has a low solubility in Fe and therefore a small amount of In tends to float besides the As on the Fe surface. Also, from the fainter LEED patterns of thin Fe/InAs, we deduce that the InAs(100) surfaces were rougher than the GaAs(100) surfaces, despite being equally well ordered. This transpired in the XRR results, which indicated that the average roughness for the Fe/GaAs samples was 0.1 - 0.3 ± 0.2 nm, for the whole thickness range, whereas the XRR fits yielded roughness amplitude values of 0.4 - 0.6 ± 0.2 nm for the case of Fe/InAs. These correspond to ∼2 and ∼4 ML of Fe, respectively. We believe that an epitaxial InAs buffer layer, protected by an As cap for transfer would improve the roughness of the InAs substrates. It is also possible that a post-anneal or a high temperature growth (*e.g.* 175°C [86]) may improve the crystallinity of the ultra-thin Fe layers on InAs, but this would also result in increased interdiffusion between the Fe and the substrate [87]. In fact we expect this to be the case for both GaAs and InAs, and it is not desirable for spintronic device applications.

The fit shown in figure 4.7 is a fit to our data only, and established from a constant bulk term and a thickness-dependence surface term [78]. This fit was made with two assumptions, namely that the Fe magnetic moment is zero at zero coverage; and the Fe magnetic moment reaches its bulk value[1] either when the Curie temperature, T_C, reaches 1040.2 K, or the film thickness approaches infinity. An expression for the T_C of Fe grown on GaAs(100)is given by Bensch *et al.* for $t_{Fe} > 0.358$ nm [71]:

$$T_C(t_{Fe}) \approx (\frac{t_{Fe}}{0.358\ [nm]} - 1)^{0.837} K. \tag{4.1}$$

The power law fit to our data is, in units of μ_B/atom is:

$$\mu^{RT}_{Fe/GaAs}(t_{Fe}) \approx \begin{cases} 0 & t_{Fe} \leq 0.21 \text{ nm} \\ \frac{-0.471}{t_{Fe}} + 2.18 & t_{Fe} > 0.21 \text{ nm}. \end{cases} \tag{4.2}$$

The same assumptions were made for the case of Fe/InAs, which leads to the following power-law fit:

[1] Bulk Fe magnetic moment at RT ≈ 2.18 $\mu_B/atom$.

$$\mu^{RT}_{Fe/InAs}(t_{Fe}) \approx \begin{cases} 0 & t_{Fe} \leq 0.52 \text{ nm} \\ \frac{-1.1439}{t_{Fe}} + 2.18 & t_{Fe} > 0.52 \text{ nm}, \end{cases} \tag{4.3}$$

again in units of μ_B/atom. The value of the magnetic moment is zero until a certain coverage is reached. This is calculated as being 0.21 nm ($\simeq$ 1.5 ML Fe) and 0.52 nm ($\simeq$ 3.6 ML Fe) for the cases of Fe/GaAs(100) and Fe/InAs(100), respectively. This corresponds to the formation of magnetically inactive, or 'dead' layers. Only above these thickness values does the Fe film form in a bcc structure (in fact a bct structure at first). Prior to this, the Fe merely constitutes part of an underlying intermixed layer (*e.g.* Fe_2As). We note that this thickness of 1.5 ML for the case of Fe/GaAs corresponds exactly to the thickness of the Fe_2As 'seed' crystal layer as suggested by an STM study of this system [31]. Unfortunately there is no similarly precise STM study of intermixing for the case of Fe/InAs, though there are reports of distorted Fe growth and intermixing between the FM and SC for coverages below 5 ML [86, 88].

Comparison of the two fits reveals that the Fe moment decreases faster with decreasing thickness in the case of Fe/InAs. There are several interplaying mechanisms that govern the magnitude of the total magnetic moment at a given thickness at RT. Firstly, the Curie temperature depends on the film thickness due to the size effects and is below RT for coverages below $\sim$0.5 nm [71, 75]. We also observe this in our MOKE results, which show that the thinnest films are not yet in a ferromagnetic state. Secondly, it seems that at low coverages the interface roughness can have a particularly large effect, possibly overwhelming an enhancement of the total magnetic moment at the interface due to the symmetry breaking. In addition to this, an increased Fe/SC interface surface due to roughness favours interdiffusion of the present atomic species. Interdiffusion in general leads to a decrease of the magnetic moment and in the worst case, for films grown at high temperatures, to the presence of thicker magnetically 'dead' layers or 'half-magnetisation' phases [70]. Compared to this, we expect the strain induced by the pseudo-morphic growth of the Fe films on the SC to have only a small influence on the magnetic moment due to the volume changes in the distorted bct Fe cell, as compared to bulk bcc Fe [89]. In addition, this influence is reduced as soon as the films begin to relax to their bulk lattice parameters.

Finally, the reduction of symmetry at the interface can lead to an enhancement of the total magnetic moment, as suggested by the results of Claydon *et al.* [73, 85], in particular of the orbital moment component at a coverage just above the onset of ferromagnetic order. This orbital contribution, however, is counterbalanced by the reduction of the moment due to roughness or interdiffusion, as indicated by our results.

4.4 Conclusions and Future Work

In conclusion, we have studied and characterised Fe films grown at RT by MBE on GaAs and InAs substrates in order to determine the factors governing the evolution of the magnetic moment of epitaxial Fe grown on a zinc-blende SC substrate. We observe a greater reduction of the Fe magnetic moment for films grown on InAs as compared to GaAs, and the Fe films reach a bulk-like moment (within 10% deviation) at a thickness of ∼2.2 nm and ∼5.2 nm on GaAs and InAs, respectively. We conclude that the substrate quality and preparation, growth conditions, and in particular interface and interdiffusion effects are the dominant mechanisms influencing the value of the magnetic moment for ultra-thin Fe films on GaAs and InAs.

Further work on this study could focus on two aspects that arose from our experiments and the literature. Firstly one could further investigate the effect of the capping layer on the Fe moment. The oxidation of a Cr cap [80] could affect the measured moment of an ultra-thin Fe film. Also, a possible reduction of the magnetic moment at the Fe/SC interface may be compensated by an enhancement at the Au/Fe interface [90]. Following this still, we could investigate the influence of buffer layers on the Fe/SC system, for instance by having a Fe/1 ML Au/SC sample configuration. Another aspect that would be of interest is to focus more specifically on the evolution of the moment for the thickness range near the SP/FM transition. Finally, we could naturally extend and repeat the study for other FM metals commonly used in device applications.

Acknowledgements

With thanks to H. E. Beere of the Semiconductor Physics Group for the growth of the GaAs buffer layers, G. Wastlbauer and A. Ionescu for help with the Fe layer growths and *in situ* characterisation. Thanks to R. M. Dalgliesh and S. Langridge of the Rutherford Appleton Laboratory, A. Ionescu and C. A. F. Vaz for help during the PNR measurements and fits. Thanks to F. van Belle for the SQUID measurements, and the XRR was collected with M. E. Vickers of the Department of Materials Science and Metallurgy, and A. Ionescu.

Chapter 5

Spin Injection and Electro-Luminescence

Abstract

Spin injection is performed from an Fe contact into a semiconductor AlGaAs/GaAs QW structure. We present electrical, magnetic and spin injection characterisation of such spin-LEDs. We report a ∼1% spin injection efficiency at RT, increasing to ∼4% at 77 K, as detected by optical polarisation in the oblique Hanle geometry.

Introduction and Outline

In recent years the emerging field of spin electronics, or spintronics, has captured the attention of many research groups around the world. Spintronic devices use the intrinsic electron property of spin, rather than charge. The token example of such a device is the spin field effect transistor, proposed by Datta and Das in 1990 [5]. The basic concept of such a device sees spin-polarised electrons injected from a source electrode, and detected electrically or optically at a drain electrode. The device therefore relies on spin injection, spin manipulation (or control), and spin detection.

In this chapter, we will examine the injection and optical detection of spin-polarised electrons into a SC. We will start by presenting the theory and background of the experiment, including previous relevant work. We will then de-

tail the sample preparation and set-up we used for this experiment, and finally present results, discuss the outcomes of our current work and possibilities for further investigation.

5.1 Theory and Background

5.1.1 Principle and Theoretical Introduction

Optical Spin Orientation

Optical spin orientation provides a basis for quantifying spin injection in a powerful approach to research studies of spin transport. Optical spin orientation was first demonstrated in 1968 by Lampel, where the spin polarisation was detected using nuclear magnetic resonance [91]. Subsequently, the optical detection of spin oriented electrons in semiconductors was carried out by several groups, with Pierce and Meier developing an approach for optically detecting spin-oriented photo-electrons emitted from GaAs [92].

Figure 5.1 shows a schematic band structure for GaAs, and the allowed transitions for circularly polarised light in GaAs. In GaAs, the valence band maximum and the conduction band minimum are at the Γ-point, the centre of the Brillouin zone ($\mathbf{k} = 0$), with an energy gap $E_g = 1.42$ eV at RT. As a direct band gap semiconductor, the only transition induced by a photon of energy $h\nu$ occurs at Γ. The valence band (p-symmetry) splits into four-fold degenerate $P_{3/2}$ states at Γ_8, and two-fold degenerate $P_{1/2}$ states, which lie at and energy Δ=0.34 eV below $P_{3/2}$, at Γ_7. The $P_{3/2}$ band consists of two-fold degenerate bands, which are the heavy hole and light hole sub-bands. The conduction band (s-symmetry) is two-fold degenerate $S_{1/2}$ at Γ_6. This is shown in figure 5.1(a). When circularly polarised light with an energy of $h\nu = E_g$ illuminates GaAs, electrons are excited from the $P_{3/2}$ to the $S_{1/2}$ bands. According to the selection rule ($\Delta m_j = \pm 1$), two transitions for each photon helicity (left and right circular polarisation) are possible. However the relative transition probabilities for light ($m_j = \pm 1/2$) and heavy ($m_j = \pm 3/2$) holes are different, resulting in a net spin polarisation of excited electrons in the GaAs [92, 93]. This is illustrated in figure 5.1(b), where we see that for instance if electrons are excited only from the valence band maximum by circularly polarised light, three times more carriers are excited from

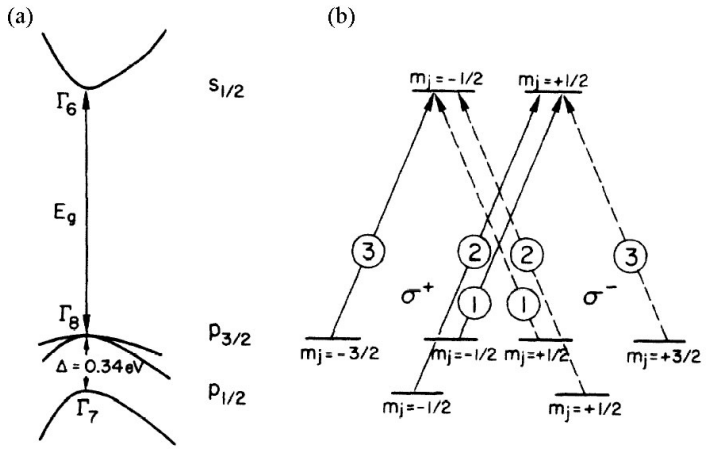

Figure 5.1: (from [92]). (a) *E-k* diagram of the energy bands near $k = 0$ for GaAs, which shows the energy gap ($E_g = 1.42$ eV) for both heavy and light holes, and the spin-orbit splitting Δ of the valence bands. (b) The allowed transitions for σ^+ ($\Delta m_j = 1$) and σ^- ($\Delta m_j = -1$) circularly polarised light, shown by solid and dashed lines, respectively. The circled numbers represent the relative transition probabilities.

$m_j = \pm 3/2$ than from $m_j = \pm 1/2$. So in theory, a maximum polarisation of 50% for the resulting carriers[1] can be expected for σ^+ or σ^- excitation.

In the case of the electro-luminescence, these selection rules obviously still apply, and we are only reversing the experimental method. Now, injected polarised carriers will emit, upon recombination with holes, different proportions of left and right circularly polarised light. This polarisation of the light then provides information on the polarisation of the injected carriers at their recombination point.

Emission from GaAs Bulk and Quantum Wells

Under uniaxial deformation, the four-fold degeneracy at the top of the valence band is lifted, and the coupling between angular momentum and quasi-momentum[2] for states near the top of the band is destroyed. The direction of the quantisation is now not determined by the quasi-momentum, but by the axis of deformation, so that states are defined by the projection of the angular momentum on this

[1] $\frac{3-1}{3+1} = \frac{2}{4} = 50\%$

[2] The energy spectrum and coefficients of the light and heavy hole bands are found by solving the equation: $\hat{H}\chi_M = \varepsilon_\mu \chi_M$, where χ_M is a column of coefficients χ_{M_μ}, and $\hat{H}$ is the Hamiltonian of Luttinger. By solving this using a spherical approximation, it is found that the coefficients $\chi_{M_\mu}(\mathbf{k})$ depend only on the direction of $\mathbf{k}$ [94].

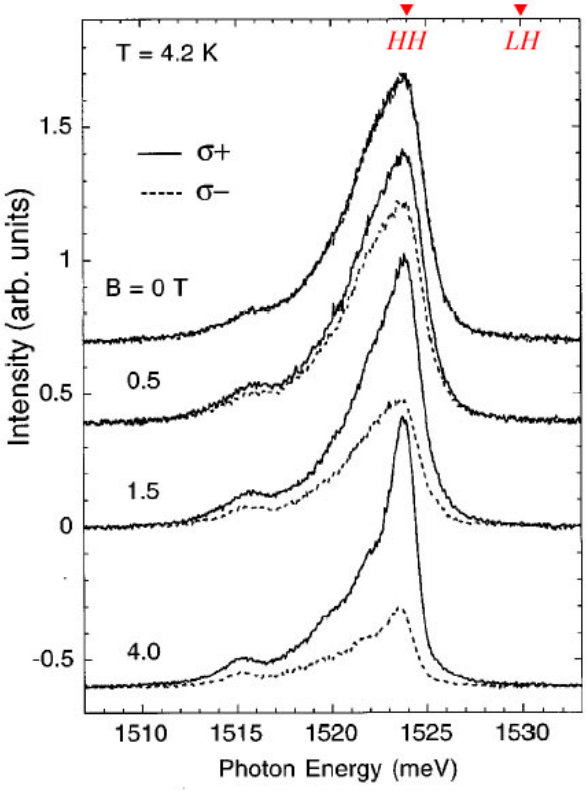

Figure 5.2: (after [95]) Electro-luminescence spectra from a Fe/GaAs QW spin-LED for selected values of applied magnetic field at 4.2 K, but also showing the relative positions of the heavy- and light-hole features obtained from photo-reflectivity measurements ($B = 0$). The feature near 1.515 eV is attributed to recombination in the bulk GaAs.

axis. The influence of this deformation is essential for states with energies less than the deformational splitting[3], ΔE, at $k = 0$, and changes the selection rules for optical transitions.

As stated, the heavy-hole (hh) and light-hole (lh) band splitting is typically several meV even in shallow quantum wells, which is much larger than the thermal energy at low temperature, so that the lh states are at higher energy and are not occupied. In this case, only the hh participate in the radiative recombination process. This is illustrated in figure 5.2, where Jonker *et al.* measured luminescence from a 15 nm GaAs quantum well (QW), and we see that they only detected emission from photons with energy corresponding to the c-hh recombination [95].

We note $P_{EL} = (I_+ - I_-)/(I_+ + I_-)$ where $I_{+,-}$ are the intensities of the two

[3]for GaAs $\Delta E \simeq 10$ meV/kBar [94].

helicities of circular polarised light, which links the luminescence and the net circular polarisation of the detected light. We can also establish $P_{EL} = \alpha \mathbf{S} \cdot \hat{\mathbf{z}}$, where $\hat{\mathbf{z}}$ is the direction of observation, and $\alpha = 2$ for luminescence from a QW, but $\alpha = 1$ for bulk systems, due to the deformation or strain in the crystal.

Electron Spin Dynamics

The general spin state, or average electron spin, $\mathbf{S}$, is related to the experimentally accessible magnetic moment via the relation

$$\boldsymbol{\mu} = g\mu_B \mathbf{S}, \tag{5.1}$$

where g is the Landé g-factor, and μ_B is the Bohr magneton. The orientation and magnitude of $\mathbf{S}$ will in turn depend on the applied magnetic field $\mathbf{B}_{app}$ and the electron spin lifetime:

$$T_s = (\tau_s^{-1} + \tau^{-1})^{-1}, \tag{5.2}$$

where τ_s^{-1} is the rate of electron-spin relaxation (scattering), and τ^{-1} is the rate of electron-hole recombination. We define the electron spin immediately after injection into the QW as $\mathbf{S}_0$. Spin relaxation that occurs before the electrons recombine with holes reduces its initial value S_0 to its steady-state value S. In addition, the spins will precess about $\mathbf{B}_{app}$ whenever $\mathbf{B}_{app} \times \mathbf{S} \neq \mathbf{0}$. The angle through which the spin precesses is determined by the product ΩT_s, of the Larmor angular frequency and the electron spin lifetime, with $\Omega = g^* \mu_B \mathbf{B}_{app}/\hbar$, where g^* is the effective electron g factor. Typically one will have $\Omega \sim 10^{10}$ Hz at 5 kG and $T_s \sim 200$ ps, giving $\Omega T_s \lesssim 2\pi$. Combining these processes of injection, precession, relaxation, and recombination, we can define a rate equation that describes the dynamics of the electron spin in the QW [96]:

$$\frac{d\mathbf{S}}{dt} = \boldsymbol{\Omega} \times \mathbf{S} - \frac{\mathbf{S}}{\tau_s} - \frac{\mathbf{S} - \mathbf{S}_0}{\tau}. \tag{5.3}$$

The electro-luminescence is a steady-state measurement, thus we can set $d\mathbf{S}/dt = 0$, and solve equation 5.3 for $\mathbf{S}$. For convenience we define the characteristic magnetic field $B_{1/2} = \hbar/(g^* \mu_B T_s)$ at which $\Omega_{B_{1/2}} T_s = 1$. We can then write the steady-state solution:

$$\mathbf{S} = \eta \frac{B_{1/2}^2 \mathbf{S}_0 + (\mathbf{S}_0 \cdot \mathbf{B}_{app})\mathbf{B}_{app} + B_{1/2}(\mathbf{B}_{app} \times \mathbf{S}_0)}{B_{1/2}^2 + B_{app}^2}, \tag{5.4}$$

where $\eta = 1/(1+\tau/\tau_s)$ [94, 96]. Equation 5.4 is the general equation for electron spin dynamics in GaAs under steady-state conditions. For the experiment we will discuss here, the sample lies in the $x-y$ plane, and the z component S_z of $\mathbf{S}$ is detected by the circular polarisation of the luminescence P_{EL}, and $\mathbf{S}_0$ is injected from a ferromagnetic metallic contact.

5.1.2 Theories of Spin Injection

Diffusion and Tunnelling, and the Conductivity Mismatch

Schmidt *et al.* suggested that there may be a fundamental obstacle to achieving efficient spin transmission across a FM/SC interface via a diffusive process, due to the conductivity mismatch between the FM and SC [97] (see also chapter 6, section 6.3). A simple picture of this is advanced by Bland *et al.* [93], where they show that as the conductivity of the FM is much larger than that of the SC, only a small fraction of the electrons in the FM can enter into the SC, and the number of electrons entering is almost the same for both spin channels. A more thorough description of this system involving the spin-dependent electro-chemical potentials of the materials confirms this simplified picture.

The solution to this problem was advanced by Rashba [98] and Smith *et al.* [99], and it involved moving away from diffusive transport, and toward a tunnelling regime. A tunnelling interface or barrier can cause spin-filtering by providing single-step coherent tunnelling of the carriers. This is achieved by designing a sufficiently high and narrow barrier, which will allow the spins to tunnel into the conduction band of the SC.

Injection through a Schottky Barrier

A Schottky barrier at a FM/SC interface can produce such a tunnelling interface. The electrical spin injection at a Schottky contact has been extensively studied, and was reviewed by Albrecht and Smith in 2002 [100]. Here, they address issues such as the band bending and depletion regions in real structures. One aspect of this study addresses the doping profile of the Schottky barrier, which

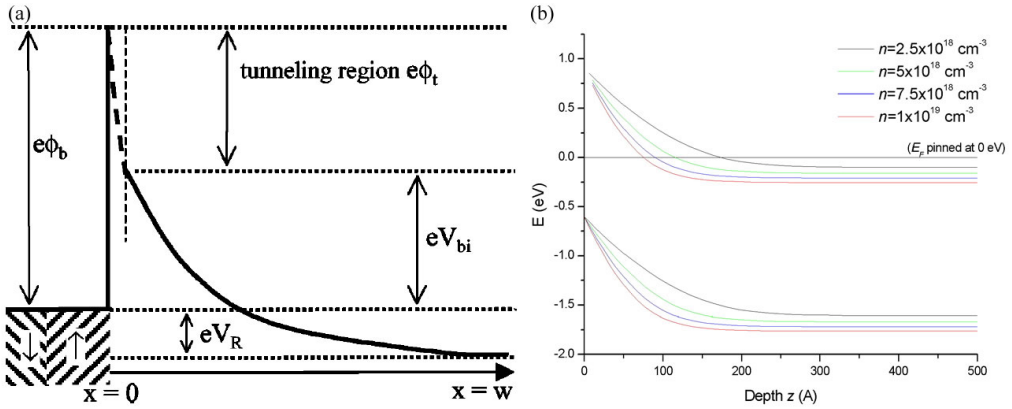

Figure 5.3: (a) (from [100]) Energy diagram of a Schottky contact including the possibility of a narrow, highly-doped tunnelling region near the interface (dashed portion of the conduction band profile). (b) Modelled band energy diagrams for various n-type doping of GaAs, simulated at 77 K.

spin-selective injection is very sensitive to. They conclude that a heavily-doped region near the interface can be used to reduce the effective energy barrier and form a spin-selective tunnel barrier to a FM contact, while not increasing the depletion width in the SC. The doping profile should be chosen so that the potential drop in the depletion region is as small as possible, and they also note that the tunnelling region must have a significant interface resistance.

A suggested Schottky barrier junction is shown in figure 5.3(a), where the total barrier $e\phi_b$ is divided into two parts which are a tunnelling region with barrier height $e\phi_t$, and an effective Schottky built-in barrier height eV_{bi}. The potential drop in the depletion region consists of this effective Schottky barrier plus the applied reverse bias eV_R. We used the SC heterostructure band modelling program HETMOD to model Schottky barriers with different doping concentrations, for the simple case of 500 Å of n-type GaAs. These are shown in figure 5.3(b), where we see that as the doping concentration is increased, the Schottky barrier becomes sharper, which would be more favourable to tunnelling. Finally, a note on the depletion layer width, which is defined by:

$$W = \sqrt{\frac{2\varepsilon_S}{qN_D}(V_{bi} - V)}, \tag{5.5}$$

where ε_S is the static dielectric constant, N_D is the doping density, and V_{bi} is the built-in potential across the depletion layer. For GaAs, $\varepsilon_S = 13.1 \times \varepsilon_0$,

and $V_{bi} \approx 1.3$ eV. At zero bias, W is estimated to be in the range 3.4 to 34 nm ($N_D = 10^{19}$ cm^{-3} and $N_D = 10^{17}$ cm^{-3}, respectively). When W is large, the electron tunnelling process is reduced due to the wide tunnel barrier, while tunnelling does not occur for very small W because of tunnel barrier breakdown [93].

Injection into Non-Magnetic Metals

Injection of spins into non-magnetic metals (NM) has also been addressed theoretically. The approach for such a study is typically to define a contact resistance, r_C, and the two characteristic resistances, r_N and r_F, each given by the ratio of the spin diffusion length and the effective bulk conductivity in the corresponding region. Then, as above, all quantities such as the electro-chemical potential and current density must be continuous across the junction. The theoretical derivation of this FM/NM contact was performed and reviewed by Žutić *et al.* [101]. This derivation can be readily extended to the FM/NM/FM case of a spin-valve structure, again by setting continuity of parameters across both interfaces.

5.1.3 Spin Depolarisation in Semiconductors

Spin relaxation and spin dephasing are processes of great importance to spintronics. The fact that non-equilibrium spins in metals and semiconductors live relatively long, allowing for spin-encoded information to travel macroscopic distances, is what makes spintronics a viable option for technology. Here we will discuss three major physical phenomenon which lead to the loss of spin polarisation in carriers. These are the Elliot-Yafet (EY), D'yakonov-Perel' (DP), and Bir-Aronov-Pikus (BAP) mechanisms [101, 102].

The Elliot-Yafet Mechanism

In 1954, Elliot was the first to point out that carrier spins can relax via ordinary momentum scattering if the lattice ions induce spin-orbit coupling in the electron wave-function [103]. In the presence of the coupling, the exact Bloch state is not a spin eigenstate but a superposition of them. This induces a finite probability for spin flip when the spatial part of the electron wave-function experiences a transition through scattering, even if the involved interaction is spin-independent.

Momentum scattering is typically caused by impurities (at low T) and phonons (at high T). A systematic calculation of the phonon-induced spin lifetime from the known band and phonon structure was developed by Yafet in reference [104] in 1963. We will not reproduce this here, but note that the EY mechanism depends greatly on the doping concentration in the semiconductor and the temperature.

The D'yakonov-Perel' Mechanism

In GaAs, the inversion symmetry is broken by the presence of two atoms in the Bravais lattice. Without inversion symmetry the momentum states of the spin-up and spin-down electrons are not degenerate, *i.e.* $E_{\mathbf{k}\uparrow} \neq E_{\mathbf{k}\downarrow}$. Spin splittings induced by this inversion asymmetry can be described by introducing a $\mathbf{k}$-dependent magnetic field, around which electron spins precess with Larmor frequency, $\Omega(\mathbf{k})$. Since the magnitude and the direction of $\mathbf{k}$ changes in an uncontrolled way due to electron scattering with impurities and excitations, the DP mechanism contributes to spin relaxation [102, 105]. In this mechanism, the spins experience dephasing between momentum collisions as they experience precession about the $\mathbf{k}$-dependent field.

In two-dimensional SC systems, *e.g.* quantum wells and heterostructures, the structural inversion asymmetry also contributes to the DP mechanism. This leads to different spin relaxation times depending on the relative orientations of the spins with respect to the crystal planes. In (100) quantum wells, the life-time of a spin parallel to the plane is twice that of the spin perpendicular to the plane [101].

The Bir-Aronov-Pikus Mechanism

The electron spin-flip transition is also made possible by electron-hole scattering via exchange and annihilation interactions. This was first shown by Bir *et al.* [106], and is especially strong in p-type SC due to high hole concentrations.

Dominant Mechanisms in Various Semiconductors

All three of these mechanisms co-exist in the III-V SC we are interested in. However, in general one will dominate over the others, depending on internal parameters such as the doping and impurity concentrations, and also external

parameters such as temperature. Song and Kim looked at the three mechanisms and presented the dominant one as a function of temperature and doping concentration for both n-and p-type GaAs, InAs, GaSb, and InSb [102]. They find that the EY mechanism is dominant in all four cases only at very low temperatures ($T < 8$ K) in n-type SC, and the DP mechanism dominates above that temperature, for all studied doping concentrations. The DP mechanism is also dominant in p-type SC, but in general only at low ($N_A \lesssim 10^{16}$ cm^{-3}) acceptor concentration, above which the BAP mechanism becomes dominant.

Hyperfine Interaction

The hyperfine interaction is the magnetic interaction between the magnetic moments of the electrons and nuclei. This provides an important mechanism for ensemble spin dephasing, and single-spin decoherence of localised electrons. This weak interaction is a means to couple electron and nuclear spins in a controlled way [96, 101].

5.1.4 Spin Injection Predictions at the Fe/SC Interfaces

There have been a number of theoretical studies of the Fe/GaAs and Fe/InAs interfaces due to their relevance to spintronic devices. Simulations have tried to predict the exact spin polarisation at the interfaces. Although these models usually ignore the slight lattice mismatch between the Fe and substrate, there are attempts to include the effects of intermixing using models such as the one shown in figure 5.4. Here, Vutukuri *et al.* [107] investigate the possibility of coherent spin injection across an Fe/GaAs interface by using band-structure codes in a Fe/GaAs/Fe trilayer. These simulations still use an idealised system, but they find that Bloch states only of certain symmetries are able to progress through such an interface, thus enabling spin-filtering. Indeed, the Δ_1 symmetry of bulk Fe majority-spin state near the Fermi energy E_F matches that of bulk GaAs band-edge states, while the symmetry of the Fe minority-spin does not. This is schematically shown in figure 5.5, and results in preferential transmission of majority-spin electrons from the Fe injector. Furthermore, as was also pointed out by Vutukuri *et al.* [107], the Δ_1 symmetry state (Fe majority-spin band) decays relatively slowly in GaAs, while the states of $\Delta_{2'}$ and Δ_5 symmetry

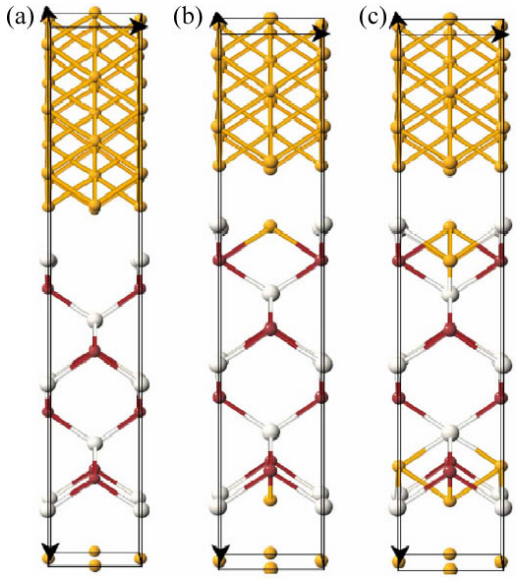

Figure 5.4: (from [107]) Modelled interfaces for Fe/GaAs/Fe structure. (a) Atomically abrupt interface; (b) partially intermixed, with one Fe atom filling a GaAs vacancy site; and (c) fully intermixed, with 2 Fe atoms filling GaAs vacancy sites.

(Fe minority-spin bands) decay much more quickly, suppressing transmission of minority-spin carriers.

Wunnicke *et al.* [109] agree that the process of spin injection is to a large extent determined by the symmetries of the band structure. They also consider spin injection through an Fe/GaAs interface, in the hot 'ballistic' regime and in the diffusive regime. Polarisations of nearly 100% are predicted, again due to the absence of minority Δ_1 states in the Fe. Further simulations of lower-energy electrons, performed with and without a (Schottky) tunnel barrier, also yield such huge polarisation predictions. The authors admit that interface disorder in a real system would reduce this spin polarisation, though unfortunately they do not quantify this effect.

Very similar reasoning is applied by Zweirzycki *et al.* for the case of Fe/InAs [108]. The Fe/InAs interface forms an ohmic contact, where no Schottky barrier is formed. In this study, we note that the authors did take into consideration the lattice mismatch present, and assumed distorted bct unit cells for the Fe at the interface. Again, enormous polarisation values (>85%) are predicted in the ballistic regime due to the band structure of the Fe majority and minor-

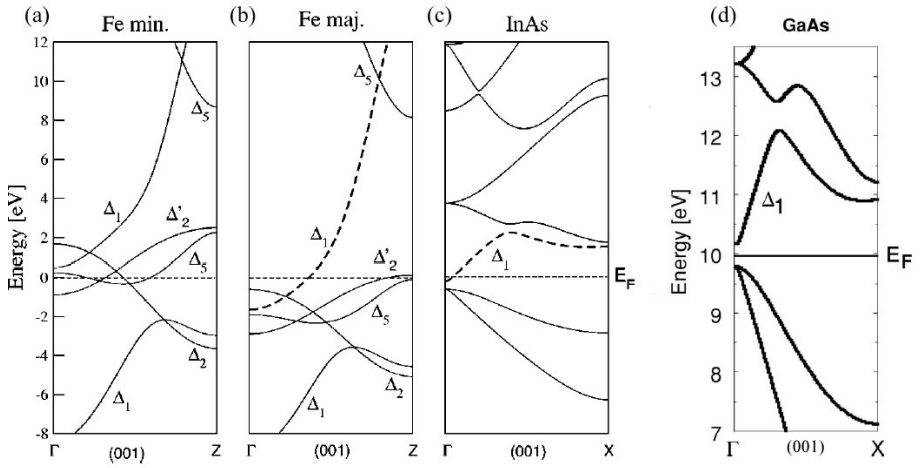

Figure 5.5: (from [108, 109]) Energy band structures of (a) Fe minority-spin states; (b) Fe majority-spin states; (c) InAs states; and (d) GaAs states.

ity spin states. Moving towards a more realistic case, Zweirzycki *et al.* [108] introduced symmetry breaking at the interface, and calculated the interface resistance for transport of the majority and minority spin states. They find that a large difference in these resistance values is entirely suppressed as soon as they simulate ∼10% atomic substitution at the interface. This disorder opens new transport channels which are symmetry-forbidden for specular interfaces. Thus they conclude that strongly spin-selective transport should be possible through an Fe/InAs interface, providing that the sample is grown epitaxially and with a very high degree of perfection.

Moving away from simulations, several studies have looked at real Fe/SC interfaces, and the formation of interfacial mixing layers. Lépine *et al.* report on deliberately-formed Fe_3GaAs at the Fe/GaAs interface [110]. In an attempt to form thermally stable compounds on GaAs, these were made by deposition of fairly thick (20-80 nm) Fe layers on GaAs, and post-annealing the film at 480-500°C for 10 minutes. XRD and transmission electron microscopy (TEM) reveal the presence of Fe_3GaAs, but also Fe_2As crystals at the interface, with some overall crystallinity though not perfect epitaxy. We note that the estimated magnetic moment per Fe atom for films of this compound was equal to $1.2 \pm 0.1\mu_B/atom_{Fe}$.

Zega *et al.* treated Fe films grown on AlGaAs with a low temperature anneal

at 200°C for 10 minutes [111]. High-resolution-TEM images reveal an interfacial region, which is reduced from 0.7 nm before the anneal to 0.5 nm afterwards. Following on from the above, the authors also discuss the possible presence of an Fe_3GaAs layer at the interface, but conclude that this compound does not occur in this case and establish that a partially intermixed interface is a more accurate representation of the sample. By applying models of abrupt, partially intermixed and fully intermixed interfaces, Zega *et al.* [111] find that while there is no significant change in the Δ_1 decay rate for the first two cases, the fully intermixed model points to a significantly faster Δ_1 decay, suggesting lower spin polarisation of the injected carriers.

For the case of Fe/InAs, Yoh *et al.* published TEM images of the interface for such samples grown at 23°C and 175°C [87]. Although these show that the sample grown at 175°C suffers from more interface reaction, this effect is not quantified. The authors also report highly-efficient spin injection from the Fe contact directly into *p*-InAs, though they do not report on the effect of the intermixing layer in the sample grown at high-temperature.

These simulations and research support our concern over the intermixing of the atomic species present for Fe/SC systems. We note in particular reports of the presence of Fe_3GaAs compounds without annealing treatments [112], as well as the mention of the formation of anti-ferromagnetic [113] Fe_2As crystals. Once more we found that much less research has been published for the case of Fe/InAs as compared to the well-documented Fe/GaAs case. Using substrate preparation methods and MBE growth of epitaxial Fe, we hope to obtain an interface that might be as close as possible to the ideal, abrupt case, but it is clear that intermixing in a real sample is unavoidable.

5.1.5 Previous Work

The electro-luminescence (EL) spin-injection measurement is one that is widespread, and currently performed by many research groups around the world. Here we will present a brief overview of work by other groups in recent years, after a quick look at the various geometries used in the EL experiment.

Note about Experimental Geometries

There are several different geometries that provide information about the spin polarisation of a polarised current. These are all shown schematically in figure 5.6.

The Faraday Geometry In the Faraday geometry, the magnetic field is applied parallel to the direction of light propagation (figure 5.6(a)). S_z is simply the component of $\mathbf{S}_0$ along $\hat{\mathbf{z}}$, scaled by η, which characterises longitudinal spin relaxation prior to recombination (equation 5.4). In the Faraday geometry, we note that B_{app} must be large enough to rotate $\mathbf{S}_0$ out of plane, typically $\mathrm{B}_{app} \geq 2$ T for Fe.

The Oblique Hanle Geometry In the oblique Hanle geometry, shown in figure 5.6(b), the field is applied at a small angle out of plane, but with its in-plane projection along the magnetic easy axis of the sample. In this geometry, $\mathbf{S}$ precesses about $\mathbf{B}_{app}$ after injection. For higher values of applied field, the electron spin makes several rotations before radiative recombination takes place and the average electron spin is aligned along the applied oblique magnetic field, so $\mathbf{S}$ will have a non-zero perpendicular component S_z, which results in circular polarisation of the applied light [114].

The Voigt Geometry and the Hard-Axis Geometry In the Voigt geometry, spin polarised carriers are optically pumped in the SC by circularly polarised light at energy near the SC band edge. This geometry is sketched in figure 5.6(c), with the magnetic field applied entirely in-plane, and the optically injected spin is entirely along the direction of laser propagation.

In the Hard-axis geometry, the field is again applied entirely in plane, but along the magnetic hard axis direction. Now, $\mathbf{S}_0$ rotates in-plane as a function of B_{app}, and $\mathbf{S}$ precesses about $\mathbf{B}_{app}$ after injection.

Injection from a Semi-Magnetic SC

Spin injection from a magnetic SC is one approach that has attracted considerable experimental interest. In such a system, the obstacle of the conductivity

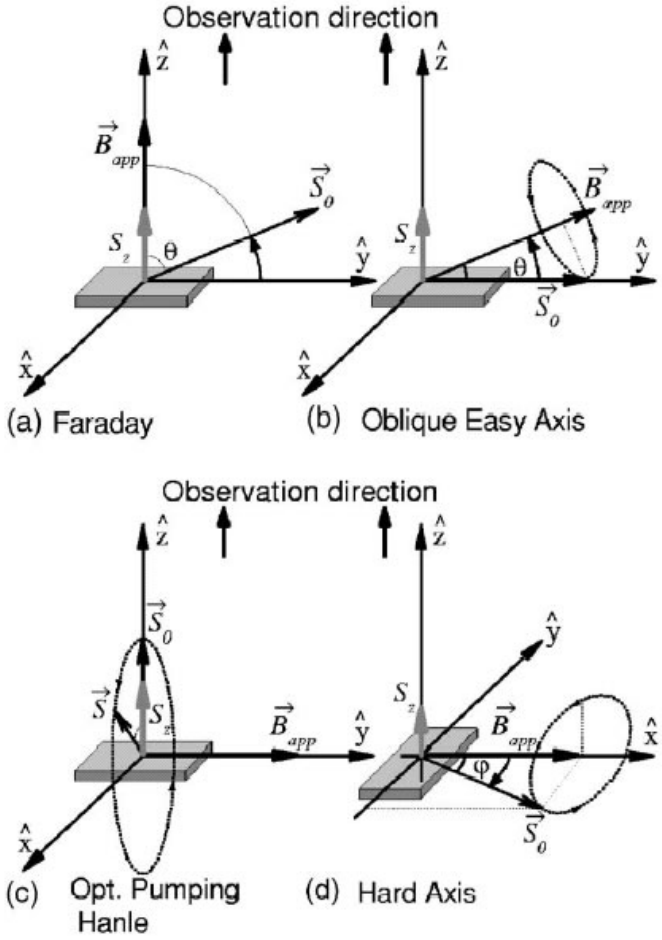

Figure 5.6: (from [96]) Different measurement geometries for the EL experiment. (a) Faraday geometry; (b) Oblique (Hanle) easy axis geometry; (c) Optical pumping Voigt geometry; and (d) Hard axis geometry. The injected spin direction is along $\mathbf{S}_0$, the applied field is along $\mathbf{B}_{app}$, and the detected component of steady-state spin is S_z. In all the cases, the observation direction is in the z direction.

mismatch is lifted entirely, as the contact is from one SC to another. However, diluted- or semi-magnetic SC only exhibit FM behaviour at low temperatures. There are continuous efforts to increase the Curie temperature of such materials, but at present they remain FM only well below RT, which is a severe disadvantage in terms of integration into devices.

Fielderling *et al.* [115] report on the injection of a spin-polarised current from a $Be_xMn_yZn_{1-x-y}Se$ spin aligner, and into a AlGaAs/GaAs QW light emitting diode (LED) structure. $Be_xMn_yZn_{1-x-y}Se$ is very well suited for spin injection into GaAs, as its lattice parameter can be matched to that of GaAs (by varying Mn concentration), thus allowing for high-quality interfaces. In this system, electrons can be injected at low energy, close to the bottom of the GaAs conduction band. Fielderling *et al.* [115] report optical polarisation of nearly 43% at low temperature (<5 K).

Jonker *et al.* [95] report a similar value of 50% optical polarisation, upon injection from a $Zn_{1-x}Mn_xSe$ layer, again on a AlGaAs/GaAs LED structure. Their measured EL spectra at 4.2 K, also obtained in the Faraday geometry, are shown in figure 5.2 in section 5.1.1 above, where we see a clear difference in the intensity of left and right circularly polarised light as the applied field is increased.

Injection from a Ferromagnetic Metallic Contact

Zhu *et al.* [116] deposited a 20 nm Fe layer on a p-i-n LED structure comprising two $In_{0.2}Ga_{0.8}As$ QWs buried in GaAs. They measure the polarisation of light in the Faraday geometry, and report values of ∼2% optical polarisation at 25 K once the applied magnetic field is large enough to align the spins entirely out of plane. Zhu *et al.* [116] note that the detected optical polarisation due to spin injection is super-imposed on the Zeeman splitting-induced spin alignment in the GaAs.

Hanbicki *et al.* [117] also report the on presence of Zeeman splitting in data obtained in the Faraday geometry at 4.5 K. Again, they used a p-i-n LED, but here with a GaAs QW buried in AlGaAs barriers. The field dependence of their results is shown in figure 5.7, where we see that the sign of P_{circ} changes as the Fe magnetisation is reversed. We note that the contribution of the Zeeman splitting

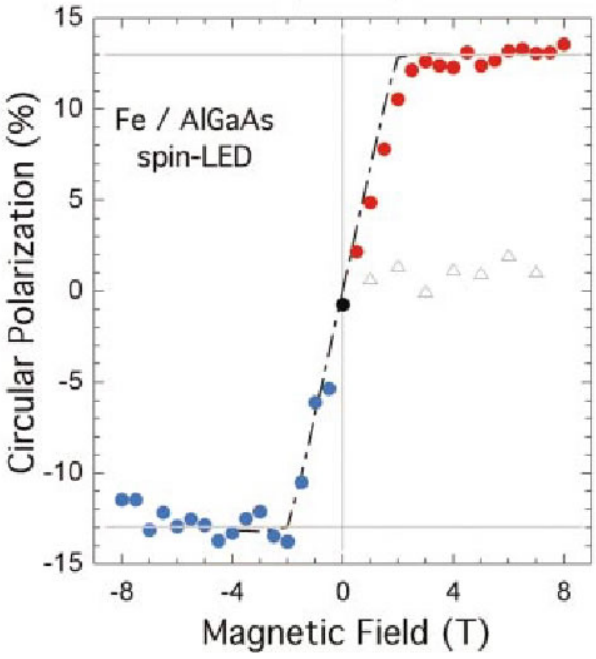

Figure 5.7: (from [117]) Field dependence of P_{circ} (circles) and the out-of-plane component of the Fe film magnetisation (dashed line), all obtained at $T = 4.5$ K. The open triangles show the measured contribution due to Faraday rotation in the Fe film.

has been subtracted in this data, and hence they report 13% optical polarisation from spin injection.

Injection through a Tunnelling Barrier

In addition to the Schottky barrier formed at a Fe/n-GaAs interface, several groups have inserted artificial oxide barriers, AlO_x and MgO, in attempts to increase spin injection efficiency.

Motsnyi *et al.* [114, 118] studied spin injection from a CoFe layer through a thin AlO_x barrier (post-oxidation of a sputter-deposited Al layer) into an AlGaAs/GaAs LED structure, in the oblique Hanle geometry. They also performed a photo-excitation measurement with linearly polarised light in order to separate the influence of the magnetic circular dichroism[4] (MCD) contribution to their signal. Motsnyi *et al.* [114, 118] report an optical polarisation value of 2.3% at 80 K.

Parkin *et al.* [119–121] investigated spin injection into a SC through an MgO barrier grown by sputter deposition. These studies were all done with CoFe injectors grown on AlGaAs/GaAs LED structures, but with a thin ($\sim$3 nm) MgO tunnel barrier inserted between the FM and SC. They perform their measurements in the Faraday geometry at a range of temperatures, and report optical polarisation of 57% and 47% at 100 K and 290 K, respectively [119]. Noting that the detected polarisation strongly depends on the spin and electron-hole lifetimes in the QW, they establish the temperature dependence of these lifetimes, and their influence on the optical polarisation. This leads to the conclusion that the actual spin injection efficiency from the CoFe contact through the tunnel barrier and into the SC only exhibits a very small temperature dependence, from $\sim$10 K to RT [120]. Finally, Wang *et al.* [121] increase the spin injection efficiency through an MgO barrier by post-annealing treatment. Fully grown samples, including the tunnel barrier and FM injector, were annealed for 1 hour at temperature steps of 300°C, 340°C, and 400°C. Such thermal treatment is likely to improve the MgO interfaces, as well as the quality of the CoFe injector. After the annealing treatment, the optical polarisation was seen to increase from 43% to 55% at 100 K.

[4]The difference in the transmission of the left and right circularly polarised light through a FM layer.

5.2 Experimental Methods

5.2.1 Growth and Processing

Semiconductor LED Design and Growth

Efficient light emission from the semiconductor part of the sample is obviously crucial to the basic success of the EL experiment. Considering this, spin injection efficiency, and spin lifetimes as discussed above, several guidelines emerge for the design of an efficient spin-LED.

All the spin-LEDs are p-i-n structures including an intrinsic QW buried in between a p- and n-doped layers on either side of it. As we want injected carriers to tunnel through a Schottky contact formed at the interface, the n-doped side will always be at the surface. The p bulk underlayers and substrate provide the holes necessary for the carrier recombination. The density profile of the n layer is an important factor in the sample design. Indeed, as we have seen above, this will determine the width and sharpness of the Schottky barrier, hence greatly influencing tunnelling properties, and also the width of the depletion layer. The depletion layer width needs to be considered when deciding on the over-layer thickness, and position of the QW.

The QW is formed by choosing SCs with slightly different band gaps. For example, a GaAs QW will be created in between AlGaAs regions, and an InGaAs QW can be buried in GaAs. The QW design and placement will be paramount in determining carrier capture efficiency. In general, we find that the design of an ideal spin-LED is a matter of trade-offs. For instance, having a higher Al-content in the AlGaAs barriers will increase the well depth, and thus carrier capture, but the added Al will contribute to spin depolarisation through impurities as discussed above.

The spin-LEDs were grown by MBE on commercial 'epi-ready' p-GaAs(100) wafers. The following describes the typical procedure for the growth of a GaAs QW buried in AlGaAs barriers. After degassing the substrate and holder, we grew a thick (500 nm) p-type buffer layer of GaAs on the substrate to provide a clean, ordered surface. Growth of p-AlGaAs followed, but prior to QW growth, we grew 15 nm i-AlGaAs in order to avoid dopant contamination into the i-GaAs QW. This i-AlGaAs layer was repeated after QW growth, before growing the

Layer Material	Etchant	Concentration
Au	Au etch (KI)	1:10 (in H_2O)
Fe	HNO_3:HCl:H_2O	1:25:400
GaAs, AlGaAs	H_2SO_4:H_2O_2:H_2O	1:8:80

Table 5.1: Etchants for spin-LED processing.

n-AlGaAs overlayer. The dopants used were Be and Si, for *p*- and *n*-doping, respectively. Finally, the sample was cooled down (from 660°C during the SC evaporations) and capped with As to avoid oxidation and contamination prior to being removed from the UHV chamber into air.

Ferromagnetic Injector Deposition

We cut the SC substrate into 10 mm × 10 mm squares, and transferred them into our UHV metals chamber. The growth of the injector (*e.g.* Fe) and Au cap was performed in the UHV chamber system described in chapter 3. This followed the same procedure as for the Fe/GaAs samples, which is detailed in chapter 4.

Sample Processing

The spin-LED structures and Fe films required processing into diodes to which electrical contacts could be made. This required chemical wet-etching of the film into pillars, and the evaporation of contact pads.

We performed the processing in a clean-room environment, where a multi-level mask was used to etch mesas into the films. The cycle of spinning resist, hardening it, exposing through a mask layer, and evaporating the contact was repeated for each mask layer. The mask set used is shown in figure 5.8. The etchants and their concentrations used for each layer are summarised in table 5.1.

To create the back contact, we etched both metallic layers away, and the semiconductor layers past the QW into the *p*-doped region. Then we evaporated an InZn alloy, and annealed it to 180°C for 10 minutes in order to decrease the resistance of the ohmic contact. In some cases we used a AuBe back contact, but the InZn was preferred due to the toxicity of BeO. For the top contacts, we first evaporated 20 nm of Ti and then 50-100 nm Au on the Au cap of the sample.

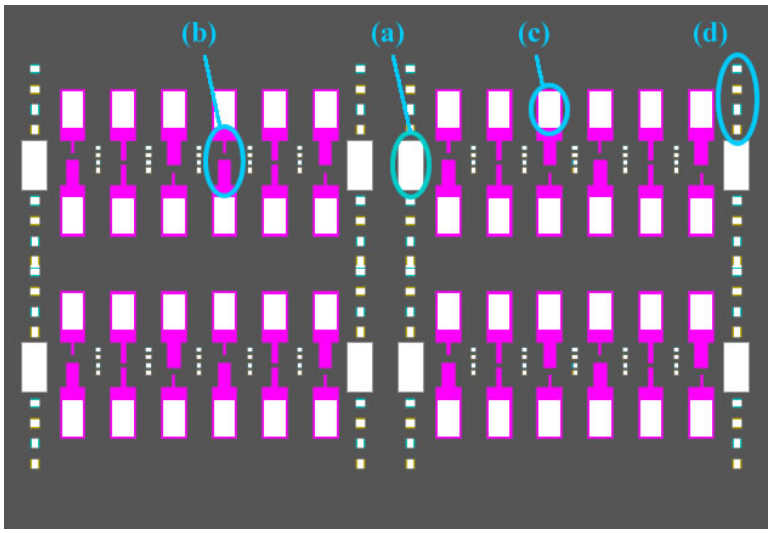

Figure 5.8: Mask set for spin-LEDs. The three layers correspond to (a) InZn back-contacts; (b) light-emitting regions (10, 20, and 30 μ m wide); and (c) Au/Ti top contacts. (d) are alignment marks for each layer of the mask set.

The Ti is necessary for the Au contact pad to stick to the sample, and we capped it with Au as the electrical contact would be through a Au wire, and to avoid oxidation.

The arrays of spin-LEDs were then separated in groups of 12 devices, which were set into a chip holder package with silver epoxy. Each device top contact was wire-bonded to a separate channel, as were the pairs of back contacts which were common to all 12 devices.

5.2.2 Optical Set-Up

We then loaded the chip package into an Oxford Instruments MicrostatHe^{TM} cryostat with optical access, and connected the device to the electrical feed-throughs. The sample and cold finger were thermally insulated by a vacuum of $\sim 10^{-4}$ mbar. We mounted the cryostat so that the sample would sit in between the pole pieces of a Lakeshore^{TM} EM7 electro-magnet, alongside a Hall probe. We were able to rotate the cryostat in the applied field, in order to vary the aforementioned Hanle angle.

A collector lens gathered the emitted light, which we focussed onto a Meadowlark Optics^{TM} variable retardation waveplate (VRW). The beam then passed

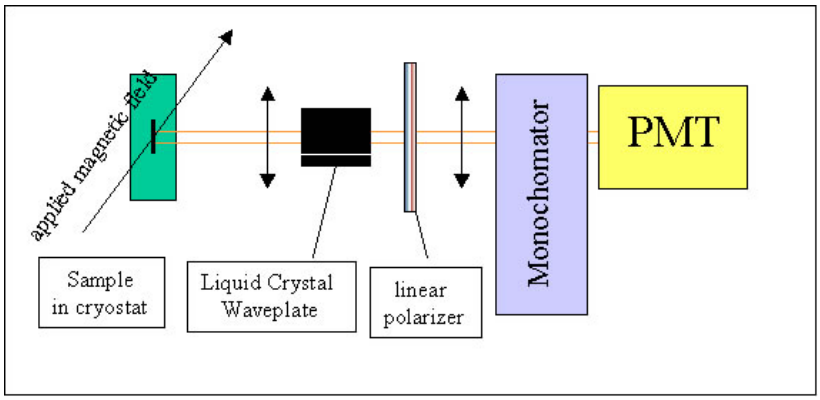

Figure 5.9: Schematic of the EL set-up. Light emitted by the spin-LED is collected, then passes through a variable waveplate, linear polariser, and is detected at a given energy (wavelength) by a photo-multiplier tube.

through a linear polariser, and we used two mirrors to bounce the light down to the level of the detector. We detected the light intensity at a given wavelength using an Oriel Instruments^{TM} monochromator, and a Hamamatsu Photonics^{TM} cooled photo-multiplier tube unit. The background counts we could hope for with this detection system were of the order of $\lesssim 10$ photon counts per second (cps). We controlled each of the components and collected our data using National Instruments' Labview^{TM} interface program. A schematic of the set-up we used for this experiment is shown in figure 5.9.

The VRW is a liquid crystal device of which the retardation can be continuously varied from 0λ to λ through a small applied voltage, for an optical range of 650 - 950 nm. We can set and store two voltage (retardation) outputs on the VWR controller which can then be alternated, again through the Labview interface. Using calibration curves and artificially-created circularly polarised light, we set these two outputs to $1/4\lambda$ and $3/4\lambda$ retardation, with the fast axis of the waveplate being at 45° from vertical. Therefore, circularly polarised light passing through the VRW will be changed to linearly polarised light, with the polarisation plane either vertical or horizontal, depending on the chirality of the incident light. By setting a vertical linear polariser at the output of the VRW, we therefore selectively pass one chirality, and block the other.

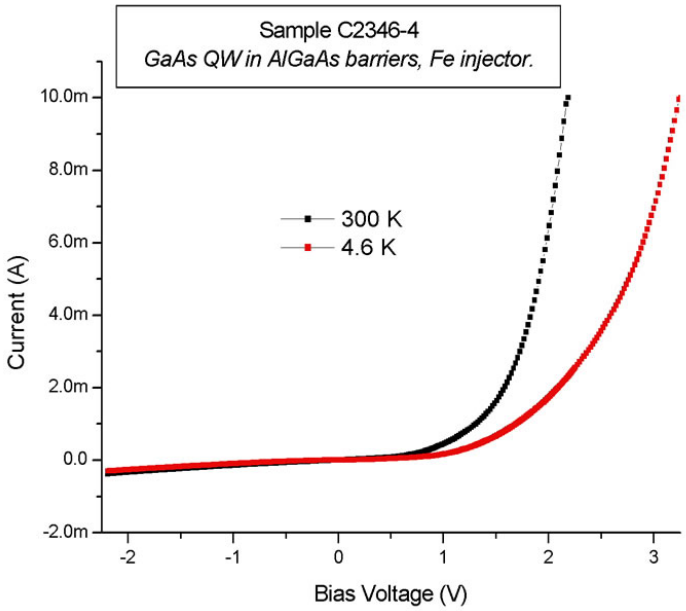

Figure 5.10: Room Temperature and Low temperature current-voltage characteristics of a spin-LED QW structure.

5.3 Results and Discussion

5.3.1 Electrical Characterisation and Light Emission

The first characterisation we performed on each LED was a current-voltage measurement. This enabled us to verify the diode-like behaviour of each device. Indeed, we often found that one or several of the devices on each chip was not suitable for further measurements, due to short- or open-circuit characteristics. The occurrence of such devices is unavoidable, perhaps caused by defects or pinholes in the films, which also influence the processing.

I-V curves measured for a film are shown in figure 5.10, for temperatures of 4.6 and 300 K. This sample had not been patterned at the time of the measurement, but only contacted with a Au pad and AuBe back contact. There are several phenomena governing the current through the Schottky barrier and LED. Thermionic emission at a Schottky metal-SC interface assumes that electrons with an energy larger than that of the top of the barrier will cross it, provided they move towards the barrier [122]. The thermionic emission current density scales with the square of the temperature. In addition to this, as the

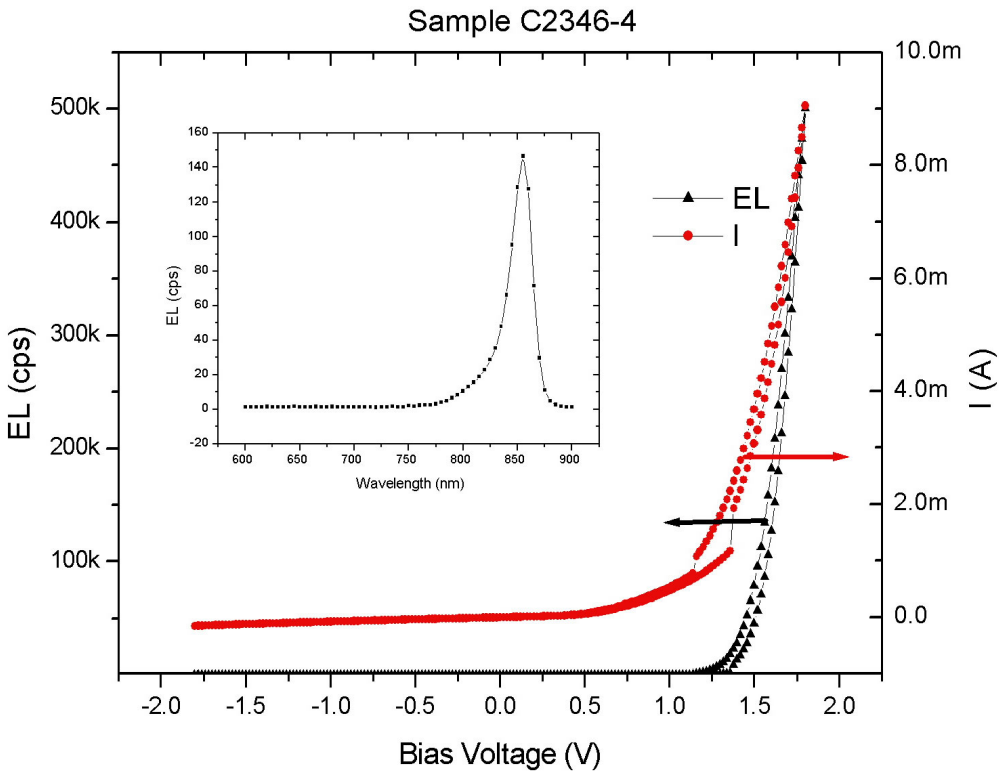

Figure 5.11: Luminescence and current as a function of applied bias voltage, taken at RT, and $\lambda = 856$ nm. *Inset:* Spectrum of emission as a function of wavelength.

sample is cooled, the band gap in the semiconductor (in this case in the GaAs QW) increases, and hence the current is reduced at a given bias. Furthermore, we expect a slight increase in the Schottky barrier height as the temperature decreases. The result of this is the shift toward higher voltages of the I-V curves, as seen in the graph. We also note that this particular device displayed good Schottky-like behaviour, with very little reverse bias (leakage) current.

The amount of emitted light depends on the number of carriers present and recombining, and therefore on the current. This is displayed in figure 5.11, where we measured the current and light emission at a specific wavelength as a function of the applied bias voltage. As we see, the emitted light follows the current through the device very closely. Indeed a plot of the luminescence as a function of the current (not shown) reveals a linear dependence above a 'switch-on' current value.

The inset of figure 5.11 shows a spectrum of emission for this device. It should

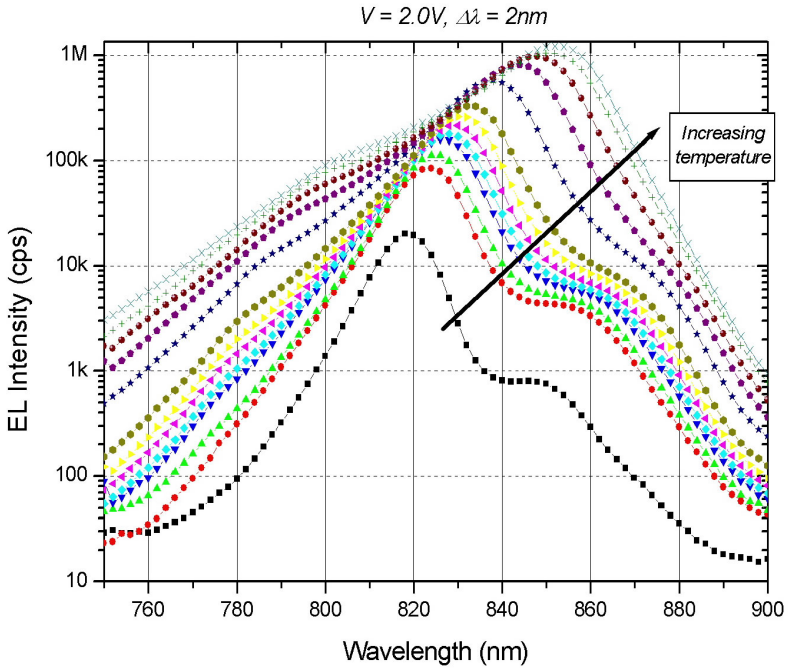

Figure 5.12: Evolution of the EL as a function of temperature, taken in *constant voltage* mode, $V = 2.0$ V. The first curve (black squares) is taken at 79 K, and the final one (crosses) at RT. Note the wavelength is a focus on the area of interest, and the vertical scale is logarithmic. The wavelength step $\Delta\lambda$ is 2 nm.

be noted that this is plotted against the detected wavelength, and not the energy of emission. This was a RT measurement, and the peak of emission corresponds to recombination in the QW. As we see, the QW in this device provides very good capture of the electrons, as we see no emission from the bulk GaAs or AlGaAs barriers at RT for this sample. The slight asymmetry of the emission spectrum is due to slightly higher energy carriers also being able to recombine and emit from the well, whereas the cut-off for the low energy carriers (high λ) is sharper.

5.3.2 Luminescence Temperature Dependence

We have already mentioned the shift in band gap, and hence current, EL intensity, and wavelength upon varying the temperature of a spin-LED. This is displayed in figure 5.12, where we have measured the emission spectrum as a function of temperature, at constant voltage. This sample was the same as that of the

previous data shown (C2346 emitter with an Fe injector), but we processed it down to square mesas, and the data shown is from a 240 μm square pillar[5].

The first thing we notice about this graph is the change in intensity. Running the measurement at 2.0 V, the current largely influenced by the change in temperature, and this in turn affects the light intensity. If we consider the curves shown in figure 5.10, the current passing through the device drops from ∼6.5 mA to ∼1.75 mA as the temperature is decreased[6]. Again, as illustrated in figure 5.11, this dramatically affects light emission, and indeed we note an 80× increase in the peak of emission as we warm the sample to RT, in constant voltage mode.

The second feature related to the temperature change is the shift in wavelength (energy) of the emission. Once more, this is due to the bang gap E_G of the GaAs increasing with temperature. Indeed we have:

$$E_G = 1.519 - 5.405 \times 10^{-4} \times \frac{T^2}{(T + 204)} eV, \tag{5.6}$$

where T is the temperature in K ($0 < T < 1000$) [123]. Therefore, as we see in figure 5.12, the emission shifts to a lower wavelength with decreasing temperature.

The final feature in this figure is the appearance of the additional peak, at lower energies, only visible for temperatures below ∼200 K. This peak corresponds to emission from the bulk GaAs. As the temperature rises to RT, this peak shifts to higher wavelengths (1.42 eV ≅ 874 nm), becomes a 'shoulder' in the QW peak, and eventually is completely absorbed by the main peak.

5.3.3 Magnetic Properties

The magnetic behaviour of each FM injector film was characterised using MOKE magnetometry. This would allow us to quickly verify the quality and epitaxy of the film, which usually displayed the expected uniaxial anisotropy of Fe/GaAs in the thin-film regime. However, it was not obvious what effect the patterning would have on the magnetisation dynamics. Indeed, this would introduce shape anisotropies, and probably pinning sites at edges and corners.

In order to measure the effect of the pattering, we used a Neoark^{TM} imaging

[5]The mask used for this processing was not the one shown in figure 5.8, but simply one of square mesas of different sizes.

[6]We note that the temperature in figure 5.10 was taken down to 4.6 K, but only to 79 K for the case of figure 5.12.

Kerr microscope. This is based upon the same principle as MOKE magnetometry (chapter 3), whereby the rotation of the incident light upon reflection provides information about the magnetisation of the surface. In the case of the microscope, a CCD camera captures the changes of intensity over an area of the sample at each stage during an external field sweep.

Images from a patterned sample are shown in figure 5.13. The first image (a) is the negative saturation state, where a large field is applied in the negative direction, and the last one (h) is the positive saturation state. Images (b)-(g) show the magnetisation reversal steps in between these two saturation cases. The contrast and various regions visible in these images are indicative of different surface magnetisation states.

Even for a very small field applied in the positive direction ((b) 0.90 Oe), we see the appearance of a reverse domain, at the corner of the emitter and contact regions. As the field increases at images (c) and (d), this domain expands along the edge, and a second reverse domain appears also along the edge. At point (e) we see that the whole emitter region has switched magnetisation, but not yet the entire contact pad. This happens at (f) and (g), but is a two-step process. Indeed, the circled region in image (f) shows a boundary between two differently aligned domains, as we see through the contrast difference in the image. This corresponds to a 90° domain in the contact pad. The MOKE magnetometry on this un-patterned sample showed two-step switching (inset in figure 5.13). This indicates the brief formation of a perpendicular domain during the magnetisation switching.

The Kerr microscope and MOKE data provide indications of the magnetisation dynamics in the patterned LEDs. We see that the switching in the emitter region is dominated by the shape anisotropy, as edges and angles provide nucleation sites for domain walls. However, in the contact pad, which is 100 $\mu m \times$ 200 μm, the film's own anisotropy still dominates the switching.

5.3.4 Optical Polarisation

Optical polarisation data is shown in figure 5.14. This is taken at room temperature, from sample ♯*C2543-M79*, which is an InGaAs QW in GaAs barriers, with a 5 nm Fe injector. A particularity about this specific sample is that it was *in*

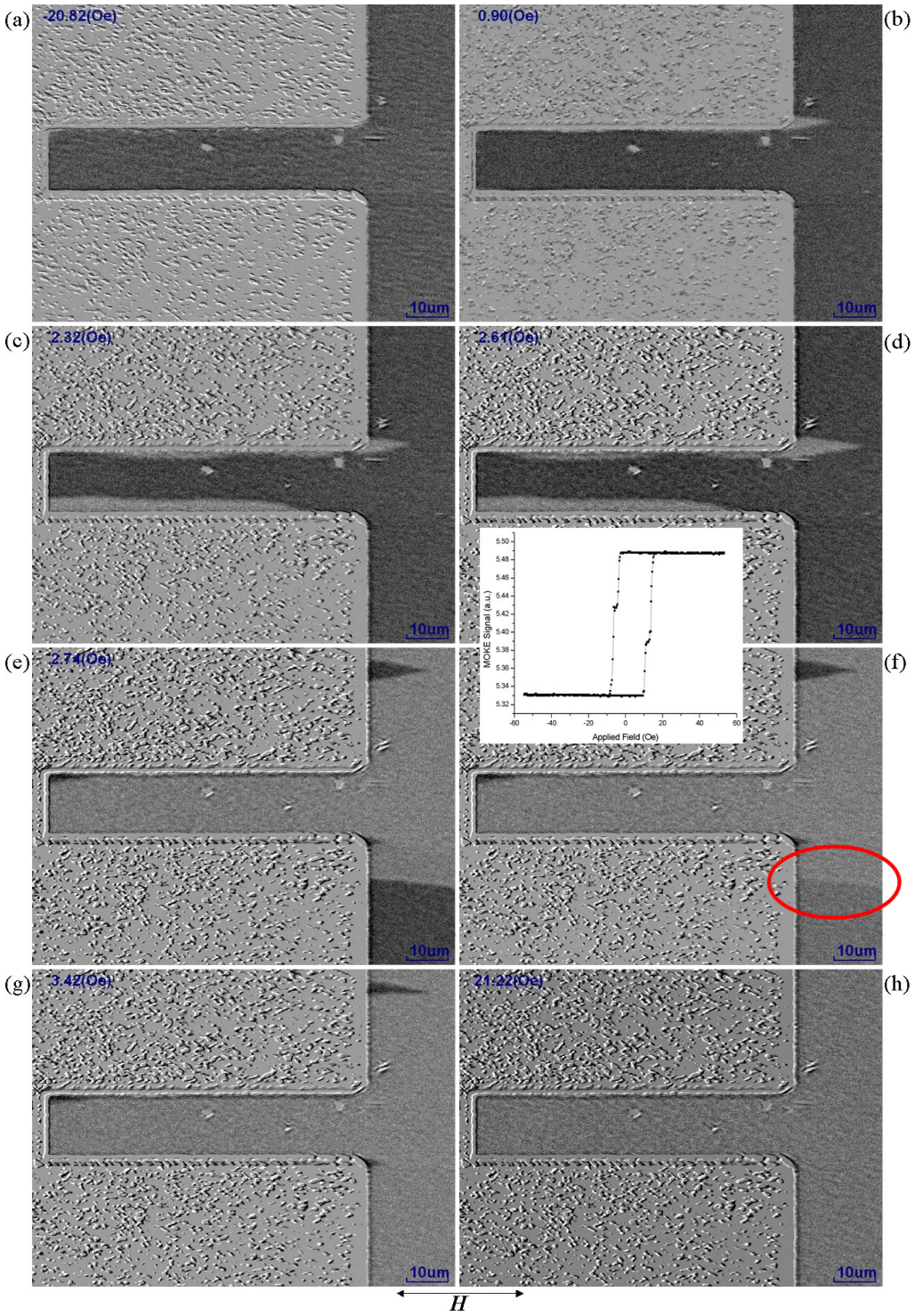

Figure 5.13: Magnetic switching in a patterned spin-LED. The applied field values are (a) -20.82 Oe; (b) 0.90 Oe; (c) 2.32 Oe; (d) 2.61 Oe; (e) 2.74 Oe; (f) 3.04 Oe; (g) 3.42 Oe; and (h) 21.22 Oe. *Inset:* MOKE loop for the un-patterned film.

situ transferred (in UHV) directly from the SC growth chamber to the metals growth chamber, without an As-cap.

The optical polarisation as a function of applied field shown here can be fitted by re-writing equation 5.4 for the S_z component, and for the case of electrical injection, where we have [118]:

$$S_z = S_{0Y} \cdot \frac{T_s}{\tau} \cdot \frac{(B/B_{1/2})^2 \cdot \cos\varphi \cdot \sin\varphi}{1 + (B/B_{1/2})^2}, \tag{5.7}$$

where T_s, τ and $B_{1/2}$ are as defined previously, and φ is the Hanle angle of the applied field. The fit to the data using this equation is also shown in figure 5.14. From this fit, we are able to extract the value of $B_{1/2}$, and hence T_S ($B_{1/2}^{-1} = g^*\mu_B T_S/\hbar$). In this case, we have $T_S = 75$ ps. Using known values of τ for this system [13], we can then determine the injected polarisation at the interface, which we established as $\Pi \approx 1\%$, at RT.

We also collected field-dependent optical polarisation data on an identical wafer which had been As-capped and *ex situ* transferred to our UHV evaporation chamber. As previously, the As-cap was then desorbed in UHV in preparation for the Fe growth. Optical polarisation values obtained at RT for this sample were identical within errors to the ones for the above ♯*C2543-M79*, thus indicating that *ex situ* transferral of As-capped spin-LED substrates provides a suitable way of transporting substrates, and is not detrimental to the SC surface or device interfaces.

Upon cooling the sample, we expect the injected polarisation to increase. The first reason for this is that recombination paths from *e.g.* C donor impurities in the QW will be reduced. As we cool the SC we also reduce the contribution of lattice phonons to the emission of light. Thus we expect a signal of emission further dominated by the recombination of interest in the QW. In addition to this the effect of scattering mechanisms as discussed above decreases with temperature. In our QW the DP mechanism dominates spin scattering. In this regime, the spin relaxation time is inversely proportional to the momentum relaxation time, and to the cube of the temperature [102].

We cooled the above (*in situ* transferred) sample to 77 K, and repeated the measurement of the optical polarisation as a function of field, shown in figure 5.15. We observed an increase of the optical polarisation, which reached ∼0.4%

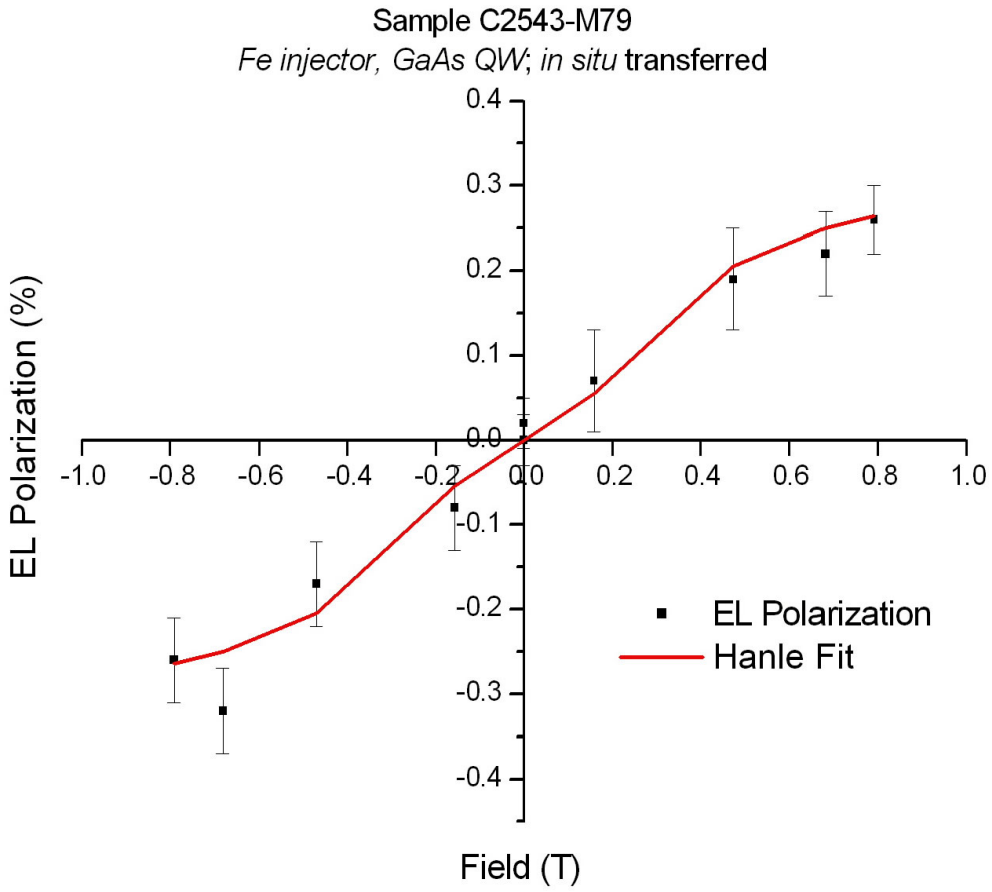

Figure 5.14: EL polarisation and Hanle fit to the data. The sample is an InGaAs QW in GaAs barriers, with an Fe injector. This particular sample was *in situ* transferred directly from the SC growth chamber to a metals growth chamber for Fe deposition.

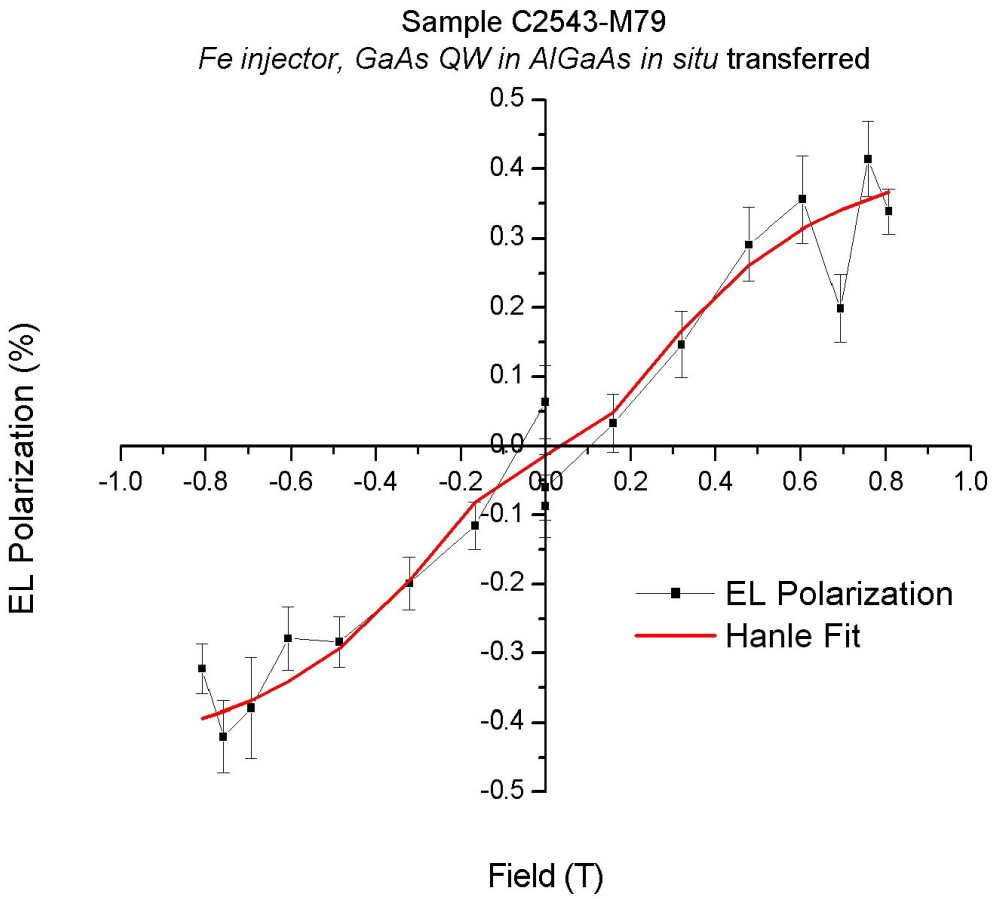

Figure 5.15: EL 77 K polarisation and Hanle fit to the data. The sample is the same *in situ* transferred one as in figure 5.14, an InGaAs QW in GaAs barriers, with an Fe injector.

at a field of 8 kG, whereas we had measured ∼0.25% at RT. We can follow the same formalism as above to fit the data and determine the injected polarisation. However in this case we do not have a measurement of the value of τ. Using the same value for τ we calculate an injected polarisation $\Pi \approx 2\%$. If we estimate that τ increases by 30% to 200 ps [94, 124], the calculated injected polarisation value rises to $\sim 4\%$.

5.4 Conclusions and Future Work

We have presented the theory of spin injection and detection into a semiconductor. Electrical characterisation and light-emission temperature dependence of spin-LED samples contribute to the understanding of this delicate system. The magnetic properties of individual devices also provide valuable insight on the dynamics of the patterned magnetic layers in this experiment. This work on EL and spin injection is still in a developmental stage. We have detected ∼1% spin injection at an Fe/GaAs interface at RT, and ∼2-4% at 77 K. These values however does not yet compete with current reports of spin injection at room temperature, which are approaching 20%.

It is clear that our system and experimental set-up is very fragile. Small optical misalignments can cause a huge drop in the detected intensity, or induce artificial optical polarisations which can be much larger than our real spin-injection signal. The experimental set-up is constantly being assessed in order to improve the accurate detection of spin injection, and reduce the systematic errors which can mask the effects of spin injection. Current work includes temperature and bias dependence studies of optical polarisation. Applied bias voltage determines the current flow and naturally affects the band structure bending of the device. In order to further study the effect of the Schottky barrier we could for instance devise a contact configuration through which we apply a separate bias voltage to the Schottky barrier and to the p-i-n structure. This would induce two current channels, presumably one of which would be spin-filtered and the other not, but could provide insight on spin-selective transport at the interface. Following from our work in chapter 4 on interface roughness and interdiffusion, we could investigate how these affect spin injection. This could be done either by artificially roughening the surface *in situ e.g.* by Ar^+ sputtering, or by post-annealing the

grown films for various lengths of time at a range of temperatures. To complement the EL experiment, we could also perform the reverse, photon-excitation measurement on the same sample. As we have mentioned above, in this experiment a spin-dependent current is detected upon optical excitation by circularly polarised light. Finally, the implementation of thin tunnelling barriers such as MgO (see chapter 6) to improve spin-selective transport is a promising route to improving the efficiency of spin-LEDs.

Acknowledgements

This work is the result of a strong collaboration with S. N. Holmes of Toshiba Cambridge Research Laboratory and R. Mansell of the Semiconductor Physics Group. Many thanks also to I. Farrer and K. Cooper of the Semiconductor Physics group for the growths and processing of the LED structures, and with M. Hickey (Toshiba & Semiconductor Physics Group) for the *in situ* transferred Fe growth. Thanks also to M. Hickey for the 4.6 K electrical data. The Kerr microscope images were taken with J. R. Jeong.

Chapter 6

MgO Growth and Applications

Abstract

We present the deposition of MgO thin (3 - 39 nm) films grown by MBE and sputtering. We characterise these films using RHEED and X-ray techniques, report crystallinity of MgO grown on GaAs, and demonstrate the epitaxial growth of MgO on Fe, and Fe, Co on MgO. Using PNR, we study the effect of MgO on thin magnetic films and observe a decrease in the magnetic moment of these films due to interfacial oxide layers. We also incorporate MgO in a pseudo-spin-valve system where we demonstrate epitaxy-induced magneto-crystalline anisotropy. Finally, we integrate MgO as a buffer layer in a semiconductor/iron garnet optical isolator.

Introduction and Outline

Magnesium Oxide, MgO, has generated a wide scientific interest in recent years due to its potential applications in numerous varied areas. In conjunction with thin magnetic films, it opens possibilities for numerous technological applications such as catalysis, electron spin polarimetry, epitaxy, magnetic recording, and spintronic devices. Tremendous progress has already been made to TMR ratios upon the transition from amorphous AlO_x barriers to oriented MgO layers. Indeed, in early reports the TMR of MgO-based samples has more than quadrupled compared to the Al_2O_3 case [125], and these have now reached values of

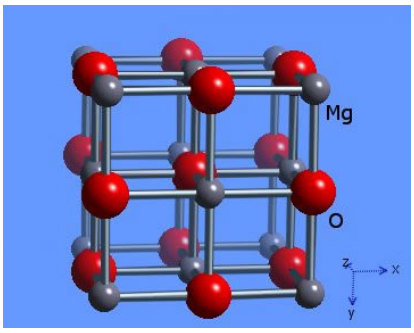

Figure 6.1: (from [128]) The MgO unit cell, rocksalt structure displaying the two (Mg and O) fcc sublattices.

200-300% [126, 127].

In this section we will focus on the fundamental aspects of the growth of samples on MgO substrates as well as the growth of MgO spacer and tunnelling layers. We then discuss the growth mode, and more specifically overview the properties of the Fe/MgO and Co/MgO interfaces. Then we will consider the effect of an MgO barrier on Fe and Co layers grown on a semiconductor substrate. Following that we will study a pseudo-spin-valve (PSV) structure, with an MgO tunnel barrier, and also grown on an MgO substrate. Finally, we will expand on another use of MgO in a semiconductor and magneto-optical waveguide integrated device.

6.1 The Growth of MgO

6.1.1 Introduction and Previous Work

MgO, also known as periclase, is a cubic material in the NaCl, or rocksalt structure. This consists of two fcc sublattices of Mg and O, each displaced with respect to the other by half a lattice parameter along the [100] direction (see figure 6.1).

As we have mentioned, the growth of MgO has generated a lot of interest in recent years, but also in the past, since the early 1990's. In the first instance, we will report on the growth of MgO on a GaAs surface. There are several aspects to the growth of MgO on GaAs that must be considered. These are:

- Substrate surface preparation, *ex situ* and *in situ*
- Growth Method

- Growth Temperature
- Growth Rate
- Sample Cooling Rate

Substrate surface preparation methods vary throughout the literature, but all aim to produce a clean and oriented GaAs surface prior to the MgO growth. These preparation recipes usually include an *ex situ* wet etch before loading the substrate into a vacuum chamber, and then a sputter or heat dry etch *in situ*. These steps are to desorb the native oxide layer of the GaAs. Tarsa *et al.* [129] investigated the effect of a native oxide layer on the MgO/GaAs growth. In this study, they compared chemically treated and antimony-passivated GaAs substrates, and the resultant quality of the MgO layer. The chemically treated substrates were degreased and then etched in NH_4OH:H_2O_2:H_2O (35:15:70) and HCl:H_2O (1:1) solutions to remove polishing damage and residual surface oxides. These were then rinsed for 3 minutes in de-ionised water so as to form a uniform, protective native oxide layer prior to exposure to air, and loading in the vacuum chamber. The Sb-passivated substrates had a 20 nm layer of Sb grown directly onto a GaAs buffer layer *in situ*. From this study, it was established that the orientation of the MgO films depends sensitively upon the treatment of the GaAs(100) prior to growth. The Sb-passivated substrates were found to provide an appropriate template for the growth of highly oriented MgO(100) films. Growth of MgO on a rough but oxide-free GaAs surface resulted in polycrystalline growth, and finally, a remnant native oxide layer appeared to serve as a directional template for MgO(111) films on GaAs(100).

The aim of substrate surface preparation is naturally to provide a seed for epitaxial growth of MgO on GaAs. The epitaxial relation, however, between GaAs and MgO is not straightforward. Reports indicate that 4 unit cells of MgO will sit on 3 of GaAs. Indeed with $a_{MgO} = 4.21$ Å, we find that $3a_{GaAs}/4a_{MgO} = 1.00724$. The is illustrated in figure 6.2, where it was found that for certain growth conditions (in particular temperature) the quoted (110) orientation of MgO grew on GaAs(100). However, it is not certain that this orientation is the only possible one to obtain single-crystal, or at least highly oriented MgO. Indeed claims of MgO(100)‖GaAs(100) have also been made [131, 132].

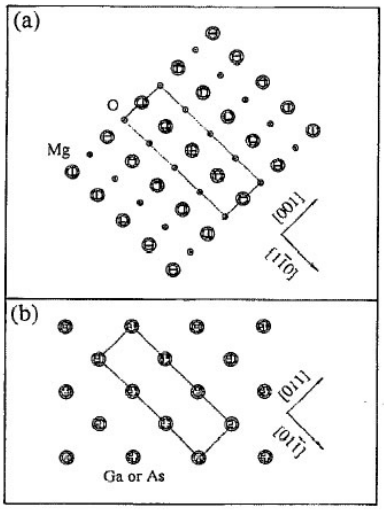

Figure 6.2: (from [130]) Top view of (a) the MgO(110) and (b) the GaAs(100) planes, showing that a superlattice cell made of 4 MgO unit cells has almost the same dimensions as a cell made of 3 GaAs unit cells. $a_{GaAs} = 5.653$ Å; $a_{MgO} = 4.21$ Å

This difference in the quality and orientation of the MgO layer will also depend on the growth method, growth rate, and substrate temperature during growth. Again, a wide range of techniques are reported for the growth of MgO on GaAs. Several groups report epitaxial MgO from pulsed laser deposition (PLD) directly from an MgO target [129, 132–134]. PLD growth was also reported from a Mg target, in an ambient oxygen atmosphere [135, 136]. A Mg target and oxygen background atmosphere was also used in radio frequency (RF) magnetron sputtering by Hsu *et al.* [137]. In addition to sputtering techniques, several groups have obtained high-quality MgO layers from e-beam growth, either directly from high-purity MgO [130, 131, 138], or from a Mg source in an O_2 background atmosphere [138].

Each of these growth methods have specific optimal deposition rates. As is true for generic high-quality layer evaporation, the growth rate should be ∼1 ML/min, in order to favour ordered deposition. For MgO growth, particularly Mg evaporation in an O_2 background atmosphere, the growth rate needs to be further calibrated in order to guarantee stoichiometric growth of MgO in the specific ambient O_2 partial pressure.

As well as the optimum growth method, earlier published results have differ-

ent opinions on the optimum growth temperature for epitaxy of the MgO layer. The substrate temperature will have a large effect on the orientation of the film [130], but consensus shows that elevated temperatures ranging from 400°C to 650°C are preferred. It must be noted, though, that when GaAs is heated much above 500°C in the absence of arsenic flux, non-equilibrium Langmuir evaporation has been observed, resulting in significant roughening of the surface due to As depletion and Ga clustering [17, 139].

Finally, the cooling rate of the sample and newly-grown MgO layer is the last parameter in the growth of MgO. Indeed a fast cooling rate may induce strain, and displacements in the MgO lattice. Reports are less precise about the optimal cooling rate, but it must be understood that controlled cooling *e.g.* ∼10°C/min should be preferred over rapid and large temperature variations [137].

In attempts to grow our own high-quality MgO layers, we have tried MBE growth from a MgO source, MBE from a Mg source in an O_2 atmosphere, and sputter deposition, directly from a magnesium oxide target.

6.1.2 MBE Growth from an MgO Source

In the first instance we grew MgO layers directly from an MgO source. We loaded high-purity MgO crystals in an evaporator in the UHV growth chamber described in chapter 3. MgO being an insulator, the source crystals had to be loaded in a metallic crucible, to allow for the acceleration of electrons towards the source. The crucible for this evaporator was made of molybdenum, chosen due to its elevated melting temperature. However, this evaporator geometry has an obvious drawback in that the heat generated by the accelerated electrons onto the crucible must then be efficiently transmitted to the source crystals.

MgO evaporation was achieved though, at a rate of approximately 1 ML per minute. The power required for this evaporation was very large, with emission currents in the range of 70 mA, which also caused the pressure to rise to $\sim 5.0 \times 10^{-9}$ mbar.

Characterisation measurements on a sample grown by this method are shown in figure 6.3. On the RHEED pattern of the GaAs(100) substrate (a) we observe sharp streaky spots, even distinguish a reconstruction of the surface, and Kikuchi arcs, indicative of a highly ordered, and smooth surface. These show that the

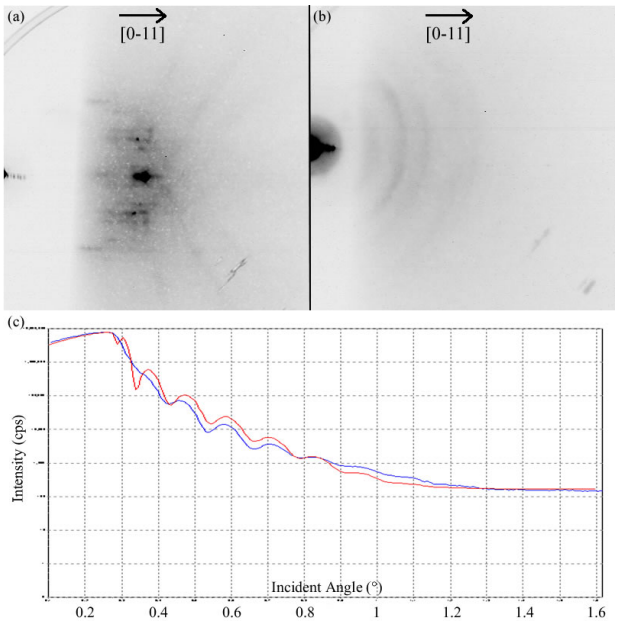

Figure 6.3: Sample ♯*01.07.2005*, grown at 450°C, nominally 32 nm MgO on GaAs(100) waveguide substrate. (a) RHEED pattern of the substrate; (b) RHEED pattern after MgO growth; and (c) XRR measurement on the sample.

semiconductor surface is clean and ordered, hence should be suitable for epitaxial growth of MgO. However, we see on the RHEED pattern of the MgO layer (b) that the growth has resulted in a polycrystalline film, yielding a distinctive ring-like diffraction pattern. The quality of the film and interfaces was checked using XRR, shown in figure 6.3(c). As discussed in chapter 3, the fringes on the reflection pattern allow us to determine the thickness of the film, and the decay can be fitted to provide the roughness of the interfaces. In this case, we have fitted the data to an MgO film 34.2 nm thick, and with interface and surface roughnesses of 1.7 nm and 1.3 nm, respectively.

Although we tried a range of growth temperatures (from RT to 600°C) and various substrate preparation methods, we never achieved single crystalline growth of MgO on GaAs using this evaporation technique. As previously mentioned, one possible reason for this is the sub-optimal heat transfer from the crucible to the isolating source crystals. This might mean that the source material is not heating up uniformly, or not degassing effectively. Also, it was noted upon removing the evaporator from the chamber, the large amount of power required to evaporate the MgO caused softening or perhaps evaporation of the

crucible itself, thus leading to potential Mo impurities in the MgO films. We know though that there were only very few - if any - of these, as the density of the film remained close to that of bulk MgO, according to the XRR fits.

6.1.3 MBE Growth from a Mg Source

We also attempted to grow MgO layers using Mg evaporation in an O_2 background atmosphere. These growths were inspired by the technique of Tegenkamp *et al.* [140]. We again used the UHV growth chamber described in chapter 3, in which we loaded high-purity (99.9+%) Mg metal in a Mo crucible. Mg has a low melting point (650°C), but is fairly soft, and is very chemically active. This means that it will react easily in air, and therefore will require thorough degassing after loading in the chamber.

The growth of MgO layers using this method is a multi-step process. In the first instance we grew a very thin ($\sim$ 4 ML) Mg layer on the clean GaAs substrate. Once this was done, we interrupted the growth, and exposed the film to an oxygen partial pressure of 2×10^{-6} mbar for 2 minutes, and then annealed it at 400°C for 15 minutes. There are two reasons for this first layer. Firstly, as discussed previously, the quality of the GaAs surface is crucial for growth of an ordered layer. Therefore it is necessary to avoid exposing the bare GaAs surface to oxygen, so it was necessary to deposit the 4 ML of Mg first, which would then be completely and stoichiometrically oxidised upon exposure to the oxygen. The reason for the anneal step is to favour the formation of a crystalline structure in the film, as a seed for further epitaxial growth.

After this initial deposition of Mg, we cooled the samples down to $\sim 150 - 200$°C for further Mg evaporation, in an ambient oxygen atmosphere. For the growth of thicker MgO layers, it is largely preferable to oxidise the Mg atoms during the growth process, rather than attempting to oxidise layers or clusters of metal after the fact [141]. As long as the Mg evaporation rate is not too high, this should allow for fully oxidised MgO films. The best stoichiometry of MgO is believed to be obtained with an oxygen partial pressure of $\sim 3 \times 10^{-7}$ mbar and a deposition rate of 1 ML/min [140].

MgO films deposited using this method were not found to be perfectly epitaxial, but exhibited some orientation. The fact that MgO is an insulator causes

some difficulty to take LEED patterns from these samples. Indeed, the low-energy incident electrons perpendicular to the surface cause the sample to charge up, which tends to prevent elastic scattering from the crystal[1]. Unfortunately the RHEED system was inoperative when these samples were grown. Therefore, we relied on *ex situ* characterisation methods, in this case XRR, XRD and MOKE, as described in chapter 3. The MOKE results will be shown and discussed in section 6.3 below.

Figure 6.4(a) is an XRR scan of sample ♯*12.09.2006*, which was nominally 26 nm of MgO grown on a GaAs(100) substrate. The fit to the XRR scan gives us several results. XRR measures changes in layer densities only (not crystal structure or atomic species present). The fit shown is for a layer density of 3.3 g/cm^3, which is very close to the actual density of bulk MgO (3.58 g/cm^3). In addition to this, the XRR fit yields the roughnesses of the interface and film. These are found to be under a nanometre ($\sim$ 7 Å) at the MgO/GaAs interface, and the MgO film has a roughness of 1.2 nm. Finally, the XRR also provides a thickness measurement, which in this case was determined to being 14.4 nm. The inconsistency between this and the nominal growth thickness is very large in this particular case, due to inaccuracy during the growth calibration and variations of the evaporation rate during deposition.

The XRD results shown in figure 6.4(b) display two features which are of interest to us. The first one is the stand-alone broad peak around $2\theta = 39°$. This can be identified as an MgO diffraction peak. It is slightly shifted compared to the expected peak position, but we are certain that it is a layer peak and not a substrate peak, due to the width (full width at half maximum $\simeq$0.9°). The second feature in the graph is the shoulder in GaAs peak, around $2\theta = 43.5°$. This peak could be an a Mg peak, though again this is not conclusive for this sample. These two deductions and the mismatch of the peaks indicate that perhaps we have not reached the ideal stoichiometric conditions for the growth of MgO using this method, though the appearance of the peaks is an encouraging

[1]There are two main strategies to overcome this. The first is to have a sufficient number of defects in the insulator which provide carriers such that a small conductivity results, though the disadvantage is that one studies a modified version of the oxide. The other possibility is to deposit a thin film of the oxide on a conducting substrate, which would give enough (tunnelling) conductivity for electron diffraction but in this case we may not really be studying the surface properties of the real bulk material.

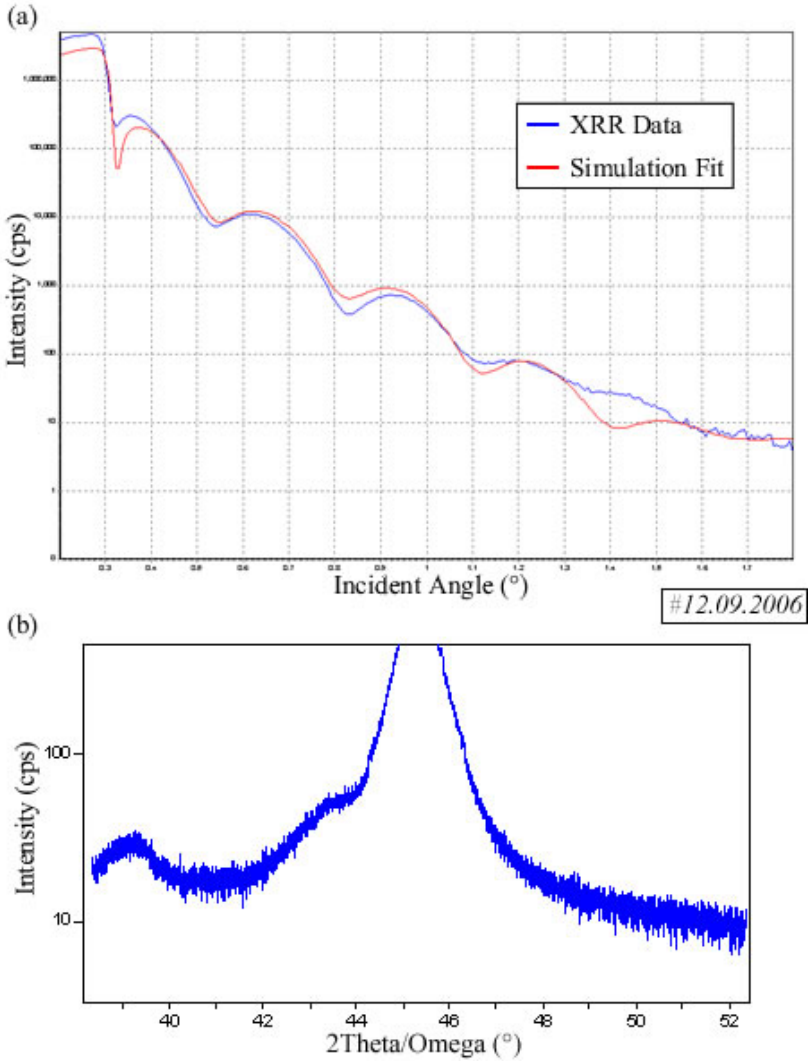

Figure 6.4: Sample ♯*12.09.2006*, nominally 26 nm MgO on GaAs(100), by Mg evaporation in O_2 background. (a) XRR scan; and (b) XRD $2\theta/\omega$ scan.

start.

6.1.4 Sputter deposition

The final deposition technique that we attempted was sputter deposition. In this case we used RF magnetron sputtering, in which an Ar plasma oscillates at a determined AC frequency (typically 13.56 MHz). Electrons in the plasma gather additional energy from this oscillation, which results in further ionisation by the high-energy tail of the electron energy distribution. This then produces a higher ion current at the same applied power than in simple DC mode. Another key advantage of RF sputtering is that the cathode receives no net current from the plasma. The incident ions from one part of the RF cycle are compensated for by the incident ions from the other part of the cycle. In a sense, the cathode and anode switch places once each RF cycle, resulting in no net current or charging [58]. This also makes it possible to sputter insulating materials. This sputter deposition was done on a CEVP Gamma 1000M commercially designed sputtering system, with a base pressure of $3 - 8 \times 10^{-9}$ mbar. The Ar plasma pressure was 2 mbar during deposition. In the first instance, we had to grow several samples with a shadow mask obscuring an area on the sample, so that the step could be measured using an AFM, yielding a thickness calibration. Following this we were able to grow accurate thin layers fairly easily. The quality of the MgO layers grown by this method will be discussed briefly in section 6.5 below.

6.2 Fe/MgO and Co/MgO Interface properties

The highest quality structures and devices are single-crystal samples. However, as we have seen for the growth of MgO on GaAs, epitaxy is not always easily obtained. In this section we will briefly move away from semiconductors, and study the growth, and interfaces of magnetic layers (Fe and Co) directly on an MgO substrate. The magnetic properties[2] of these layers will be addressed below

[2]We attempted to determine the onset of ferromagnetism and the magnetic anisotropies of ultra-thin Fe and Co films grown on MgO, with an *in situ* MOKE experiment of layer-by-layer deposition on MgO(100). However we found that for such thin coverages of magnetic metals, and including the fact that MgO is transparent, the polarisation of the reflected laser beam was lost, most likely through dispersion in the substrate crystal, thus no Kerr rotation could be measured.

$a_{MgO} = 4.211$ Å		
$a_{Fe,bcc} = 2.866$ Å	$a^{45^\circ}_{Fe,bcc} = \sqrt{2} \times (a_{Fe,bcc}) = 4.054$ Å	$\frac{a_{MgO}}{a^{45^\circ}_{Fe,bcc}} = 1.039$
$a_{Co,bcc} = 2.827$ Å	$a^{45^\circ}_{Co,bcc} = \sqrt{2} \times (a_{Co,bcc}) = 3.999$ Å	$\frac{a_{MgO}}{a^{45^\circ}_{Co,bcc}} = 1.053$

Table 6.1: Lattice parameters for the growth of Fe and Co on MgO(100).

in the context of the PSV sample below (section 6.4).

Epitaxial growth of Fe and Co on MgO(100) is reasonably straightforward, despite requiring a 45° in-plane rotation [142, 143]. Thus we have Fe(100)[011]‖ MgO(100)[001], and the direct equivalent for the case of Co. The lattice parameters demonstrating this epitaxial relation are shown in table 6.1. We see that there is a 3.9% and 5.3% lattice mismatch for the epitaxial growths of Fe(100) and Co(100), respectively, on MgO(100).

6.2.1 Fe on MgO

There have been several studies, both experimental and theoretical, of the Fe/MgO interface [144–150]. In addition to the aforementioned epitaxial relation, a LEED and AES study determined that the Fe atoms of the first deposited layer onto a clean MgO surface sit atop the O atoms [145]. The literature, however, is not definite on the formation and presence of an FeO layer at this interface. It has been reported [151], but also rejected [148]. The root of this discrepancy is not very well determined, though it has been suggested that the presence of C impurities on the substrate surface could lead to various degrees of reaction with oxygen atoms present. However, we believe that due to the presence of oxygen atoms at the surface and the affinity of Fe to bond with O, it is likely that Fe and O will react in this system. There is virtually no diffusion of Fe into the MgO for growth temperatures up to 350°C , but for high temperature growth (600°C), interdiffusion occurs and Fe is present in an oxidised state [146].

Structural defects introduced by the slight lattice mismatch are also a potential issue for the growth of high-quality Fe films on MgO. Di Bona *et al.* [144] study a 10 ML (≈1.4 nm) Fe film grown on an MgO(100) substrate. As expected, they find that the 10 ML film has a bct distorted structure. Annealing

the film up to 300°C improved its crystalline quality while maintaining it in the bct structure, and higher annealing temperature (400-500°C) resulted in islands, which were able to relax to a bcc structure. Upon growing thicker Fe layers, and not necessarily annealing them at such high temperatures, it is established that the film relaxes to its bcc structure, with bct and bcc domains co-existing [145], always due to the slight lattice mismatch between the two materials. Finally, Vassent *et al.* [146] study the complementary growth of MgO on Fe(100). The conclusions of their study are similar for the ultra-thin regime of the MgO film (pseudo-morphic growth for t<4-5 ML), but for a thicker layer they find the relief of the misfit strain occurs via a dislocation along the direction of the MgO{110} plane.

6.2.2 Co on MgO

The growth of Co on MgO(100) is much less documented than that of Fe. As we have previously mentioned, we expect Co to grow in the bcc structure in the first instance on MgO(100) due to the favourable epitaxial relations upon a 45° in-plane rotation (table 6.1). Sicot *et al.* [147] performed an X-ray Photoemission Spectra (XPS) study of the interface, and detected no evidence of CoO formation. However, Sicot *et al.* [147] were not able to extend their study to high temperatures due to the presence of an Fe buffer layer in their samples. As with Fe, we expect the presence of O to affect the Co film, in particular at elevated temperatures.

6.2.3 Interface Tunnelling Properties

The theory of spin-dependent tunnelling through a thin MgO barrier is of direct interest for numerous device applications requiring high MR (briefly introduced in section 6.4). *Ab initio* calculations predict large TMR values in single-crystalline magnetic tunnel junctions, for both Fe/MgO/Fe [149, 152] and Co/MgO/Co [143]. The theoretical calculations are driven by the different tunnelling mechanisms for the majority and minority spin channels in single crystal junctions. The symmetry of the Bloch states at the Fermi level and the symmetry-related decay of the evanescent states in the barrier layer are different for the majority and minority electrons, thus leading to a difference in conductance of the two spin

channels from a FM, and hence the large TMR. In addition to this, however, the tunnelling conductance is affected by interfacial effects, such as scattering and resonance effects [153]. Unfortunately, these theoretical studies do not fully address the consequences of such interfacial effects. It is usually assumed that the structure is fully and perfectly epitaxial, neglecting even the lattice mismatch at the interface. Butler *et al.* [149] discuss briefly the interfacial states and tunnelling through interface resonance states, though the details of this are beyond the scope of this thesis.

Xu *et al.* [154] performed a systematic, quantitative study of the effect of disorder on the MR of an idealised FeCo/*vacuum*/FeCo magnetic tunnel junction (MTJ) system. They find that disorder at the interfaces will have two effects. The first is to destroy the point group symmetry for states with Δ_1 symmetry, and thus the surface state with that symmetry. The second effect of roughness is simply a reduction of the barrier width, therefore an enhancement of the conductance, which depends exponentially on the barrier width. Xu *et al.* [154] consider these two competing effects and conclude that the current reported experimental TMR values of a few hundred percent (200-300% [126, 127]) are still in the roughness/disorder-limited regime.

The effect of interface scattering mechanisms on tunnelling properties has not yet been well quantised. However, the extremely high predicted TMR ratios in the theoretical calculations above provide motivation to fabricate such a structure experimentally. Epitaxial growth of samples in a UHV chamber will result in the cleanest possible interfaces. The slight lattice strain will naturally remain, but clean surfaces are obtainable and it is possible to minimise interdiffusion effects, thus leading to a real device as close as possible to the ideal model.

6.3 MgO as a Tunnelling Barrier

6.3.1 The Impedance Mismatch Obstacle

In the late nineties it became apparent that spin injection into a semiconductor using a magnetic semiconductor was more efficient than using a metallic ferromagnetic injector [115]. One explanation for this was first put forward by Schmidt *et al.* in 2000 [97]. The fundamental obstacle for efficient spin injection

from a FM metal was identified as being the impedance mismatch between the FM metal and the semiconductor. Schmidt *et al.* [97] indeed found that in the diffusive transport regime, only a current with small spin-polarisation can be injected into a SC even if the conductivities of the SC and FM are equal.

A theoretical solution for this problem was advanced simultaneously by Rashba [98] and Smith *et al.* [99]. Moving away from the diffusive regime, a tunnelling interface or barrier would act as a spin-selector, and greatly enhance the spin injection efficiency. MgO is again of current interest for this use as a tunnel barrier in spin-injection devices. Along with the quality of the interfaces and barrier, as discussed above in section 6.2, the oxide layer itself may affect the magnetic properties of the injector. In the case of a spin-injection structure such as Fe/MgO/GaAs(100), for instance, the spin-polarisation at the interface is a critical parameter for device performance [155], and therefore it is important that the magnetic moment of the magnetic film is not affected by the presence of the oxide layer. This will also be the case for MTJ structures, where the oxide barrier may have damaging effects on the magnetic layers [126, 127].

Following a similar study for AlO_x barriers [90], in order to characterise the effect of the MgO tunnel barrier on the FM injector, we have grown three samples, varying the MgO film thickness and the FM injector, all on a GaAs(100) substrate. These were 5 nm Fe injector with 1.5 and 2.8 nm MgO barriers, and a third sample of 5 nm Co FM layer with a 1.5 nm MgO barrier. All three barrier samples were grown using Mg evaporation in an O_2 background (see section 6.1.3) in the UHV MBE chamber, and Au-capped before unloading them from the chamber.

6.3.2 Interface Roughness and MgO Crystallinity

We first characterised the samples *ex situ* using XRR, in order to obtain estimates for the thicknesses and interface roughness amplitudes of each layer. The XRR results are summarised in table 6.2, and a representative result and fit to the data are shown in figure 6.5. We notice slight discrepancies between the nominal and estimated thicknesses for the barrier layers as well as the FM layers. The explanation for this is the instability in the rate of evaporation, particularly of the Mg, but also for such thicknesses the XRR fit loses accuracy due to the

	Layer Material	t ±0.1 (nm)	ρ ±0.1 (nm)
♯*20.09.2006*	GaAs	*n/a*	0.91
	MgO	2.83	0.89
	Fe	5.93	0.86
	Au	7.34	0.73
♯*28.09.2006*	GaAs	*n/a*	0.36
	MgO	1.29	0.36
	Fe	6.22	0.72
	Au	8.60	0.77
♯*30.09.2006*	GaAs	*n/a*	0.99
	MgO	1.35	0.45
	Co	6.60	0.64
	Au	6.16	0.75

Table 6.2: Summary of XRR simulation fit results, yielding thickness, t, and interface roughness amplitude, ρ, of each layer, for the MgO tunnel barrier study samples.

small number of Kiessig fringes detected in the low-angle incidence range of the measurement. Of notable interest for our purposes though is the roughness amplitude for each sample layer. The XRR fit indicates that despite a fairly poor GaAs surface in two cases, the MgO layer and subsequent FM layer had reasonably low interface roughnesses.

As we were unable to take LEED or RHEED patterns (*in situ*) for these samples, we had to rely on *ex situ* measurements to characterise the crystallinity of the layers. We decided not to attempt XRD scans as the MgO layers were so thin, but turned directly to MOKE magnetometry. Performing MOKE with various field orientations (in-plane) would be an indication as to whether or not the FM films displayed any magneto-crystalline anisotropy. The magneto-crystalline anisotropy reflects the crystalline structure of an epitaxial film, so in this case such an anisotropy would be a demonstration of crystalline order. The MOKE loops for two of these samples are shown in figures 6.6 and 6.7.

Sample ♯*20.09.2006* has a 2.8 nm MgO barrier. As we see in figure 6.6, the loops taken with four applied field directions are not identical, which immediately indicates a crystallinity of the Fe film. Upon further examination, and taking into consideration the applied field direction, this film displays a uni-axial anisotropy. Indeed, the MOKE loops show what tends to be an easy axis with the field along the [011] direction, and a hard axis with the field applied perpendicular to that,

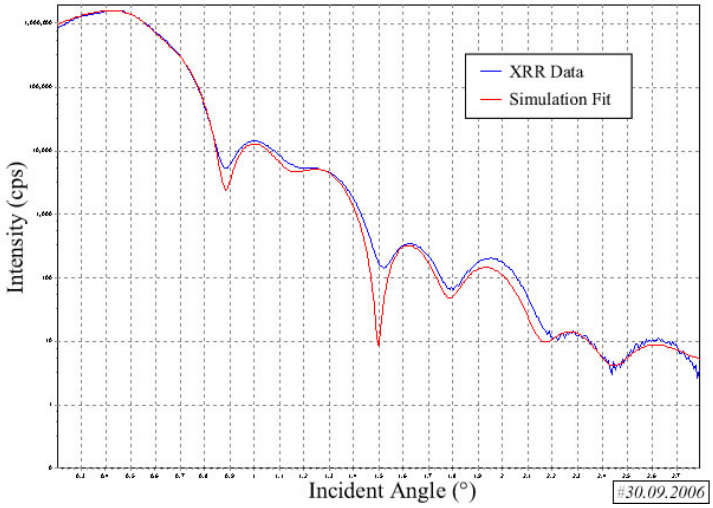

Figure 6.5: Sample ♯*30.09.2006*, nominally Au cap, 5 nm Co, 1.5 nm MgO on GaAs(100); MgO barrier grown by Mg evaporation in O_2 background. XRR data (blue) and fit (red). The fit parameters are summarised in table 6.2

along the $[0\bar{1}1]$ direction. Furthermore, the two other loops, at 45° to these, are very similar to each other, both displaying an intermediate switching behaviour.

This is not the behaviour we expect from an epitaxial Fe film on epitaxial MgO, which is a cubic anisotropy, with four-fold symmetry. However, this anisotropic behaviour is suspiciously similar to that of Fe grown direction on GaAs(100). Indeed for such a system and ultra-thin Fe, we expect this uni-axial anisotropy. This makes it quite difficult to establish what has happened with this film. 2.8 nm of MgO corresponds to a layer ∼13 ML thick, therefore we expect that to entirely cover the GaAs surface, hence the surprising presence of this uni-axial anisotropy. However, we notice that the roughness of this substrate and of the MgO barrier was quite high, both ∼0.9nm, which would have been quite detrimental to the quality and crystallinity of the subsequent Fe layer. One explanation would be that the Fe film has relaxed into crystalline order during the growth. From an initially polycrystalline growth, epitaxy might have occurred in the latter stages of the Fe growth. This might have been helped or brought on by the fact that following the MgO growth, the substrate temperature was still slightly above 100°C at the start of the Fe growth. Therefore, we might have an initially polycrystalline film that then relaxes into order, and thus displays a

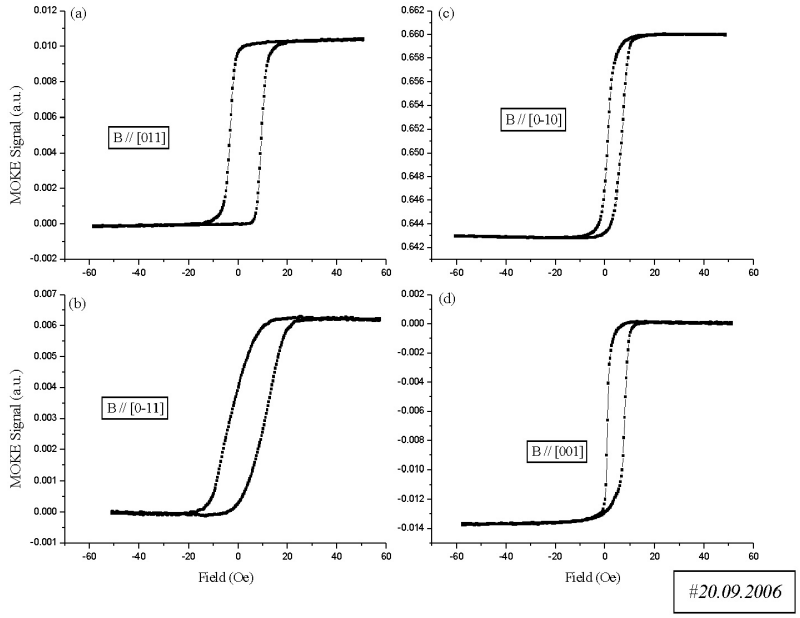

Figure 6.6: Sample ♯*20.09.2006*, nominally Au cap, 5 nm Fe, 2.8 nm MgO on GaAs(100); MgO barrier grown by Mg evaporation in O_2 background atmosphere. MOKE loops for the specified field orientations.

strain-induced uni-axial anisotropy.

Figure 6.7 shows the MOKE loops measured on sample ♯*28.09.2006*, which is a thinner (nominally 1.5 nm) MgO barrier, but otherwise grown under the same conditions, and with the same Fe layer. These MOKE loops do not display the same uni-axial anisotropy, but rather a cubic anisotropy. Indeed we see that the loops can be paired up as easy and hard axes, with loops in a pair corresponding to perpendicular field directions. In addition to this there are a few minor features which we notice. Namely the 'double switching' in loop (a) which indicates that the magnetisation is switching from a parallel, to perpendicular, and then to anti-parallel alignment in two distinct steps. This two-step switching is not present in loop (b), but its shape is still characteristic of an easy axis of magnetisation switching. The double switching and such a square easy axis loop are indicative of a highly crystalline FM layer. Furthermore, the cubic anisotropy is confirmed by the two perpendicular hard-axis loops (c) and (d), which show a rotation of the magnetisation of the layer and then a jump. In addition to this, the direction

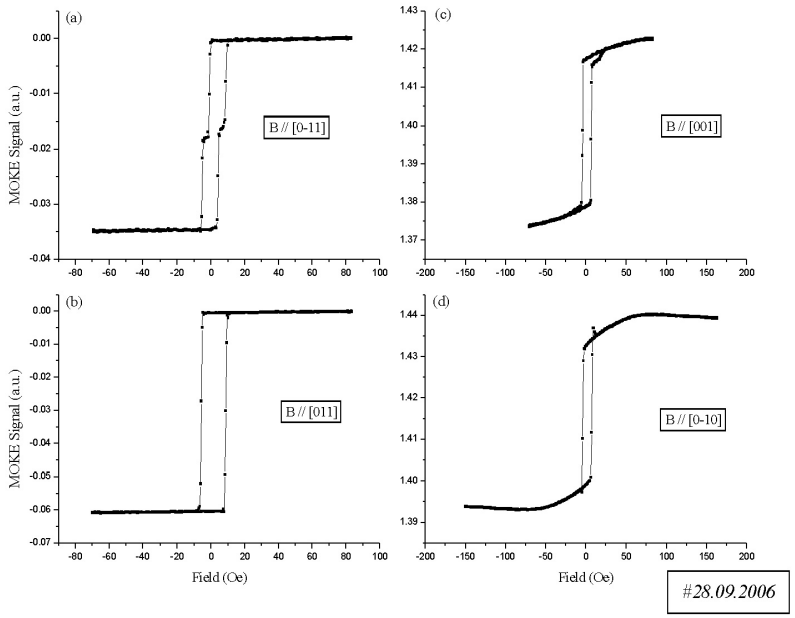

Figure 6.7: Sample ♯*28.09.2006*, nominally Au cap, 5 nm Fe, 1.5 nm MgO on GaAs(100); MgO barrier grown by Mg evaporation in O_2 background atmosphere. MOKE loops for the specified field orientations.

of the Fe anisotropy corresponds to that which we expect, for growth on MgO, considering the 45° in-plane rotation of the Fe lattice upon the MgO lattice (see details in section 6.4), thus further demonstrating the crystallinity of the film. We note that for this sample the roughness amplitude of the substrate surface and Fe/MgO interface were low, at ∼0.3 nm, which would be very favourable to high-quality crystalline growths.

The fact that the Fe films display anisotropies for these two samples is indicative of their partial epitaxy, which in turn means that the MgO barrier was crystalline, and hence a suitable seed for epitaxial growth. However, the results presented for these samples are not consistent for what are nearly identical samples. Furthermore, we performed MOKE measurements on the third sample (not shown) and found that the loops in all four applied field directions were identical, hence pointing to a polycrystalline Co layer. We believe that the Fe and Co evaporations and growths are fairly well controlled, unlike the MgO growth, which was still in a development stage. The reason for the difference in the qual-

Sample	FM Layer	t (nm)	ρ (nm)	Magn. Moment (μ_B)
♯*20.09.2006*	**Fe**	5.1 ± 0.4	0.9 ± 0.1	2.06 ± 0.03
♯*28.09.2006*	**Fe**	4.9 ± 0.3	0.7 ± 0.1	2.10 ± 0.02
♯*30.09.2006*	**Co**	7.1 ± 0.9	0.4 ± 0.1	1.6 ± 0.1

Table 6.3: Summary of PNR fit results for the FM layers in the MgO barrier samples, showing the best fit parameters for the thickness, t, roughness, ρ, and magnetic moment.

ity of these layers is a lack of control of the evaporation rate of Mg during the MgO deposition. Rapid changes in this rate will lead to poor stoichiometry and crystallinity of the barrier layer.

6.3.3 Polarized Neutron Study of Barrier Samples

As we have seen, PNR is a very powerful technique enabling us to determine structural and magnetic properties of samples simultaneously. We performed PNR on our three MgO tunnel barrier samples. Fits to the data provided values for layer thickness, roughness and atomic density to complement the XRR results, and in addition to this an estimate of the magnetic moment of the FM layer.

A sample of our PNR data and fits is shown in figure 6.8. This shows the up- and down-spin reflectivities, and the spin-asymmetry for sample ♯*20.09.2006*. The spin-asymmetry is simply the difference between the normalised spin-up and spin-down signals, from which it is possible to extract the magnetic moment. In order to obtain the best physically accurate fits to the PNR data, we initially started the fitting using the above XRR results, and required consistency between the two reflectivity techniques. Once a suitable fit was obtained we could then begin to slightly vary the magnetic moment of the FM layer, and the atomic densities of the barrier and Au cap. As in chapter 4, we allowed the Au cap density to vary from its bulk value to account for the possibility of imperfect epitaxial growth of the cap. Finally, fitting the spin-asymmetry allowed us to refine the determined magnetic moment value.

The results of the fits are summarised in tables 6.3 and 6.4. We note consistency with the XRR results for the thickness and roughness amplitude values within the errors of the two measurements. Two features which stand out are the decrease of the magnetic moments of the FM layers, and of the atomic density

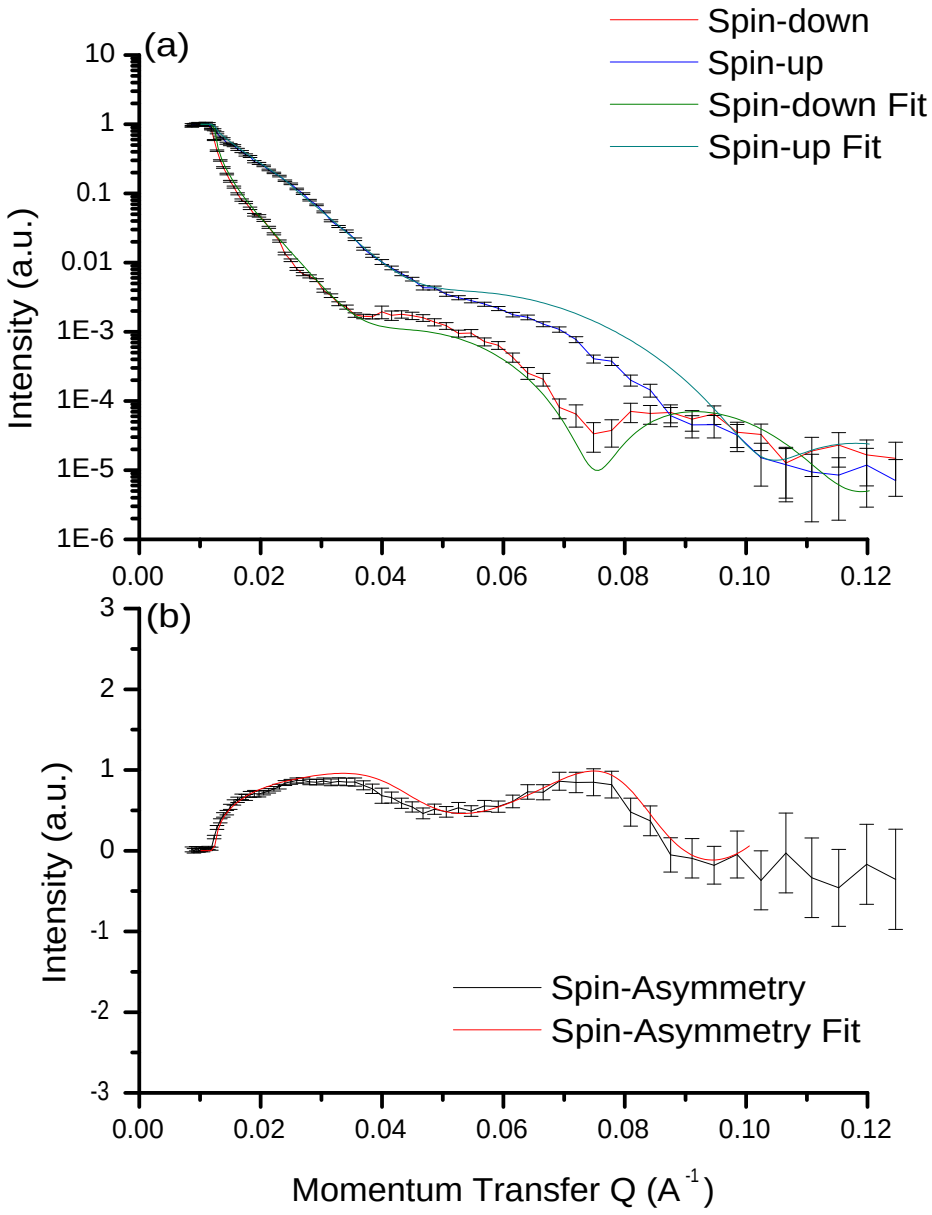

Figure 6.8: Sample ♯*20.09.2006*, nominally Au cap, 5 nm Fe, 1.5 nm MgO on GaAs(100); MgO barrier grown by Mg evaporation in O_2 background atmosphere. Normalised PNR intensity measurement and fits to (a) spin-up and spin-down reflectivities; and (b) spin-asymmetry data.

Sample	t (nm)	ρ (nm)	N (10^{28} m^{-3})
♯*20.09.2006*	2.8 ± 0.2	0.8 ± 0.1	8.2 ± 0.4
♯*28.09.2006*	1.1 ± 0.1	0.3 ± 0.1	8.7 ± 0.4
♯*30.09.2006*	1.2 ± 0.2	0.9 ± 0.1	8.3 ± 0.5

Table 6.4: Summary of PNR fit results for the MgO barriers, showing the best fit parameters for the thickness, t, roughness, ρ, and atomic density, N.

of the MgO tunnelling barriers[3].

We observe a slight decrease of the magnetic moment in all three samples from the theoretical values of 2.2 and 1.8 μ_B for Fe and Co, respectively. Similarly to the argument of chapter 4, we attribute this to interface roughness and interdiffusion. In these cases, we have a formation of FeO or CoO at the interface between the MgO tunnelling barrier and the FM layer. This intermixing is enhanced due to interface roughness, which increases the contact surface area between the two layers.

The variation in the atomic density of the MgO barriers is indicative of non-stoichiometric growth of MgO. As we have seen (section 6.1.3), our growth of MgO by Mg deposition in an O_2 background atmosphere was not yet sufficiently optimised to yield epitaxial and perfectly stoichiometric films. The decrease in atomic density indicates Mg-rich layers, thus lack of O_2 present during growth, due to the large fluctuations (increase) of the Mg evaporation rate.

MgO Barriers Conclusion

MgO barriers are a very promising route to solving the impedance mismatch obstacle at a FM/SC interface. We must not however neglect the quality of the layers and interfaces, which can greatly affect magnetic properties, and dramatically alter transport properties.

[3]Bulk value: $N_{MgO} = 10.71 \times 10^{28}$ m^{-3}.

6.4 Co/MgO/Fe Pseudo-Spin-Valve

6.4.1 Motivation: Magnetic Tunnel Junctions

Magnetic tunnel junctions, consisting of two ferromagnetic electrodes separated by an insulating layer (tunnel barrier) exhibit magneto-resistance at room temperature. MTJs are arguably the most promising route to developing high-performance MRAM, magnetic sensors, and novel spintronic devices due to the high achievable signal-to-noise ratio. These devices rely on the MR ratio of the multilayer, defined as:

$$\frac{\Delta R}{R_P} = \frac{(R_{AP} - R_P)}{R_P} \tag{6.1}$$

where R_P and R_{AP} are the junction resistance when the magnetisation of the two electrodes are aligned in the parallel and anti-parallel states, respectively [156].

Therefore, it is obvious that controlled and independent switching of the two FM layers is crucial to efficient operation of MRAM or such devices. Large TMR values of up to 70% at RT have been reported using amorphous AlO_x [157], but recent research reports ∼200% TMR using highly oriented MgO barriers [126, 127]. This MR ratio is constantly being improved as the growth methods are developing, and has been theoretically predicted to reach 1000% for an Fe/MgO/Fe system [149, 152], and even higher for a Co/MgO/Co MTJ [143].

6.4.2 MBE Growth and Structural Characterisation

We have grown a PSV structure on an oriented MgO substrate in the UHV growth chamber described in chapter 3, and using e-beam evaporation from an MgO source (see section 6.1.2). UHV MBE enables us to grow clean and crystalline multilayer structures. The PSV was based upon a Co/MgO/Fe trilayer, without anti-ferromagnetic material, so essentially two free magnetic layers (see inset in figure 6.10). It is clear that the quality of each layer and of the oxide barrier is paramount to achieving high MR ratios. Furthermore, a single crystal MgO tunnelling layer provides the necessary seeding for an epitaxial top electrode, which then enables us to control its magnetisation state independently of the bottom FM layer.

As we have seen, epitaxial relations link the growths of Fe/MgO and Co/MgO

	Layer	Thickness (nm)	Roughness (nm)
MgO	(substrate)	n/a	0.3 ± 0.1
Fe	(bottom electrode)	4.4 ± 0.1	0.2 ± 0.1
MgO	(tunnel barrier)	3.2 ± 0.1	0.5 ± 0.1
Co	(top electrode)	7.7 ± 0.1	0.6 ± 0.1

Table 6.5: Summary of XRR fit results for the MgO-based PSV.

upon a 45° in-plane rotation, with Fe(100)[011]‖MgO(100)[001] [142]. In order to achieve epitaxy and obtain smooth interfaces we grew this sample at high temperature ($T = 200$°C) and in the best pressure conditions ($p_{growth} = 3 \times 10^{-9}$ mbar). We were able to verify the epitaxy of the structure *in situ* by RHEED. Figure 6.9 shows the RHEED patterns of the substrate and each subsequently grown layer, for three orientations. Kikuchi arcs on the substrate patterns, and distinct spots and streaks for each layer confirm the single-crystal growth throughout the entire multi-layer structure.

We performed further interface characterisation *ex situ* using XRR. The resultant diffraction and a fit to the data are shown in figure 6.10. The fit to the XRR data provides thickness and roughness values for each layer, as summarised in table 6.5. The XRR fit confirms that all the interfaces were extremely smooth. As expected, the MgO tunnel barrier had a slightly higher roughness than the substrate and Fe layer, for the reasons explained in section 6.1.2, and this roughness was then carried through to the Co top electrode.

6.4.3 Magnetic Characterisation: Independent Switching and Polarized Neutron Reflectivity

Knowing that both layers were epitaxial, we wanted to verify independent switching, and check the easy axes directions for the layers. This was done using vector MOKE magnetometry, and the loops for four crystal directions are shown in figure 6.11. Indeed these show independent switching of both FM layers and indicate that the easy axes (sharpest switching) tend to be at 45° to the *e.g.* (010) crystal orientation of the edge of the (cubic) MgO substrate. This confirms the magneto-crystalline anisotropy of both FM electrodes. By delicately varying the range of field sweep, we were also able to observe minor loops for the structure,

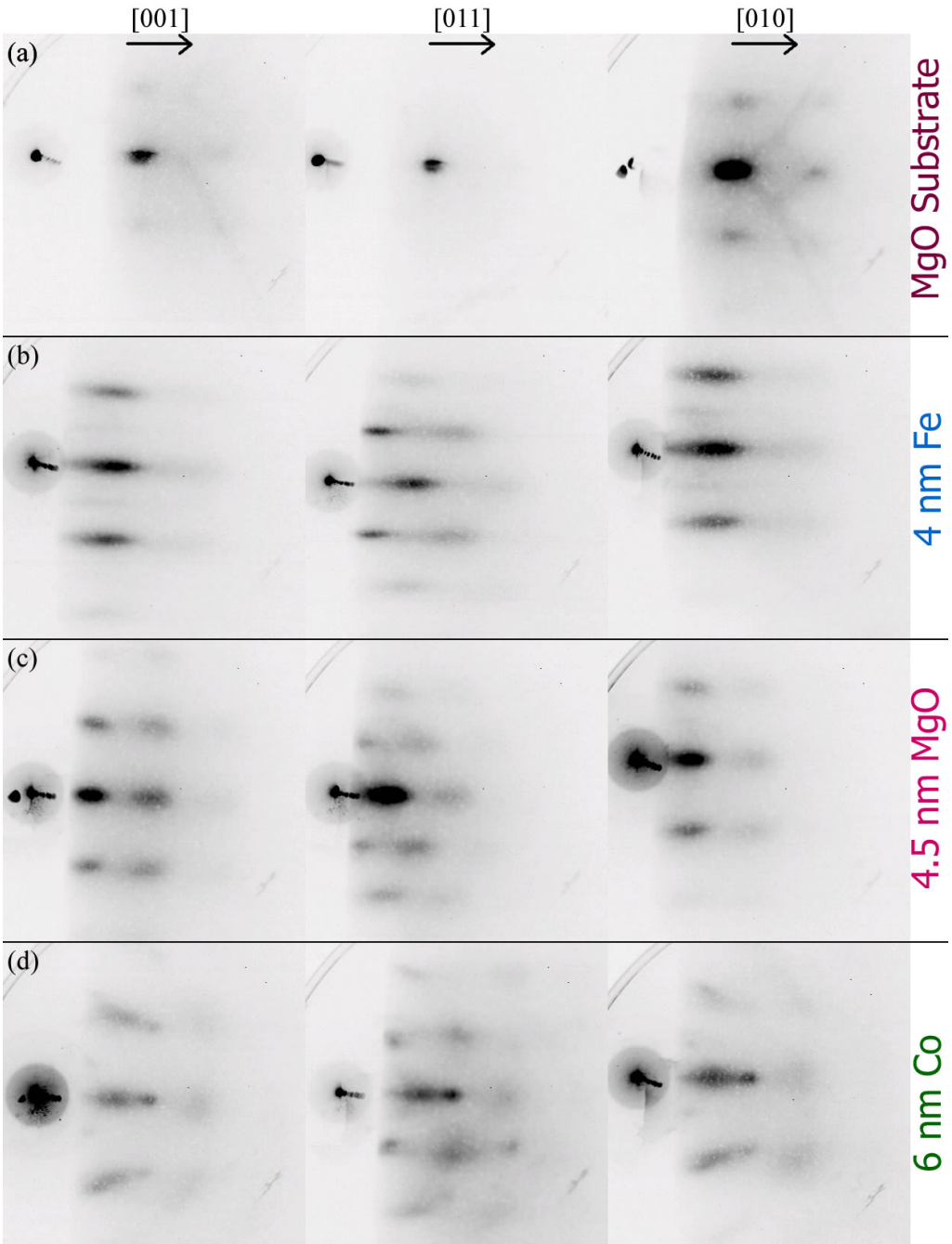

Figure 6.9: RHEED patterns for the substrate and each layer of the PSV sample, along three directions. (a) MgO Substrate; (b) Fe layer; (c) MgO barrier; and (d) Co layer. The thicknesses indicated are nominal.

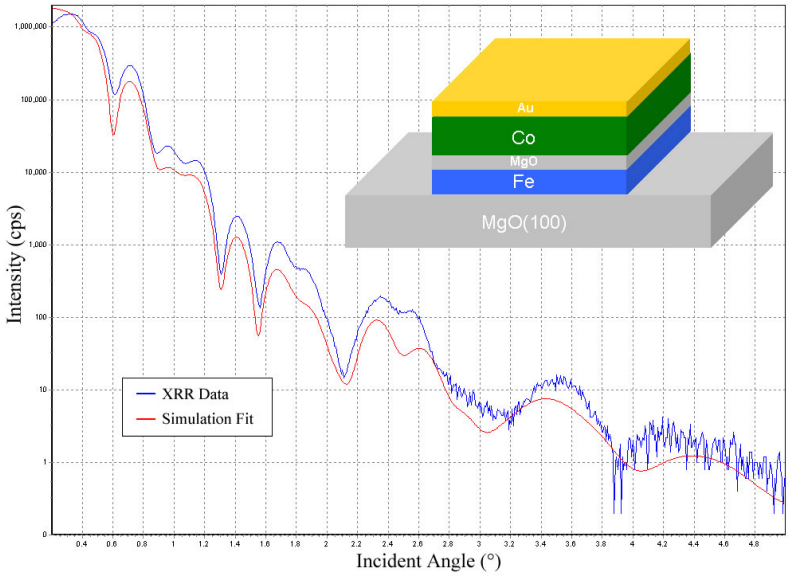

Figure 6.10: XRR results for the PSV Structure. *Inset*: Schematic diagram of the sample.

in which we only switched the Fe layer (not shown).

The fact that the layers were switching independently indicated that they were not pinhole-coupled magnetically. In addition to this, we wanted to further characterise the MgO barrier by verifying that it was indeed epitaxial and insulating. We performed AMR measurements. The AMR effect manifests itself as a difference in resistivity depending on the direction of the current with respect to the spontaneous magnetisation [158].

We performed AMR measurements using a collinear 4-point probe system, simply lowered to contact the (Au cap of the) sample. We applied a constant current across the outer probes and measured the change in voltage across the two inner probes while sweeping an external magnetic field, thus yielding a measurement of the resistivity as a function of magnetisation. We applied the field in the plane of the sample, and applied the current parallel to the direction of the magnetic field.

The AMR results are shown in figure 6.12. First of all, and quantitatively, we observe that the Co layer displays a $\sim$1% AMR ratio. Qualitatively we notice the two different shapes of the curves, which can be paired up with perpendicular

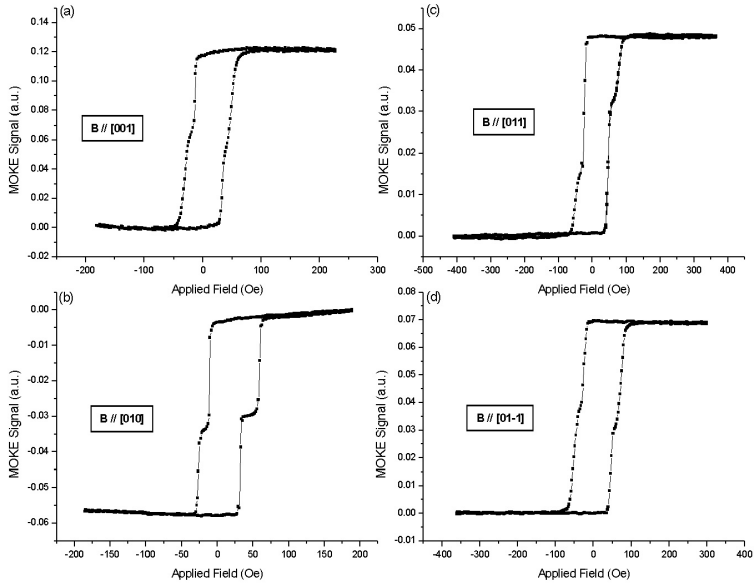

Figure 6.11: MOKE loops for the PSV structure. The field was applied in the plane of the sample, along four directions.

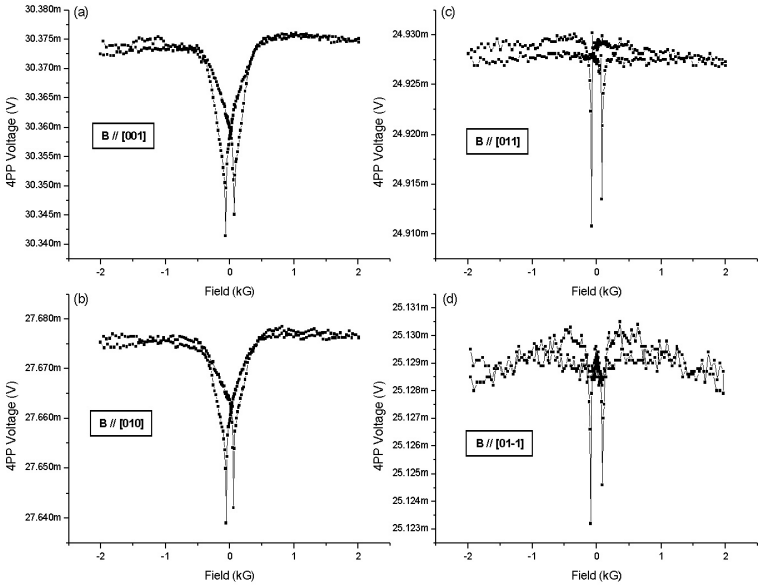

Figure 6.12: AMR results for the PSV Structure. The field was applied in the plane of the sample, and the current was parallel to the direction of the field.

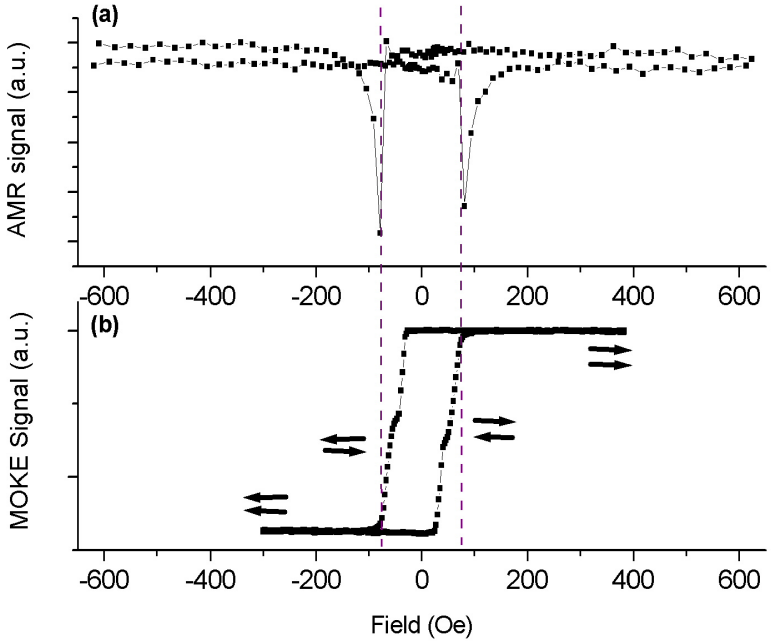

Figure 6.13: Bringing together figures 6.11 and 6.12, we observe the correspondence of the switching field of the Co top electrode observed in the (a) AMR curve; and (b) MOKE loop.

applied field directions: H||[001],[010] and H||[011],[01$\bar{1}$]. The sharp spike observed in figures 6.12(c) and (d) is characteristic of an easy axis switch. Indeed, the magnetisation of the layer is jumping, rather than rotating, to the antiparallel orientation extremely rapidly at the saturation field strength. However the v-shape curve in figures 6.12(a) and (b) indicates that the magnetisation in the sample is rotating in plane in order to reach the antiparallel alignment, which is indicative of a hard axis of magnetisation for the layer. These AMR results allow us to complement the MOKE data, thus verifying the expected four-fold anisotropy of the Co film grown on MgO [159].

As we have mentioned above, the AMR data was taken using a contact probe set-up. The fact that the AMR data only shows single peaks indicates that we are only running the current through the (Au cap and) Co layer, as the resistivity is not affected by the Fe layer's switching. This further confirms that we have an insulating tunnel barrier and we are able to selectively probe only this top electrode. This is further displayed in figure 6.13, where we see the position of the

Layer	t (nm)	ρ (nm)	Magn. Moment (μ_B)	N (10^{28} m^{-3})
Fe	4.1 ± 0.3	0.2 ± 0.1	1.91 ± 0.06	8.49†
MgO	3.6 ± 0.3	0.5 ± 0.1	0†	9.10 ± 0.16
Co	8.3 ± 0.4	0.6 ± 0.1	1.43 ± 0.02	8.99†

Table 6.6: Summary of PNR fit results for the MgO-based PSV, showing the best fit parameters for the thickness, t, roughness, ρ, magnetic moment, μ_B, and atomic density, N, for the relevant layers. A † indicates that the parameter was not fitted (kept to 0 or to the bulk value).

AMR peaks correspond to the steps in the MOKE loops, within field calibration error on the two set-ups.

In order to further characterise the magnetic properties of the individual FM layers, we performed PNR on this multilayer sample. Again, fitting the PNR data can provide us with layer-specific magnetic and structural information. The data and fits to the data are shown in figure 6.14, and the best fit parameters are summarised in table 6.6.

As it was the case for the barrier samples (section 6.3), we notice two features in the fit parameters, which are again a decrease in the FM layers' magnetic moment, and a slight decrease in the atomic density of the MgO tunnel barrier. This time, however, the decrease in the atomic density is not caused by non-stoichiometric growth (evaporation directly from an MgO crystal) but only by slightly imperfect epitaxial growth. We note that the deviation from the bulk value is less than that of the case of Mg evaporation in an O_2 background atmosphere.

In the case of the magnetic moments of the Fe and Co layer, the deviation from the theoretical bulk values is larger than that for the barrier samples above. We again attribute this to interdiffusion at the interfaces in the sample, and the formation of interfacial FeO and CoO inter-layers. In particular the Fe layer is grown on and covered by MgO, which potentially doubles the amount of interfacial oxidation.

PSV Conclusion and Further Work

In conclusion for this section, we have grown a high-quality pseudo-spin valve structure by UHV MBE. The structure was fully crystalline, with smooth inter-

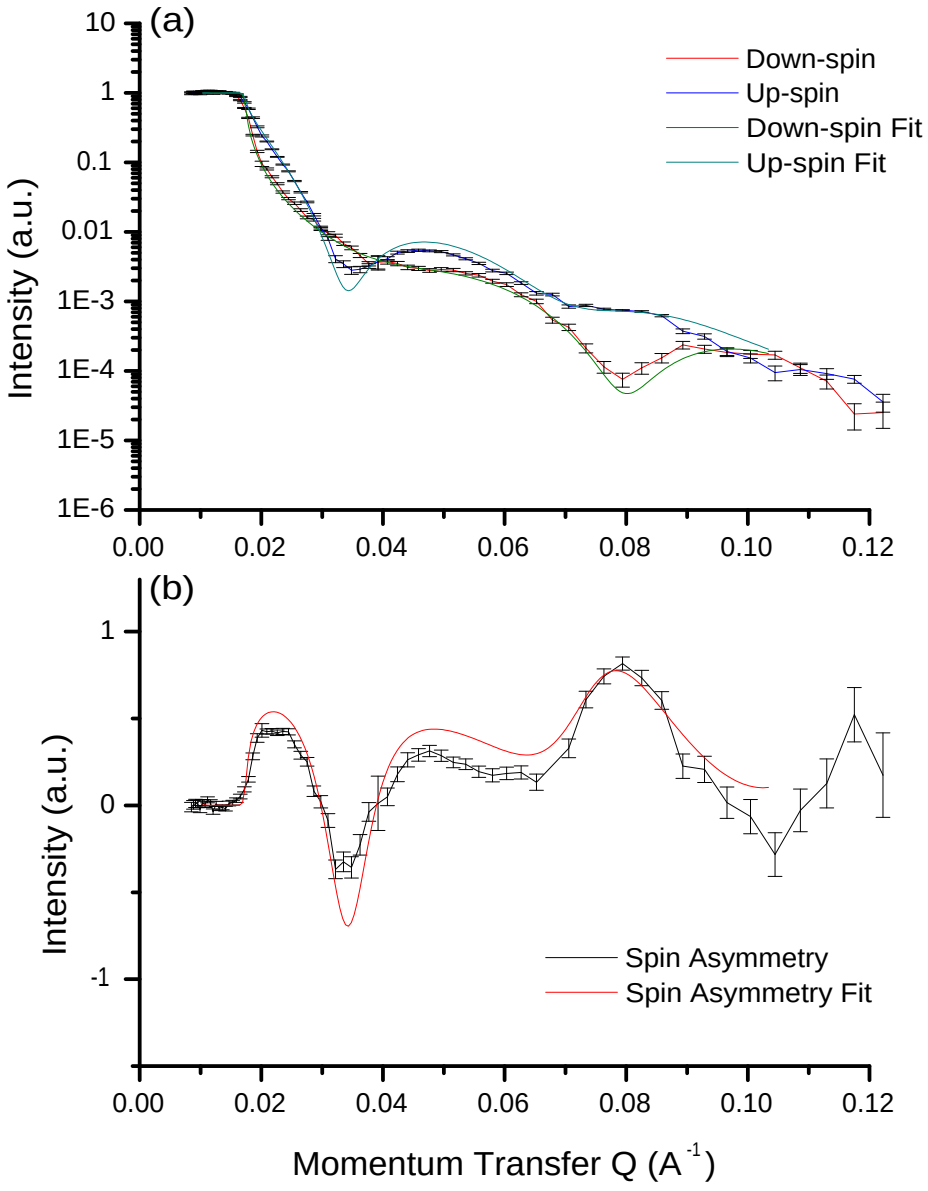

Figure 6.14: Normalised PNR intensity measurement and fits to (a) spin-up and spin-down reflectivities; and (b) spin-asymmetry data for the MgO-based PSV sample.

faces throughout. We have demonstrated epitaxy-induced magneto-crystalline anisotropy and *in consequence* controlled independent switching of two ferromagnetic layers in a MTJ structure. Future work on such devices will include transport characterisation measurements, with the current perpendicular to the plane, in order to measure the TMR ratio through the epitaxial MgO barrier.

6.5 MgO as a Buffer Layer in a Monolithic-Integrated Device

Thin MgO layers have another useful application as a buffer layer. We studied and used this property of MgO in the context of a collaboration project with the Universities of Glasgow and Salford, titled Monolithic-Integrated Optical Devices containing Magneto-Optic Elements.

6.5.1 Overview of the Monolithic-Integrated Devices Project

Laser sources can suffer instabilities when placed within an optical system due to the injection noise caused by light being reflected back into the laser cavity [160]. Currently, in order to avoid this instability, bulk optical isolators are incorporated between laser sources and connected optical elements. The assembly of individual components in a bulk isolator is a complex process that significantly increases cost and reduces yield. Consequently, the prospect of a monolithically integrated optical-isolator has attracted considerable interest. The underlying difficulty to achieve this is that the magneto-optic response of conventional III-V semiconductors such as GaAs is extremely small, requiring the application of an impractically large magnetic field in order to elicit a significant response. Some of the issues and potential solutions were reviewed by Hutchings [161]. The approach that this collaboration project was to take was based on extending the Faraday rotation technique used in bulk magneto-optic devices. The key feature of such an isolator is the non-reciprocal nature of the Faraday effect, which imparts the same rotation sense to the polarisation in both directions of propagation. Therefore a MO crystal placed in between two linear polarisers at 45° to each other will constitute an isolator, if the MO crystal imparts a 45° rotation to the polarisation of the light. The rotation of light in the forward

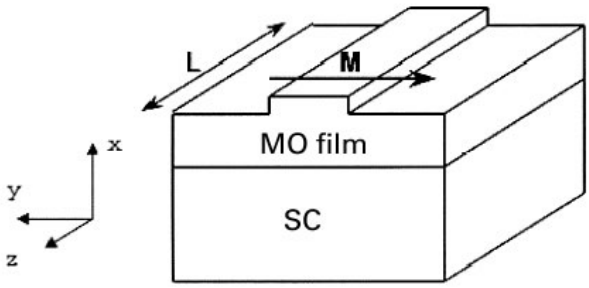

Figure 6.15: (from [162]) Isolator structure for the rib waveguide. A nonreciprocal phase shift is generated in waveguide MO films by the application of a transverse magnetic field to the waveguide axis. Light propagation is along the z direction.

direction is parallel to and is passed by the output polariser, but in the backward direction it is orthogonal to the first polariser and is subsequently blocked [162].

There are two possible implementations to achieve non-reciprocal behaviour in integrated planar devices. The first uses the magneto-optic Kerr effect with a transverse magnetic (TM)-guided mode and an applied transverse magnetic field and at the core-cladding interface. We considered implementing this with a ferromagnetic metallic layer but initial simulations indicated that the optical losses would be prohibitive. The second approach uses Faraday rotation, which allows the use of transverse electric (TE)-gain in conventional semiconductor wafer structures and is the approach which was undertaken in this collaboration project.

The transfer of the non-reciprocal Faraday rotation principles to a planar, SC wave-guide geometry raises a number of inherent difficulties. Firstly, the guided-wave structure introduces a birefringence which limits the coherence of the polarisation conversion due to Faraday rotation. Secondly, although polarisation selectivity can be routinely incorporated for TE- or TM-modes, it is not straightforward for other polarisation angles. However, the integrated device devised in collaboration with Glasgow and Salford implemented this, and was based on incorporating an effective wave-plate with an asymmetric waveguide to provide a reciprocal polarisation rotation [161, 163]. The basic design of the waveguide isolator structure is shown in figure 6.15.

6.5.2 Magneto-Optic Layer Deposition

The magneto-optic material that we used was an yttrium-iron oxide garnet, often referred to as YIG, with chemical composition $Y_3Fe_5O_{12}$. This alloy is known to have a very high Faraday rotation, even for thin films, and a low optical absorption for the near-infrared wavelengths. The Verdet constant is additionally enhanced for the communication wavelengths with Cerium substitution: $Ce_1Y_2Fe_5O_{12}$ (Ce:YIG). Experimentally, there are several approaches to the deposition of YIG. It has been grown by PLD [164, 165], RF-sputtering [166–169], metal-oxide chemical vapour deposition [170], and MBE co-evaporation of Y and Fe in an oxygen background has also been suggested. Each of these comes with its own difficulties in terms of getting the film quality and layer stoichiometry correct.

At first we considered MBE co-evaporation, but were faced with several difficulties, including the challenge of correctly dosing the two evaporators and the O_2 background pressure for stoichiometry, and keeping the evaporation rates stable for extended periods of time (up to several hours for thick layers). It therefore proved much more straightforward to sputter our magneto-optic layers directly from a $Ce_1Y_2Fe_5O_{12}$ target. This should yield the correct composition for the film and, with accurate control of deposition rate and conditions, a smooth film and interface. We did not expect the crystallinity of the Ce:YIG deposited by RF-sputtering to be perfect upon deposition, as we were sputtering at room temperature in the first instance. However, previous research [166, 168] and a study carried out at Glasgow on our samples indicated that improvements in crystallinity, and subsequent enhancement of the Verdet coefficient, can be obtained through post-annealing of the films.

6.5.3 MgO as a Buffer Layer

We note that the annealing temperature range for the Ce:YIG films was 750-950°C, which is one of the reasons for requiring an inert buffer layer. Indeed at such temperatures we expect large amounts of undesirable As interdiffusion from the substrate into the MO layer [133]. In the case of high-temperature growth, Langmuir evaporation of As at these temperatures would result in considerable roughening of the GaAs surface, and As migration leads to intermixing in the SC

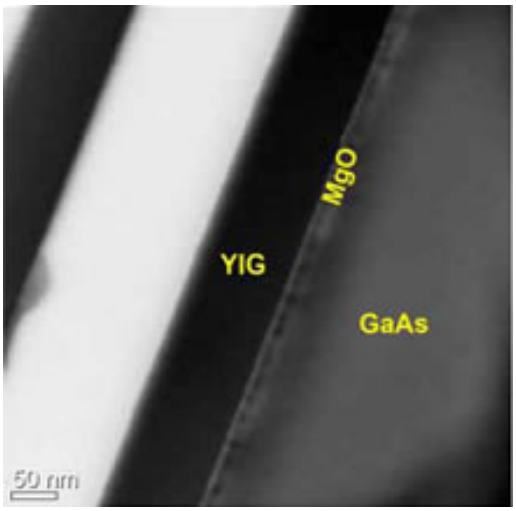

Figure 6.16: Sample *SPUT‡07.10.2005*, nominally 100 nm Ce:YIG/8 nm MgO/GaAs(100). TEM image of a sputtered Ce:YIG/MgO/GaAs wave-guide sample. TEM image courtesy of Dr. Ian MacLaren, University of Glasgow.

waveguide, and is detrimental to the quantum wells. However, high-quality MgO layers as thin as 4.5 nm grown on GaAs have been demonstrated to adequately protect the GaAs and preserve the integrity of the quantum well at temperatures in excess of 800°C [167]. Furthermore, in the case of growth in an O_2 background, the oxygen-rich ambient atmosphere and high growth temperature would lead to rapid oxidation of the GaAs substrate surface [131].

The second reason for the MgO buffer layer is that it offers an appropriate lattice matching between the SC surface and the Ce:YIG. With $a_{YIG} = 12.376$ Å, and $a_{GaAs} = 5.654$ Å there is a very large lattice mismatch between the SC and the MO layer. However, the insertion of an intermediate MgO layer provided an appropriate seed for crystallinity of the MO film [170]. And as we have seen above, GaAs and MgO are also epitaxially linked. Therefore a potentially high-quality MgO buffer layer may provide a route to approaching the crystalline Verdet constant values for the Ce:YIG.

The crystallinity of our UHV MBE-grown MgO layers was discussed in sections 6.1.2 and 6.1.3, but not that of the samples grown by sputter deposition. We unfortunately do not have XRD data for these layers. Figure 6.16 shows a TEM image of a sample we grew entirely in our sputtering chamber without removal from the vacuum. Due to a problem with the sample holder heat source

at the time of deposition, this sample was grown at only 150°C. The TEM image was taken directly after deposition, before any annealing treatment. Therefore the Ce:YIG layer is amorphous, as expected. The MgO buffer layer however already displayed indications of crystalline growth. In addition to this the TEM showed very sharp interfaces for this sample.

6.6 MgO: Conclusions and Further Work

We have shown and explored from a fundamental point of view how magnesium oxide layers can be useful for device applications. As previously stated, there is currently huge interest and research towards incorporating MgO layers into electronic and spintronic devices. However it is clearly emerging that high-quality MgO layers are necessary for practical applications.

Therefore it is crucial to understand and control as best we can the interface dynamics in MgO-based samples. These include epitaxy, growth mode, and of course interdiffusion effects. As we have shown, such effects and parameters are paramount to the role of the MgO, as well as affecting neighbouring layers such as ferromagnetic contacts. Finally, as we have seen in our work on the wave-guide project, high-quality MgO can lead the way to incorporating further exotic materials to semiconductor-based devices.

Further work on the growth and use of MgO will focus on optimising the growth to obtain fully epitaxial layers and barriers on a variety of substrates. This might be done by redesigning the MgO source evaporator geometry in order to better heat and degas the source crystal, or in the case of the growth in oxygen background modifying the Mg evaporator to gain better control of the deposition rate. We have seen that growth by sputtering already produces high-quality MgO films, which provides an opportunity to use more complex materials and explore coverage and thickness effects. This enables us to fairly easily design and produce various samples in order to guide further studies of fully epitaxial samples grown in the MBE chamber. Such samples will be of great interest for spintronics research, both in terms of magneto-resistance and spin injection and detection into a semiconductor-based device.

Acknowledgements

Thanks again to M. E. Vickers of the Department of Materials Science and Metallurgy for assistance during the X-ray measurements. Thanks to R. M. Dalgliesh and S. Langridge of the Rutherford Appleton Laboratory, A. Ionescu, N.-J. Steinke and S. Easton for the PNR data collection. Thanks to T.J. Hayward for some MOKE data, and J. Llandro for the AMR measurements. Thanks to W.-S. Lew for the sputter-growths. We also thank D. C. Hutchings and B. Holmes from the University of Glasgow, A. Boardman from the University of Salford, for a fruitful collaboration with the optical isolator project.

Chapter 7

Summary and Outlook

Experimental Progress

During the course of this work, we have developed and improved several pieces of apparatus and experimental techniques. The UHV chamber itself is in constant need of repairs and maintenance, and whenever possible we took these opportunities to improve and update the system. In addition to this, we experimented and developed the growth of MgO by MBE, both from an MgO source, and from Mg in an O_2 background. We were able to include MgO layers in thin epitaxial multilayer structures.

The EL set-up was nearly entirely redesigned during the course of this Ph.D. We switched to the oblique Hanle geometry, introduced low-temperature capability, and improved the optical polarisation detection.

Fe/GaAs and Fe/InAs

After magnetic and structural characterisation of ultrathin epitaxial Fe films grown on GaAs and InAs, we have established that interface and interdiffusion effects are the dominant mechanisms which influence the value of the magnetic moment in these films. Substrate surface roughness increases intermixing of the atomic species present, and we suggest the formation of non-ferromagnetic compounds at the interface contributes to the decrease of the magnetic moment.

Spintronics and Electro-Luminescence

We have used the EL experiment to probe spin-states of carriers in semiconductor structures. We have characterised our spin-LED structures electrically and presented their magnetic behaviour. We have detected a small optical polarisation of the light emitted by our spin-LEDs, which indicates a ∼1% spin injection polarisation at RT. This value increases to ∼4% at 77 K. We note that the polarisation detected from an *in situ* and *ex situ* transferred sample are near-identical.

MgO Growth and Applications

We have grown and characterised thin MgO buffer and tunnelling layers. Such layers currently generate huge interest in device applications, where MgO is being integrated in magnetic multilayers. We have not obtained completely epitaxial MgO on GaAs, though we have seen some indications of emerging crystallinity. We have studied the influence of an MgO tunnelling barrier on thin FM films, and report a slight decrease in the magnetic moment of such films, which we attribute to interface roughness and subsequent oxidation of the FM layers. We also presented the growth and characterisation of an MgO-based PSV structure, and demonstrated epitaxy-induced magneto-crystalline anisotropy, and in consequence independent switching of the two FM electrodes. We also report on a decrease of the ferromagnetic contacts' magnetic moments in this structure, due to interfacial oxide layers. Finally, we have developed the integration of MgO as a buffer layer in a monolithic device.

Conclusions

From these experiments, we deduce that the interface quality is a critical parameter in thin film magnetic multilayers. Disorder, defects and intermixing at interfaces have drastic consequences on magnetic and structural properties. Epitaxy requires atomically ordered surfaces, and will be destroyed by defects on the substrate or layer surface. Intermixing of the atomic species present during growth is unavoidable to a certain extent. Indeed, high-energy (hot) atoms inci-

dent on a surface will potentially dislocate substrate atoms in the formation of its own bonds. Molecular beam epitaxy and *in situ* surface treatment in UHV aim to provide us with such clean templates for epitaxial growth, which has allowed us to demonstrate epitaxy-induced magneto-crystalline anisotropy in a ferromagnetic film.

As we have seen, roughness amplitude of an interface, which increases the surface area in contact at the interface, contributes to the intermixing. The effects of roughness and intermixing are naturally most important at low coverages, where the proportion of intermixed film is large. We have seen in the Fe/SC magnetic moment study that the films regain their bulk-like magnetic moment as the film thickness increases. In the case of the FM/MgO layers, the PNR results again indicated a slight decrease in the magnetic moment of the Fe and Co layers despite relatively thick layers. This was attributed to increased intermixing and subsequent *e.g.* FeO interlayers due to the greater roughness amplitude in this system as compared to the Fe/SC one.

In addition to affecting magnetic and structural properties, defects and disorder at a surface can change the electrical transport properties at an interface. We have seen this to be the case in spin-LEDs, where certain devices containing defects or pinholes displayed short- or open-circuit behaviour instead of the expected diode-like characteristics from the Schottky contact. Furthermore, impurities at the interface are hugely detrimental to spin injection efficiencies as predicted in ideal FM/SC junctions. It has also been shown in MgO-based device simulations that any interface impurities or defects will destroy the potential spin-filtering effects.

Future Work

Any insight into fundamental properties of physical systems will always raise further questions and open new avenues of research. Following on from this project, we can imagine new experiments exploring these fundamental properties but also device integration and applications.

Although the task of realising a perfect single atomic layer interface seems impossible, we could attempt to optimise growth systems to obtain the highest quality real samples. These could include varying growth conditions such as tem-

perature, but also for instance inserting inert buffer layers in multilayer systems. A thin Au layer between Fe and GaAs may reduce intermixing without being detrimental to the epitaxy of the Fe film. As MgO becomes more commonly used, it would be useful to gain further insight on the evolution of the structural and magnetic properties of ferromagnetic contacts grown on MgO, for instance with a systematic thickness-dependence study. And as we have seen, crystalline MgO could be used as a buffer and protective layer for more complex compounds such as iron garnets.

The integration of epitaxial films in commercial devices such as computer memory elements and hard drive read heads could potentially have a huge impact on their efficiency. However, the challenge of realising an epitaxial multilayer is incompatible with the low-cost and mass production requirements of the industries. Therefore, it seems essential to fully characterise real interfaces, including interdiffusion and intermixing effects, and defects in magnetic multilayer systems. Ultimately, detailed studies such as those carried out in the course of this project will be critical in understanding how the interface properties in ferromagnetic multilayer structures can be engineered to be efficiently integrated in commercially available devices.

Bibliography

[1] S. Blundell, *Magnetism in Condensed Matter* (Oxford University Press, 2001).

[2] S. Chikazumi, *Physics of Ferromagnetism* (Claredon Press, Oxford, 1997).

[3] S. A. Wolf, D. D. Awschalom, R. A. Buhrman, J. M. Daughton, S. von Molnár, M. L. Roukes, A. Y. Chtchelkanova, and D. M. Treger, Science **294**, 1488 (2001).

[4] D. D. Awschalom and M. E. F. N. Samarth, Sci. Am. **286**, 66 (2001).

[5] S. Datta and B. Das, Appl. Phys Lett. **56**, 665 (1990).

[6] J. Nitta, NTT Tech. Rev. **2**, 31 (2004).

[7] R. Williams, *Modern GaAs Processing Methods* (Artech House, Boston, 1990).

[8] C. Y. Chang and F. Kai, *GaAs High-Speed Devices* (John Wiley & Sons, New York, 1994).

[9] *http://kottan-labs.bgsu.edu/teaching/workshop2001/chapter5.htm.*

[10] D. E. Aspnes, J. B. Theeten, and R. P. H. Chang, J. Vac. Sci. Technol. **16**, 1374 (1979).

[11] R. P. H. Chang and J. J. Coleman, Appl. Phys. Lett. **32**, 332 (1978).

[12] M.R. Brozel and G.E. Stillman, *editors*, *Properties of Gallium Arsenide (3rd Edition)* (Institution of Engineering and Technology, 1996).

[13] M. Hickey, *Spin Injection from Magnetic Thin Films into InGaAs Quantum Wells* (PhD Thesis, University of Cambridge, 2005).

[14] R. J. Pechman, X.-S. Wang, and J. H. Weaver, Phys. Rev. B **51**, 10929 (1995).

[15] D. M. Gillingham, *Spin Transport on the Nanoscale* (PhD Thesis, University of Cambridge, 2003).

[16] X.-S. Wang, R. J. Pechman, and J. H. Weaver, Appl. Phys. Lett. **65**, 2818 (1994).

[17] B. Goldstein, D. J. Szostak, and V. S. Ban, Surf. Sci. **57**, 733 (1976).

[18] R. Arès, *Growth Mechanisms of Atomic Layer Epitaxy Studied* In situ *by Reflectance Difference Spectroscopy* (PhD Thesis, Simon Fraser University, Canada, 1997).

[19] D. K. Biegelsen, R. D. Bringans, J. E. Northrup, and L.-E. Swartz, Phys. Rev. B **41**, 5701 (1990).

[20] J. Behrend, M. Wassermeir, L. Däweritz, and K. H. Ploog, Surf. Sci. **342**, 63 (1995).

[21] G. P. Srivastava and S. J. Jenkins, Phys. Rev. B **53**, 12589 (1996).

[22] Q.-K. Xue, T. Hashizume, and T. Sakurai, Appl. Surf. Sci. **141**, 244 (1999).

[23] G. Binnig and H. Rohrer, Helv. Phys. Acta **55**, 726 (1982).

[24] P. K. Larsen, J. H. Neave, J. F. van der Veen, P. J. Dobson, and B. A. Joyce, Phys. Rev. B **27**, 4966 (1983).

[25] M. Sauvage-Simkin, R. Pinchaux, J. Massies, P. Calverie, N. Jedrecy, J. Bonnet, and I. K. Robinson, Phys. Rev. Lett. **62**, 563 (1989).

[26] J. R. Waldrop and R. W. Grant, Appl. Phys. Lett. **34**, 630 (1979).

[27] G. Wastlbauer and J. A. C. Bland, Adv. Phys. **54**, 137 (2005).

[28] H. Takeshita, H. Akinaga, M. Ehrigher, Y. Suzuki, K. Ando, and K. Tanaka, Jpn. J. Appl. Phys. **34**, 1119 (1995).

[29] E. M. Kneedler, B. T. Jonker, P. M. Thibado, R. J. Wagner, B. V. Shanabrook, and L. J. Whitman, Phys. Rev. B **56**, 8163 (1997).

[30] R. Moosbühler, F. Bensch, M. Dumm, and G. Bayreuther, J. Appl. Phys. **91**, 8757 (2002).

[31] A. Ionescu, M. Tselepi, D. M. Gillingham, G. Wastlbauer, H. E. Beere, D. A. Ritchie, and J. A. C. Bland, Phys. Rev. B **72**, 125404 (2005).

[32] S. C. Hong, M. S. Chung, B.-G. Yoon, and J. I. Lee, J. Magn. Magn. Mater. **239**, 39 (2002).

[33] S. C. Erwin, S.-H. Lee, and M. Scheffler, Phys. Rev. B **65**, 205422 (2002).

[34] B. Heinrich and J. A. C. Bland, *editors*, *Ultrathin Magnetic Structures* (Springer-Verlag, Berlin, 1994).

[35] K. Ha and R. C. O'Handley, J. Appl. Phys. **85**, 5282 (1999).

[36] Y. B. Xu, E. T. M. Kernohan, D. J. Freeland, A. Ercole, M. Tselepi, and J. A. C. Bland, Phys. Rev. B **58**, 890 (1998).

[37] M. Zölfland, M. Brockmann, M. Köhler, S. Kreuzer, T. Schweinböck, S. Miethaner, F. Bensch, and G. Bayreuther, J. Magn. Magn. Mater. **175**, 16 (1997).

[38] O. Thomas, Q. Shen, P. Schieffer, N. Tournerie, and B. Lépine, Phys. Rev. Lett. **90**, 017205 (2003).

[39] Y. Zhai, L. Shi, W. Zhang, Y. X. Xu, H. Zhai, W. X. Tang, X. F. Jin, Y. B. Xu, and J. A. C. Bland, J. Appl. Phys. **93**, 7622 (2003).

[40] S. J. Steinmuller, M. Tselepi, V. Strom, and J. A. C. Bland, J. Appl. Phys. **91**, 8679 (2002).

[41] S. J. Steinmuller, M. Tselepi, G. Wastlbauer, V. Strom, D. M. Gillingham, A. Ionescu, and J. A. C. Bland, Phys. Rev. B **70**, 024420 (2004).

[42] M. A. Ruderman and C. Kittel, Phys. Rev. **96**, 99 (1954).

[43] T. Kasuya, Prog. Theor. Phys. **16**, 45 (1956).

[44] K. Yosida, Phys. Rev. **106**, 893 (1957).

[45] *http://www.wikipedia.org/.*

[46] M. N. Baibich, J. M. Broto, A. Fert, F. N. V. Dau, F. Petroff, P. Eitenne, G. Creuzet, A. Friederich, and J. Chazelas, Phys. Rev. Lett. **61**, 2472 (1988).

[47] A. Samad, *Structural and Magnetic Properties of Spin Valve Structures* (PhD Thesis, University of Cambridge, 1999).

[48] J. Shen and J. Kirschner, Surf. Sci. **500**, 300 (2002).

[49] A. Ercole, *Thin Film Magnetism at Surfaces and Interfaces* (PhD Thesis, University of Cambridge, 1998).

[50] W. S. Lew, A. Samad, S. P. Li, L. Lopez-Diaz, G. X. Cheng, and J. A. C. Bland, J. Appl. Phys. **87**, 5947 (2000).

[51] A. Ercole, T. F. M. Patel, C. Daboo, R. J. Hicken, and J. A. C. Bland, J. Magn. Magn. Mater. **156**, 121 (1996).

[52] J. A. C. Bland, C. Daboo, M. Patel, T. Fujimoto, and J. Penfold, Phys. Rev. B **57**, 10272 (1998).

[53] M. Patel, T. Fujimoto, A. Ercole, C. Daboo, and J. A. C. Bland, J. Magn. Magn. Mater **156**, 53 (1996).

[54] W. Y. Lee, A. Samad, T. A. Moore, J. A. C. Bland, and B. C. Choi, J. Appl. Phys. **87**, 6600 (2000).

[55] W. Y. Lee, A. Samad, T. A. Moore, J. A. C. Bland, and B. C. Choi, Phys. Rev. B **61**, 6811 (2000).

[56] W. S. Lew, S. P. Li, L. Lopez-Diaz, D. C. Hatton, and J. A. C. Bland, Phys. Rev. Lett. **90**, 217201 (2003).

[57] L. Thomas, M. G. Samant, and S. S. P. Parkin, Phys. Rev. Lett. **84**, 1816 (2000).

[58] Dorothy M. Hoffman, Bawa Singh and John H. Thomas III, *Handbook of Vacuum Science and Technology* (Academic Press, 1998).

[59] J.M. Blakely, *Introduction to the Properties of Crystal Surfaces* (Pergamon Press, Oxford, 1973).

[60] Zhong Lin Wang, *Reflection Electron Microscopy and Spectroscopy for Surface Analysis* (Cambridge University Press, 1996).

[61] A. W. Adamson and A. P. Gast, *Physical Chemistry of Surfaces* (John Wiley & Sons, New York, 1997).

[62] S. D. Bader and E. R. Moog, J. Appl. Phys. **61**, 3729 (1987).

[63] S. D. Bader, J. Magn. Magn. Mater. **100**, 440 (1991).

[64] J. Zak, E. R. Moog, and C. L. S. D. Bader, Phys. Rev. B **43**, 6423 (1991).

[65] C. M. Gürtler, *Spin Transport and Mesomagnetismin Fe Nanostructures* (PhD Thesis, University of Cambridge, 2001).

[66] D. A. Allwood, G. Xiong, M. D. Cooke, and R. P. Cowburn, J. Phys. D: Appl. Phys. **36**, 2175 (2003).

[67] W. G. Williams, *Polarized Neutrons* (Claredon Press, Oxford, 1988).

[68] B. A. Hands, editor, *Cryogenic Engineering* (Academic Press, 1986).

[69] H. Zabel, Appl. Phys. A **58**, 159 (1994).

[70] A. Filipe, A. Schuhl, and P. Galtier, Appl. Phys. Lett. **70**, 129 (1997).

[71] F. Bensch, G. Garreau, R. Moosbhler, G. Bayreuther, and E. Beaurepaire, J. Appl. Phys. **89**, 7133 (2001).

[72] R. Meckenstock, D. Spoddig, K. Himmelbauer, H. Krenn, M. Doi, W. Keune, Z. Frait, and J. Pelzl, J. Magn. Magn. Mater. **240**, 410 (2002).

[73] J. S. Claydon, Y. B. Xu, M. Tselepi, J. A. C. Bland, and G. van der Laan, J. Appl. Phys. **95**, 6543 (2004).

[74] L. Giovanelli, G. Panaccione, G. Rossi, M. Fabrizioli, C.-S. Tian, P. L. Gastelois, J. Fujii, and C. H. Back, Phys. Rev. B **72**, 045221 (2005).

[75] M. Tselepi, Y. B. Xu, D. J. Freeland, T. A. Moore, and J. A. C. Bland, J. Magn. Magn. Mater. **226**, 1585 (2001).

[76] C. M. Teodorescu, F. Chevrier, R. Brochier, C. Richter, V. Ilakovac, O. Heckmann, P. D. Padova, and K. Hricovini, Eur. Phys. J. B **28**, 305 (202).

[77] J.-B. Laloë, F. van Belle, A. Ionescu, C. A. F. Vaz, M. Tselepi, G. Wastlbauer, R. M. Dalgliesh, S. Langridge, and J. A. C. Bland, IEEE Trans. Magn. **42**, 2933 (2006).

[78] A. Ionescu, *Magnetic and Structural Studies on Epitaxial Heterostructures* (PhD Thesis, University of Cambridge, 2006).

[79] Y. B. Xu, E. T. M. Kernohan, M. Tselepi, J. A. C. Bland, and S. N. Holmes, Appl. Phys. Lett. **73**, 399 (1998).

[80] J. S. Arlow, D. F. Mitchell, and M. J. Graham, J. Vac. Sci. Technol. A **5(4)**, 572 (1987).

[81] A. Ionescu, C. A. F. Vaz, J.-B. Laloë, F. van Belle, A. S. Middleton, M. Tselepi, G. Wastlbauer, R. M. Dalgliesh, S. Langridge, and J. A. C. Bland, *in preparation* (2007).

[82] Y. B. Xu, D. J. Freedland, M. Tselepi, and J. A. C. Bland, J. Appl. Phys. **87**, 6110 (2000).

[83] L. Ruppel, G. Witte, C. Wöll, T. Last, S. F. Fischer, and U. Kunze, Phys. Rev. B **66**, 245307 (2002).

[84] Y. B. Xu, M. Tselepi, C. M. Guertler, C. A. F. Vaz, G. Wastlbauer, J. A. C. Bland, E. Dudzik, and G. van der Laan, J. Appl. Phys **89**, 7156 (2001).

[85] J. S. Claydon, Y. B. Xu, M. Tselepi, J. A. C. Bland, and G. van der Laan, Phys. Rev. Lett. **93**, 037206 (2004).

[86] C. M. Teodorescu, F. Chevrier, R. Brochier, C. Richter, O. Heckmann, V. Ilakovac, P. D. Padova, and K. Hricovini, Surf. Sci. **482**, 1004 (2001).

[87] K. Yoh, H. Ohno, K. Sueoka, and M. E. Ramsteiner, J. Vac. Sci. Tech. B **22**, 1432 (2004).

[88] Y. B. Xu, D. J. Freeland, M. Tselepi, and J. A. C. Bland, Phys. Rev. B **62**, 1167 (2000).

[89] R. A. Gordon, E. D. Crozier, D.-T. Jiang, T. L. Monchesky, and B. Heinrich, Phys. Rev. B **20**, 21512157 (2000).

[90] C. A. F. Vaz, A. Ionescu, T. Trypiniotis, J. A. C. Bland, R. M. Dalgliesh, and S. Langridge, J. Appl. Phys. **97**, 10J119 (2005).

[91] G. Lampel, Phys. Rev. Lett. **20**, 491 (1968).

[92] D. T. Pierce and F. Meier, Phys. Rev. B **13**, 5484 (1976).

[93] B. Heinrich and J.A.C. Bland, *editors*, *Ultrathin Magnetic Structures* (Springer-Verlag, Berlin, 2005).

[94] F. Meier and B.P. Zakharchenya, *editors*, *Optical Orientation* (North-Holland, New York, 1984).

[95] B. T. Jonker, Y. D. Park, B. R. Bennett, H. D. Cheong, G. Kioseoglou, and A. Petrou, Phys. Rev. B **62**, 8180 (2000).

[96] J. Strand, X. Lou, C. Adelmann, B. D. Schultz, A. F. Isakovic, C. J. Palmstrøm, and P. A. Crowell, Phys. Rev. B **72**, 155308 (2005).

[97] G. Schmidt, D. Ferrand, L. W. Molenkamp, A. T. Filip, and B. J. van Wees, Phys. Rev. B **62**, R4790 (2000).

[98] E. I. Rashba, Phys. Rev. B **62**, 16267 (2000).

[99] D. L. Smith and R. N. Silver, Phys. Rev. B **64**, 045323 (2001).

[100] J. D. Albrecht and D. L. Smith, Phys. Rev. B **66**, 113303 (2002).

[101] I. Žutić, J. Fabian, and S. D. Sarma, Rev. Mod. Phys. **76**, 323 (2004).

[102] P. H. Song and K. W. Kim, Phys. Rev. B **66**, 035207 (2002).

[103] R. J. Elliot, Phys. Rev. **96**, 266 (1954).

[104] F. Seitz and D. Turnbull, *editors*, *Solid State Physics, Vol. 14* (Academic, New York, 1963).

[105] M. I. D'yakanov and V. I. Perel', Sov. Phys. Solid State **13**, 3023 (1971).

[106] G. L. Bir, A. G. Aronov, and G. E. Pikus, Zh. Eksp. Teor. Fiz. **69**, 1382 (1975).

[107] S. Vutukuri, M. Chshiev, and W. H. Butler, J. Appl. Phys. **99**, 08K302 (2006).

[108] M. Zwierzychi, K. Xia, P. J. Kelly, G. E. W. Bauer, and I. Turek, Phys. Rev. B **67**, 092401 (2003).

[109] O. Wunnicke, P. Mavropoulos, R. Zeller, P. H. Dederichs, and D. Grundler, Phys. Rev. B **65**, 241306 (2002).

[110] B. Lépine, C. Lallaizon, P. Schieffer, A. Guivarc'h, G. J. A. Rocher, F. Abel, C. Cohen, D. Députier, and F. N. V. Dau, Thin Solid Films **446**, 6 (2004).

[111] T. J. Zega, A. T. Hanbicki, S. C. Erwin, I. Žutić, G. Kioseoglou, C. H. Li, B. T. Jonker, and R. M. Stroud, Phys. Rev. Lett. **96**, 196101 (2006).

[112] B. Schultz, H. H. Farrell, M. M. R. Evans, K. Lüdge, and C. J. Palstrøm, J. Vac. Sci. Technol. B **20**, 1600 (2002).

[113] L. M. Corliss, J. M. Hastings, W. Kunnmann, R. J. B. M. F. Collins, and E. Gurewtiz, Phys. Rev. B **25**, 245 (1982).

[114] V. F. Motsnyi, J. D. Boeck, J. Das, W. van Roy, G. Borghs, E. Goovaerts, and V. I. Safarov, Appl. Phys. Lett. **81**, 265 (2002).

[115] R. Fielderling, M. Keim, G. Reuscher, W. Ossau, G. Schmidt, A. Waag, and L. W. Molenkamp, Nature **402**, 787 (1999).

[116] H. J. Zhu, M. Ramsteiner, H. Kostial, M. Wassermeier, H.-P. Schnherr, and K. H. Ploog, Phys. Rev. Lett. **87**, 016601 (2001).

[117] A. T. Hanbicki, B. T. Jonker, G. Itskos, G. Kioseoglou, and A. Petrou, Appl. Phys. Lett. **80**, 1240 (2002).

[118] V. F. Motsnyi, P. van Dorpe, W. van Roy, E. Goovaerts, V. I. Safarov, G. Borghs, and J. D. Boeck, Phys. Rev. B **68**, 245319 (2003).

[119] X. Jiang, R. Wang, R. M. Shelby, R. M. Macfarlane, S. R. Bank, J. S. Harris, and S. S. P. Parkin, Phys. Rev. Lett. **94**, 056601 (2005).

[120] G. Salis, R. Wang, X. Jiang, R. M. Shelby, S. S. P. Parkin, S. R. Bank, and J. S. Harris, Appl. Phys. Lett. **87**, 262503 (2005).

[121] R. Wang, X. Jiang, R. M. Shelby, S. S. P. Parkin, S. R. Banks, and J. S. Harris, Appl. Phys. Lett. **86**, 052901 (2005).

[122] S. M. Sze, *Physics of Semiconductor Devices* (Wiley and Sons, 1981).

[123] *http://www.ioffe.ru/sva/nsm/semicond/index.html*.

[124] C. Adelmann, X. Lou, J. Strand, C. J. Palmstrøm, and P. A. Crowell, Phys. Rev. B **71**, 121301 (2005).

[125] M. Bowen, V. Cros, F. Petroff, A. Fert, C. M. Boubeta, J. L. Costa-Krämer, J. V. Anguita, A. Cebollada, F. Briones, J. M. de Teresa, et al., Appl. Phys. Lett. **79**, 1655 (2001).

[126] S. S. P. Parkin, C. Kaiser, A. Panchula, P. M. Rice, B. Hughes, M. Samant, and S.-H. Yang, Nat. Mat. **3**, 862 (2004).

[127] S. Yuasa, T. Nagahama, A. Fukushima, Y. Suzuki, and K. Ando, Nat. Mat. **3**, 868 (2004).

[128] *http://www.webelements.com/*.

[129] E. J. Tarsa, M. D. Graef, D. Clarke, A. C. Gossard, and J. S. Speck, J. Appl. Phys. **73**, 3276 (1993).

[130] L. S. Hung, L. R. Zheng, and T. N. Blanton, Appl. Phys. Lett. **60**, 3129 (1992).

[131] L. D. Chang, M. Z. Tseng, E. L. Hu, and D. K. Fork, Appl. Phys. Lett. **60**, 1753 (1992).

[132] C. Martínez-Boubeta, J. L. Menédez, J. L. Costa-Krämer, J. M. García, J. V. Anguita, B. Bescós, A. Cebollada, F. Briones, A. V. Chernykh, I. V. Malikov, et al., Surf. Sci. **482**, 910 (2001).

[133] C. Martínez-Boubeta, E. Navarro, A. Cebollada, F. Briones, F. Peiró, and A. Cornet, J. Cryst. Growth **226**, 223 (2001).

[134] D. K. Fork, K. Nashimoto, and T. H. Geballe, Appl. Phys. Lett. **60**, 1621 (1992).

[135] P. A. Stampe and R. J. Kennedy, Thin Solid Films **326**, 63 (1998).

[136] K. Nashimoto, D. K. Fork, and T. H. Geballe, Appl. Phys. Lett. **60**, 1199 (1992).

[137] W.-Y. Hsu and R. Raj, Appl. Phys. Lett. **60**, 3105 (1992).

[138] S. Yadavalli, M. H. Yang, and C. P. Flynn, Phys. Rev. B **41**, 7961 (1990).

[139] C. T. Foxon, J. A. Harvey, and B. A. Joyce, J. Phys. Chem. Solids **34**, 1693 (1973).

[140] C. Tegenkamp, H. Pfnür, W. Ernst, U. Malaske, J. Wollschläger, D. Peterka, K. M. Schröder, V. Zielasek, and M. Henzler, J. Phys.: Condens. Matter **11**, 9943 (1999).

[141] S. A. Chambers, Surf. Sci. Rep. **39**, 105 (2000).

[142] C. Martínez-Boubeta, A. Cebollada, J. F. Calleja, C. Conteras, F. Peiró, and A. Cornet, J. Appl. Phys. **93**, 2126 (2003).

[143] X.-G. Zhang and W. H. Butler, Phys. Rev. B **70**, 172407 (2004).

[144] A. di Bona, C. Giovanardi, and S. Valeri, Surf. Sci. **498**, 193 (2002).

[145] T. Urano and T. Kanaji, J. Phys. Soc. Jpn. **57**, 3403 (1988).

[146] J. L.Vassent, M. Dynna, A. Marty, B. Gilles, and G. Patrat, J. Appl. Phys. **80**, 5727 (1996).

[147] M. Sicot, S. Andrieu, F. Bertran, and F. Fortuna, Phys. Rev. B **72**, 144414 (2005).

[148] M. Sicot, S. Andrieu, C. Tiusan, F. Montaigne, and F. Bertran, J. Appl. Phys. **99**, 08D301 (2006).

[149] W. H. Butler, X.-G. Zhang, T. C. Schulthess, and J. M. MacLaren, Phys. Rev. B **63**, 054416 (2001).

[150] M. Klaua, D. Ullmann, J. Barthel, W. Wulfhekel, J. Kirschner, R. Urban, T. L. Monchesky, A. E. J. F. Cocran, and B. Heinrich, Phys. Rev. B **64**, 134411 (2001).

[151] H. L. Meyerheim, R. Popescu, J. Kirschner, N. Jedrecy, M. Sauvage-Simkin, B. Heinrich, and R. Pinchaux, Phys. Rev. Lett. **87**, 076102 (2001).

[152] J. Mathon and A. Umerski, Phys. Rev. B **63**, 220403 (2001).

[153] J. Faure-Vincent, C. Tiusan, E. Jouguelet, F. Canet, M. Sajieddine, C. Bellouard, E. Popova, M. hehn, F. Montaigne, and A. Schul, Appl. Phys. Lett. **82**, 4507 (2003).

[154] P. X. Xu, V. M. Karpan, K. Xia, M. Zwierzychi, I. Marushchenko, and P. J. Kelly, Phys. Rev. B **73**, 180402 (2006).

[155] T. Taniyama, G. Wastlbauer, A. Ionescu, M. Tselepi, and J. A. C. Bland, Phys. Rev. B **68**, 134430 (2003).

[156] S. Yuasa, T. Katayama, T. Nagahama, A. Fukushima, H. Kubota, Y. Suzuki, and K. Ando, Appl. Phys. Lett. **87**, 222508 (2005).

[157] J. S. Moodera, L. R. Kinder, T. M. Wong, and R. Meservey, Phys. Rev. Lett. **74**, 3273 (1995).

[158] H. Ebert, A. Vernes, and J. Banhart, Phys. Rev. B **54**, 8479 (1996).

[159] F. Screiber, Z. Frait, T. Zeidler, N. Metoki, W. Donner, H. Zabel, and J. Pelzl, Phys. Rev. B **51**, 2920 (1995).

[160] K. E. Stubkjaer and M. B. Small, IEEE J. Quantum Electron. **20**, 472 (1984).

[161] D. C. Hutchings, J. Phys. D: Appl. Phys. **36**, 2222 (2003).

[162] M. Levy, IEEE J. Sel. Top. Quant. **8**, 1300 (2002).

[163] T. Shintaku, Appl. Phys. Lett. **73**, 1946 (1998).

[164] T. Tepper and C. A. Ross, J. Crsyt. G. **255**, 324 (2003).

[165] H. Kim, A. M. Grishin, K. V. Rao, S. C. Yu, R. Sbiaa, and H. L. Gall, IEEE Trans. Magn. **35**, 3163 (1999).

[166] M.-B. Park and N.-H. Cho, J. Magn. Magn. Mater. **231**, 253 (2001).

[167] B. J. H. Stadler and A. Gopinath, IEEE Trans. Magn. **36**, 3957 (2000).

[168] A. Tate, T. Uno, S. Mino, A. Shibukawa, and T. Shintaku, Jpn. J. Appl. Phys. **35**, 3419 (1996).

[169] T. Shintaku and T. Uno, Jpn. J. Appl. Phys. **35**, 4689 (1996).

[170] B. Stadler, K. Vaccaro, P. Yip, J. Lorenzo, Y.-Q. Li, and M. Cherif, IEEE Trans. Magn. **38**, 1564 (2002).

List of Acronyms

3D three-dimensional

AES Auger electron spectroscopy

AFM atomic force microscope

AMR anisotropic magneto-resistance

BAP Bir-Aronov-Pikus

bcc body-centred cubic

bct body-centred tetragonal

BLS Brillouin light scattering

CCD charge-coupled device

cps counts per second

DP D'yakonov-Perel'

EL electro-luminescence

EY Elliot-Yafet

fcc face centred cubic

FET field effect transistor

FM ferromagnet

GMR giant magneto-resistance

LED light emitting diode

LEED low-energy electron diffraction

LT low temperature

MCD magnetic circular dichroism

MBE molecular beam epitaxy

MO magneto-optical

MOKE magneto-optical Kerr effect

MR magneto-resistance

MRAM magnetic random access memory

MTJ magnetic tunnel junction

PLD pulsed laser deposition

PMMA polymethyl methacrylate acrylic

PNR polarised neutron reflectivity

PSV pseudo-spin-valve

QW quantum well

RF radio frequency

RHEED reflection high-energy electron diffraction

RT room temperature

SC semiconductor

SEM scanning electron microscope

SP superparamagnetic

SQUID superconducting quantum interference device

STM scanning tunnelling microscope

SV spin-valve

TE transverse electric

TEM transmission electron microscopy

TFMM Thin Film Magnetism and Materials

TM transverse magnetic

TMR tunnelling magneto-resistance

UHV ultra-high vacuum

VRW variable retardation waveplate

XRD X-ray diffraction

XRR X-ray reflectivity

YIG yttrium-iron garnet